TECHNISCHE UNIVERSITÄT MÜNCHEN
Lehrstuhl für Statik

Multi-Fidelity Aeroelastic Analysis of Flexible Membrane Wind Turbine Blades

Mehran Saeedi

Vollständiger Abdruck der von der Ingenieurfakultät Bau Geo Umwelt der Technischen Universität München zur Erlangung des akademischen Grades eines

Doktor-Ingenieurs

genehmigten Dissertation.

Vorsitzender:

Prof. Dr.-Ing. habil. Fabian Duddeck

Prüfer der Dissertation:

1. Prof. Dr.-Ing. Kai-Uwe Bletzinger
2. Prof. Dr. Ernst Rank
3. Prof. Dr. Carlo Luigi Bottasso, Politecnico di Milano, Italy

Die Dissertation wurde am 03.08.2017 bei der Technischen Universität München eingereicht und durch die Ingenieurfakultät Bau Geo Umwelt am 11.12.2017 angenommen.

Abstract

This thesis studies a new concept for flexible wind turbine blades. Flexible wings and their advantages have been the topic of various research projects. To realize a flexible wing construction, different concepts have been used including morphing wing, telescopic spars or using smart materials in the construction of the wing. The membrane blade concept, which is studied within the scope of this thesis, is originally an example of a passively controlled structure, whereas one could think of actuation in future realizations.

With the increase in a wind turbine's rotor diameter, aeroelastic simulation of rotor blades to study their unsteady response to disturbances or control actions has become more and more important. To realize the so-called "smart rotors", both active and passive aeroelastic devices have been employed for load mitigation of wind turbines. Within this contribution, a simulation environment for multi-fidelity aeroelastic analysis of wind turbine blades is presented. The goal of the multi-fidelity analysis is realized by using three different approaches for calculating the aerodynamic loading on a wind turbine, which include: blade element momentum (BEM) method, vortex panel method and computational fluid dynamics.

The developed multi-fidelity analysis workflow is used for analysis of a sample membrane blade based on the NASA-Ames phase VI wind turbine. At each level of modeling, the comparison between the performance of the membrane blade and the rigid baseline blade is made. Furthermore, a new combined methodology based on panel-BEM coupling for using the blade element momentum method for the analysis of membrane blades with form varying cross-section is proposed and tested for the studied sample membrane blade. The studied membrane blade demonstrates advantages over the baseline rigid blade in terms of power generation which should be mainly attributed to the increase of profile's camber due to membrane's deflection.

Acknowledgment

This dissertation is the outcome of my work as a PhD candidate in the Chair of Structural Analysis (Lehrstuhl für Statik), Technische Universität München, from June 2012 to June 2017.

First of all, I would like to thank my *Doktorvater*, Prof. Dr.-Ing. Kai-Uwe Bletzinger, for giving me the chance of being a part of his group and enjoying the academic freedom in Lehrstuhl für Statik. This helped me grow as a researcher and I do value it. I also like go express my gratitude to him for his trust and support during my time at the chair.

Furthermore, I would like to thank the members of my examining jury, Prof. Dr. Carlo Luigi Bottasso and Prof. Dr. rer. nat. Ernst Rank. Their interest in my work is gratefully appreciated. I also want to thank Prof. Dr.-Ing. habil. Fabian Duddeck for chairing the jury.

Special thanks goes to, Dr.-Ing. habil. Roland Wüchner. As a student, I have learned a lot from him. I appreciate his patience and I am grateful to him for his trust and for the countless fruitful discussions (both related and non-related to work) we had. I would also like to thank my colleagues at the chair.

Last but not least, I am grateful to my parents for their invaluable love and support and to my wife. Thank you for being the great person you are.

Mehran Saeedi
June 2017

Contents

1 *Introduction*

This thesis has been built upon the idea of multi-fidelity aeroelastic analysis of wind turbines. For realizing this idea, three approaches for predicting aerodynamic loads on a wind turbine have been utilized. They are:

- Blade element momentum method (BEM)
- Vortex panel method
- Computational fluid dynamics

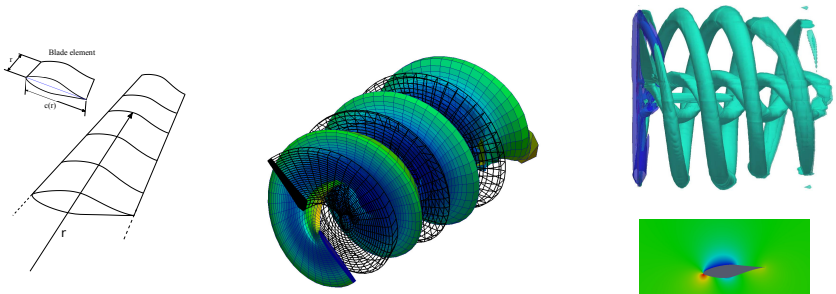

Figure 1.1: Aerodynamic models for analysis of wind turbines.

Within the thesis, these methods have been used for studying the applicability of the sailwing concept to wind turbine rotors.

Flexible wings have been the central topic of many research projects. Different techniques have been applied to bring flexibility to conventional rigid wings. They can be categorized into two groups: active and passive. In active control configurations like morphing wing [1] or wing frames employing telescopic spars [2], actuators are used to bring flexibility to the wing. But in passive control concepts, the wing configuration possesses some intrinsic flexibility and its capability to adapt itself to the flow does not depend on the use of actuators. Membrane wings provide an alternative to conventional rigid wings where the wing surface is made of shells, i.e. thin-walled structures with bending stiffness. Membrane structures can effectively carry the external load over wide spans (e.g. stadium roofs) via in-plane stresses. Membrane wings could be used in design of Micro Air Vehicles (MAVs) [3, 4], airplane models [5] or windmills [6]. They have certain favorable characteristics compared with conventional rigid wings. Because of their flexibility, they are able to adapt to the surrounding flow field, which has the following advantages: From the aerodynamics point of view, membrane wings have a higher lift curve slope, higher maximum lift coefficient and higher lift to drag ratio compared to an equivalent rigid wing [5, 7, 8]. Delayed stall to higher angles of attack is another advantage of membrane wings [7]. From the structural dynamics point of view, there is a load reduction for membrane wings in unsteady flow cases [9]. However, because of self-excited vibrations, membrane wings might show a transient response even in steady state flow conditions [10].

Numerous studies on membrane wings have been carried out to examine their performance in MAV applications or with the goal of developing a better understanding of the mammalian flight. Shyy et al. [11] performed 2D analysis of a membrane-top airfoil concept in MAV flying regime, demonstrating a more stable lift coefficient compared with rigid airfoils. Another study on membrane wings for MAVs by Lian et al. [12] studied laminar-turbulent transition for a flexible airfoil, with only a portion of the upper surface formed by the membrane, showing self-excited vibration at $\alpha = 4°$, with comparable lift and drag coefficient to the rigid airfoil. Song et al. [13] performed an experimental and analytical study of a low aspect ratio rectangular membrane wing with fixed supports at the leading and trailing edge for a broad range of angles of attack from -20 to 60 degrees. In a numerical high-fidelity study for a single-layered membrane wing airfoil at MAV flying regime, Gordnier [14] studied the effect of membrane rigidity and pre-stress on airfoils aerodynamic characteristics and dynamic response for different combinations of angle of attack, Reynolds number, membrane rigidity and pre-strains. Different vibration modes were observed for the studied cases, as well as improvement in the lift coefficient

because of the introduced camber in the airfoil due to membrane's flexibility.

Research on the Sailwing concept was originally initiated at Princeton University during the 1970s with an interest in determining the applicability of this design as an auxiliary lifting device. Schematic presentation of the sailwing is shown in Fig. 1.2. A rigid mast forms the leading edge section of the wing. To support the upper and lower membranes, depending on the span of the wing a number of ribs are mounted along the span. Upper and lower membranes are joined together at the trailing edge via a pre-stressed edge cable.

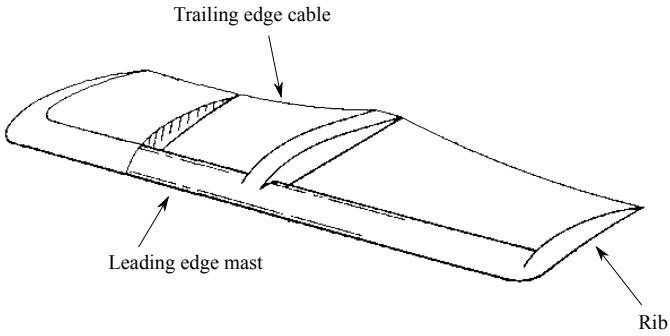

Figure 1.2: The Sailwing construction concept, from [15]

Later, during the 1980s, the application of the sailwing concept to wind energy systems was explored by the Princeton windmill group. The final progress report of the group states (Maughmer [6]): "*the sailwing rotor continues to be highly competitive in performance with its rigid-bladed counterparts and yet enjoys the benefits of simpler construction and lower costs*".

Analysis of the membrane blade consists of three major steps. They are represented in Fig. 7.3 for a sample section. In the form-finding step, the equilibrium shape in the absence of external loading is calculated. This corresponds to the shape of the wing at the beginning of the Fluid-Structure Interaction (FSI) simulation. Then in the FSI analysis, the interaction between the membrane and the fluid flow is simulated. FSI analysis is followed by evaluating the design in terms of aerodynamic and structural characteristics of the blade. The cycle could be repeated for a new design to realize a better aerodynamic performance of the blade.

For a membrane blade, the structural response (and thus the final form of the blade in operating condition) depends on aerodynamic loading, whereas the loading itself depends on the blade's shape; thus, a two-way coupled FSI sim-

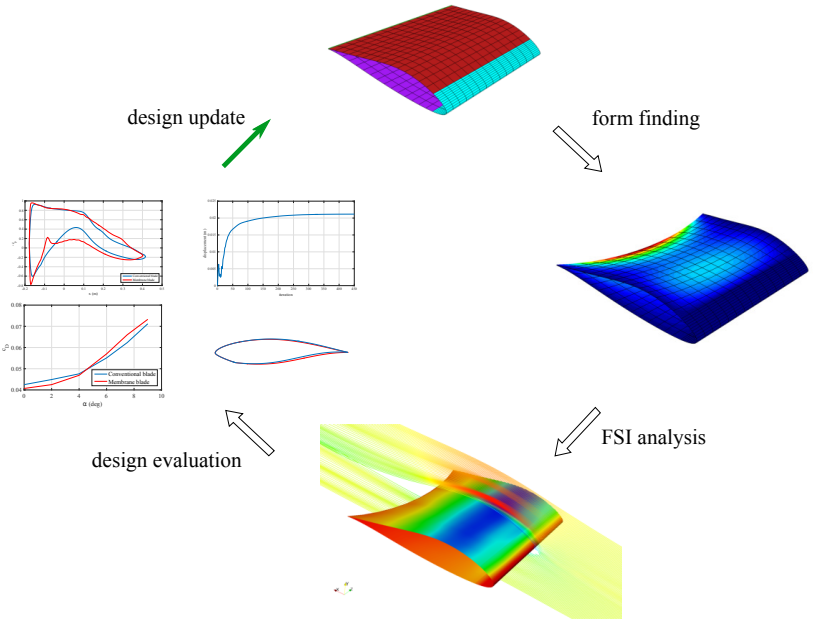

Figure 1.3: Analysis workflow for the membrane blade

ulation is necessary to analyze the characteristics of a membrane wing. Many parameters influence the overall performance of the sailwing, which include pre-stresses of the membranes in spanwise and chordwise directions, the pre-stress of the trailing-edge cable and material properties like elasticity modulus, density, Poissons ratio for different structural parts, etc. To choose a proper set of pre-stresses in order to obtain optimized performance at the design point, a comprehensive parameter study should be performed. Taking into account that FSI simulations are computationally expensive and time-consuming, a high-fidelity FSI analysis with detailed flow simulation is not the best choice during early phases of the design process. Models of lower complexity are unavoidable for performing a comprehensive design space exploration at a reasonable cost. The sequence of the analysis of the membrane blade concept using multi-fidelity FSI analysis is illustrated in Fig. 1.4.

The structure of the thesis is as follows:
Chapter 2 is about the blade element momentum (BEM) method. It explains the steady and unsteady BEM and the structural modeling of rotor blades using

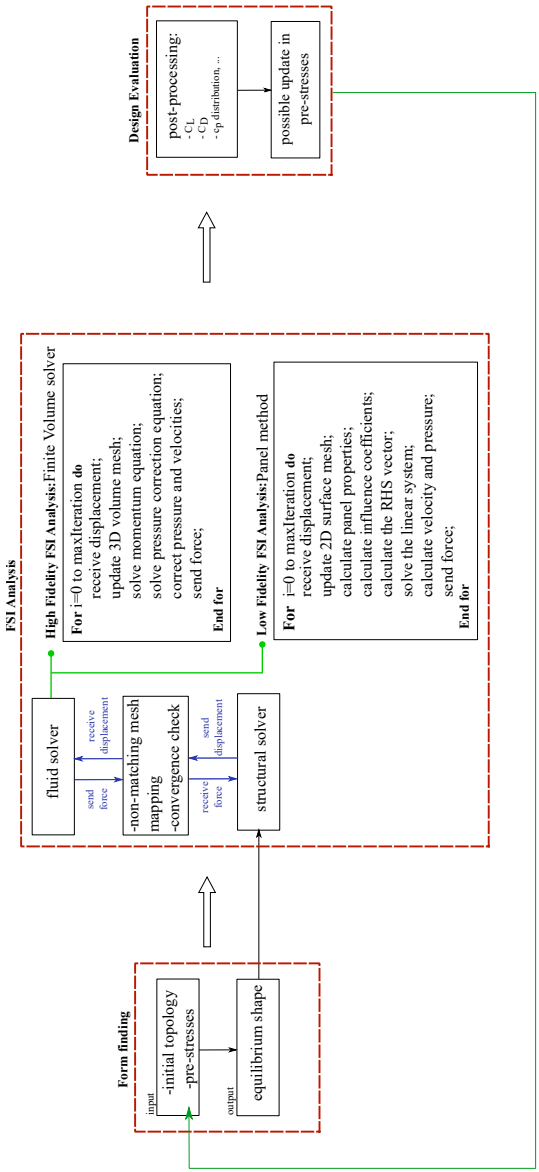

Figure 1.4: Schematic representation of the multi-fidelity analysis work flow.

beam elements. The presented structural solver is coupled with the BEM solver to construct a tool for aeroelastic analysis of wind turbine rotors.

In chapter 3, the vortex panel method is explained. It starts with the two-dimensional panel method and continues with steady three-dimensional and unsteady three-dimensional implementation, taking into account the wing or rotor's kinematics. The implemented panel code is tested for examples including sudden acceleration of a wing, pitching oscillations of a wing and flow over a wind turbine rotor.

Chapters 4 and 5 include respectively the fundamentals of computational fluid dynamics and the finite element method. These two theory chapters are kept very brief. For more detail, references are made to some well-known literature in the respective fields.

In chapter 6 the results of the low-fidelity FSI analysis workflow, using the panel method for solving the fluid problem are discussed and the comparison is made with the high-fidelity analysis approach using CFD. Besides that, the pre-stress dependent performance of the membrane blade concept is studied.

Chapter 7 is devoted to the membrane blade concept. The chapter presents the analysis of the membrane blade concept in three levels. In the first level, the membrane blade concept is studied in non-rotating uniform flow condition. Multi-fidelity FSI analysis is performed for the steady state situation. Unsteady FSI analysis of the membrane blade is also performed in non-rotating condition. In the second level, a workflow is introduced for the analysis of the membrane blade via panel-BEM coupling. The method combines the blade element method with 2D and 3D panel method for analyzing the performance of the membrane blade. At each FSI iteration the proposed method utilizes the three-dimensional panel method solver (Section 3.2) for calculating the loading from the fluid side in order to update the shape of the membrane blade and the two-dimensional panel method solver (Section 3.1) for calculating the lift and drag coefficient for the membrane blade sections which are used for BEM calculations. Finally, the performance of the membrane blade is analyzed in rotating configuration. In all three levels, comparison of the membrane blade's performance with its equivalent baseline rigid blade is made.

Lastly, concluding remarks are made in chapter 8.

2 *Blade Element Momentum Method*

This chapter discusses the theory and development of a solver for aeroelastic analysis of wind turbine rotor blades. It uses the blade element momentum (BEM) method for determining the loading on the blade in both steady and unsteady operating conditions. The unsteadiness of the loading might, on one hand, be due to changes in parameters controlling the turbine's operation like the rotational speed of the rotor or the pitch angle of the individual blades. On the other hand wind shear and atmospheric turbulence play a major load in the unsteadiness of the loading on a wind turbine. They are both included in evaluating the loading using BEM. Fluctuation of the wind speed component in the atmospheric boundary layer is modeled based on Mann's method [16, 17]. On the structural side, the blades are modeled using linear beam elements [18] and modal decomposition is used for dynamic analysis of the blade.

The implemented BEM solver is verified against the results obtained from Qblade [19] for the NASA-Ames Phase VI wind turbine (Appendix B). A very good agreement between the results is observed. Finally, the obtained results for unsteady cases like blade's pitching are presented as well as the aeroelastic response of the blade to unsteady loading due to wind shear and atmospheric turbulence.

2.1 Flow Over Airfoils

Airfoils are geometric profiles used to create lift. For the case of flow over an airfoil, the lift force (L) is quite larger than the drag force (D):

$$L >> D \tag{2.1}$$

Fig. 2.1 shows a sample airfoil with some of the term used in describing airfoil's geometry:

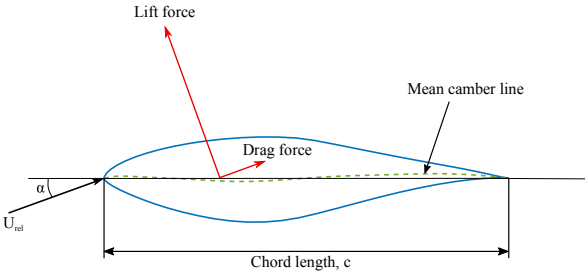

Figure 2.1: Airfoil terms and the forces acting on an airfoil section.

- **Chord Line**: The straight line connecting the leading edge and the trailing edge of an airfoil. Its length (c) is used as the characteristic length in airfoil calculations.
- **Camber Line**: The locus of the point midway between the upper and the lower surface of an airfoil.
- **Angle of Attack**(α): The angle between the relative velocity vector [1] and the chord line.

The forces acting on an airfoil can be resolved to a component perpendicular to the direction of the air flow, which is called the lift force, and a component in direction of the upcoming air flow, which is called the drag force (Fig. 2.1). The lift force is mainly a consequence of the pressure difference between the upper surface (suction side) and the lower surface (pressure side) of the airfoil, while the drag force is due to both the pressure difference on the two airfoil sides and the viscous friction force at airfoil's surface.

For a specific airfoil these forces depend on the angle of attack and the Reynolds number, which is the ratio of viscous to inertial forces:

$$Re = \frac{UL}{\nu} \tag{2.2}$$

where U is the inflow velocity, L is a characteristic length (chord length for 2D profile calculations) and ν is the kinematic viscosity of the fluid. Non-dimensional coefficients corresponding to the forces applied to an airfoil (or

[1] Velocity with respect to the frame attached to the airfoil

other 3D bodies) are defined via dimensional analysis. The 2D lift coefficient is defined as:

$$C_l = \frac{L}{\frac{1}{2}\rho|U|^2 c} \tag{2.3}$$

and the 2D drag coefficient is defined as:

$$C_d = \frac{D}{\frac{1}{2}\rho|U|^2 c} \tag{2.4}$$

Three-dimensional lift and drag coefficients are respectively designated by C_L and C_D. Another non-dimensional coefficient used in studying fluid flow over airfoils is the pressure coefficient:

$$c_p = \frac{p - p_\infty}{\frac{1}{2}\rho|U_\infty|^2} \tag{2.5}$$

As an example, lift and drag curves of the NACA0012 airfoil as a function of the angle of attack are shown in Fig. 2.2. The curves are obtained using XFOIL and show typical lift and drag characteristic of a generic airfoil. The lift coefficient at zero angle of attack is zero for this airfoil because NACA0012 is a symmetric profile. For lower values of angle of attack the flow is attached, lift

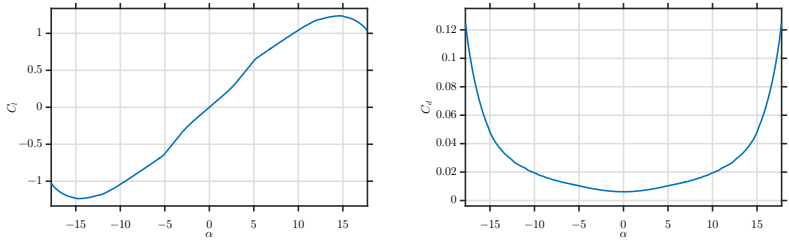

Figure 2.2: Lift and drag coefficient for the NACA0012 airfoil.

coefficient increases linearly with α and drag remains relatively low. For an ideal case of inviscid flow, the lift coefficient would continue to increase with α until an angle of attack of 90 degrees is reached. But, as a result of viscous forces, the slope of the lift curve decreases as the angle of attack and consequently the viscous forces increases. The airfoil increasingly stalls with the increase of angle of attack. Finally, stall happens at a specific critical angle of attack (typically between 10 and 16 degrees depending on the airfoil geometry and the Reynolds number [20] and flow separation on the suction side occurs.

At the stall point, the lift coefficient is at its maximum. After the stall point, lift coefficient starts to decrease and the drag coefficient increases rapidly. Power regulation in a stall controlled wind turbine is based on the decrease in the lift force after the stall point. With further increase in the angle of attack, the airfoil acts more and more like a flat plate.

2.2 1D Momentum Theory

The power extracted from the wind flow by an idealized rotor can be calculated using the Betz model. The Betz model is based on linear momentum theory used for analyzing the performance of propellers. The control volume used in the analysis is shown in Fig. 2.3. The model assumes incompressible, homogeneous, steady flow with no drag over a rotor with an infinite number of blades. Furthermore, uniform distribution of the thrust force over the rotor disc is assumed and the rotation in the wake is neglected.

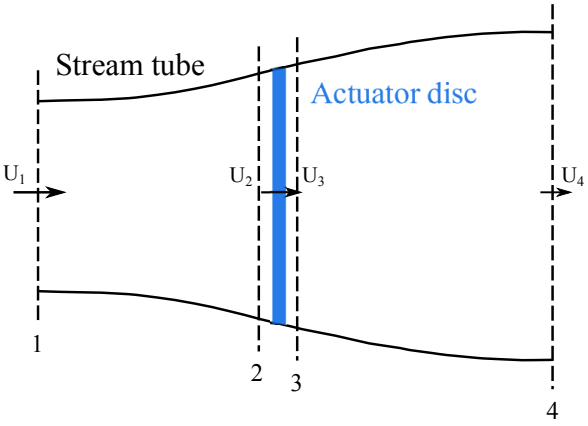

Figure 2.3: Non-rotating actuator disc model for a wind turbine rotor.

Taking the above assumptions, the Bernoulli equation can be written for the upstream region of the rotor (from section 1 to 2) and also for the downstream region of the rotor (section 3 to 4):

$$p_1 + \frac{1}{2}\rho U_1^2 = p_2 + \frac{1}{2}\rho U_2^2 \tag{2.6}$$

and

$$p_3 + \frac{1}{2}\rho U_3^2 = p_4 + \frac{1}{2}\rho U_4^2 \tag{2.7}$$

It is also assumed that the pressure far away from the rotor is equal to the free-stream pressure ($p_1 = p_4$) and that the velocity does not change across the rotor ($U_2 = U_3$).

The thrust force applied to the rotor can be found by applying the conservation of linear momentum to the presented control volume in Fig. 2.3:

$$T = U_1(\rho A_1 U_1) - U_4(\rho A_4 U_4) = \dot{m}(U_1 - U_4) \tag{2.8}$$

where A_i is the cross-section area of the corresponding section and $\dot{m}$ is the mass flow rate. The thrust force is the net force applied by the wind on the rotor in the horizontal direction. It can also be calculated from the pressure difference on the two sides of the rotor:

$$T = A(p_2 - p_3), \tag{2.9}$$

where $A = A_2 = A_3$ is the rotor area. Solving equations 2.6 and 2.7 for $(p_2 - p_3)$ and inserting it into equation 2.9, yields:

$$T = \frac{1}{2}\rho A_2(U_1^2 - U_4^2) \tag{2.10}$$

equating equations 2.8 and 2.10 and replacing the mass flow rate by $\rho A_2 U_2$, one obtains:

$$U_2 = \frac{U_1 + U_4}{2} \tag{2.11}$$

which states that the velocity at the rotor plane is the average of the free stream and downstream velocities. Defining the axial induction factor simplifies the description of velocity at different sections. The axial induction factor is a non-dimensional parameter describing the decrease of wind velocity from the upstream region to the rotor plane:

$$a = \frac{U_1 - U_2}{U_1} \tag{2.12}$$

The velocity at different section can be written in terms of the free stream velocity (U_1) and the induction factor (a):

$$U_2 = U_1(1 - a) \tag{2.13}$$

$$U_4 = U_1(1 - 2a) \tag{2.14}$$

The velocity at the rotor plane decrease as the induction factor increases from 0. For $a = 0.5$ wind velocity at the rotor becomes zero and the theory in not applicable anymore.

Major parameters regarding rotor performance can now be described in terms of the induction factor and the free stream velocity (U_1) which is designated by U from now on. The Power generated by the idealized rotor in the 1D momentum theory is equal to thrust time velocity:

$$P = \frac{1}{2}\rho A(U_1^2 - U_4^2)U \tag{2.15}$$

Substituting U_2 and U_4 form equations 2.13 and 2.14 the Power reads:

$$P = \frac{1}{2}\rho A U^3 4a(1-a)^2 \tag{2.16}$$

The performance of the rotor can be quantified via the non-dimensional power coefficient:

$$C_P = \frac{\text{Generated power}}{\text{Available power in wind}} = \frac{P}{\frac{1}{2}\rho A U^3} \tag{2.17}$$

which is equal to:

$$C_P = 4a(1-a)^2 \tag{2.18}$$

Setting the derivative of C_P with respect to a equal to zero, the maximum theoretical power of a wind turbine can be calculated. It could be seen that C_P is maximum at $a = \frac{1}{3}$, and its maximum value is:

$$C_P(a = \frac{1}{3}) = \frac{16}{27} \approx 0.593 \tag{2.19}$$

It implies that with the previously mentioned idealizing assumptions, a wind turbine cannot extract more than about 59% of the kinetic energy of the wind passing through its rotor plane.

Similar to the power coefficient, the thrust coefficient is defined as the ratio of the actual thrust acting on the rotor to the theoretically maximum force the airflow with the velocity of U could exert on a disc of area A:

$$C_T = \frac{T}{\frac{1}{2}\rho U^2 A} = 4a(1-a) \tag{2.20}$$

For the case of optimal power output ($a = \frac{1}{3}$), C_T is equal to $\frac{8}{9}$. Maximum thrust coefficient occurs at $a = \frac{1}{2}$. The simplified model used in 1D momentum theory is not valid for axial induction factors greater than 0.4.

Neglecting the rotation of the wake behind the rotor is one of the assumptions made in the 1D momentum theory of Betz. As a consequence of rotor's rotation, the flow in the downstream of the rotor rotates in the opposite direction of the rotor. The rotational velocity induced by the rotor in the downstream flow is designated by ω. This rotational velocity is small compared with the rotational velocity of the rotor itself(Ω). The angular induction factor is defined as one half of this ratio:

$$a' = \frac{\omega}{2\Omega} \tag{2.21}$$

With the definition of these parameters for describing the performance of a rotor and flow over an airfoil, the next section continues with the blade element momentum theory.

2.3 Blade Element Momentum Method

The Blade Element Momentum (BEM) method is the most common method used for calculating the wind load on wind turbines [21]. BEM calculations are very fast and they still provide satisfactory result provided that good airfoil data are utilized for the calculations. The inputs for the method include tabular lift and drag coefficient data at a number of Reynolds numbers and for a proper range of angles of attack, wind speed and turbine's operation-related inputs like pitch angle, yaw angle and rotational speed.

The method discretizes the blade into a number of radial elements (Fig. 2.4). Typically between 20-30 elements are used. The primary unknowns of the problem, solved using BEM method are the axial and tangential induction factors (a and a'). After solving for these unknowns the velocity at each section could be calculated together with the angle of attack. In the post processing step, the loading on the blade in the normal and tangential direction is calculated and major quantities like thrust, torque, bending moment and power could be calculated.

The basis of the BEM method lies on the calculation of the forces acting on each blade element using two different approaches and then equating them in order to derive the BEM method equations, which are solved iteratively. The two approaches are the momentum theory and the blade element theory:

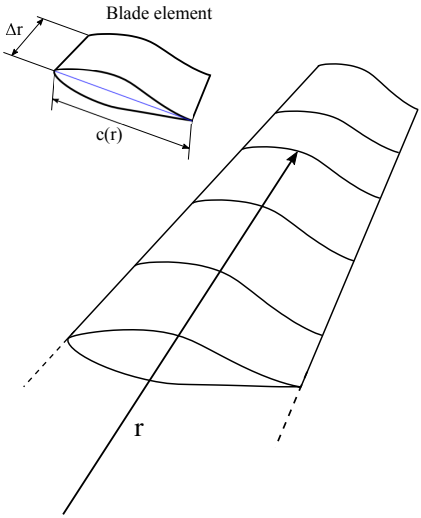

Figure 2.4: Discretization of the blade into radial elements.

2.3.1 Momentum theory

The momentum theory calculates the forces and the moment acting on each annular element based on the principle of conservation of linear and angular momentum. The control volume used for the calculations is shown in Fig. 2.5. The lateral boundaries of the control volume are stream tubes, meaning that no fluid flows through these boundaries and exchange of momentum takes place only at the upstream boundary in front of the rotor and the downstream boundary.

The thrust force acting on the annular element at the distance r from the root of the rotor could be calculated from conservation of linear momentum:

$$dT = [U - (1 - 2a)U]d\dot{m} \tag{2.22}$$

where $d\dot{m}$ is the mass flow rate across the control volume:

$$d\dot{m} = \rho U(1 - a)2\pi r dr \tag{2.23}$$

Inserting the mass flow rate from 2.23 into 2.22 the thrust force acting on the element reads:

$$dT = 4\pi r \rho U^2 a(1 - a)dr \tag{2.24}$$

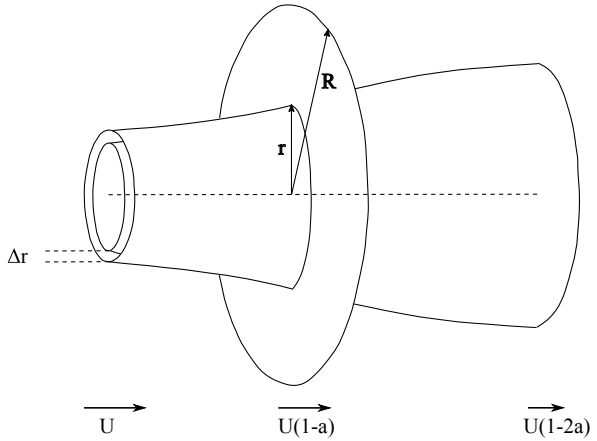

Figure 2.5: Control volume in the momentum method, from [18].

The moment acting on the annular element, dM, can also be calculated analogously using the principle of conservation of angular momentum:

$$dM = ru_\theta d\dot{m} \tag{2.25}$$

where u_θ is the azimuthal velocity:

$$u_\theta = 2\Omega r a' \tag{2.26}$$

Inserting the terms from 2.23 and 2.26 into 2.25 results in the moment acting on the annular element:

$$dM = 4\pi r^3 \rho U \Omega (1-a) a' dr \tag{2.27}$$

2.3.2 Blade Element Theory

Blade element theory calculates the thrust and moment acting on annular blade elements in terms of lift and drag coefficient, Reynolds number and the local angle of attack at each element. Flow in the radial direction is neglected in the calculations using blade element theory. The two-dimensional force calculations are done independently for each element, i.e. elements are not influenced by their neighbors.

As shown in Fig. 2.6, the relative velocity at each radial section can be decomposed into a component in the rotor plane and another component normal

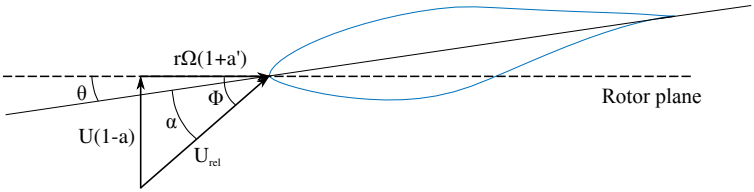

Figure 2.6: Decomposition of the relative velocity vector.

to the rotor plane. θ is the local pitch angle, which is the sum of blade's pitch angle (θ_p) and local twist at the section (β). By definition, the pitch angle of the blade is equal to zero when the chord line at the tip of the blade is parallel with rotor plane. Φ is the angle between the relative velocity vector and rotor plane:

$$\Phi = atan\left(\frac{(1-a)U}{(1+a')\Omega r}\right). \tag{2.28}$$

With the definition of these two angles, the local angle of attack reads:

$$\alpha = \Phi - \theta. \tag{2.29}$$

The forces acting on a generic blade element are shown in Fig. 2.7. The lift and the drag force acting on each element are calculated as a function of Reynolds number and angle of attack. From the lift and the drag forces the force acting normal to the rotor plane (contributing to the thrust force) and the tangential force (generating torque) for each element can be calculated:

$$\begin{bmatrix} p_N \\ p_T \end{bmatrix} = \begin{bmatrix} cos(\Phi) & sin(\Phi) \\ sin(\Phi) & -cos(\Phi) \end{bmatrix} \begin{bmatrix} L \\ D \end{bmatrix} \tag{2.30}$$

dividing equation 2.30 by $\frac{1}{2}\rho U_{rel}^2 c$ results in:

$$\begin{bmatrix} C_n \\ C_t \end{bmatrix} = \begin{bmatrix} cos(\Phi) & sin(\Phi) \\ sin(\Phi) & -cos(\Phi) \end{bmatrix} \begin{bmatrix} C_l \\ C_d \end{bmatrix} \tag{2.31}$$

where C_n and C_t are respectively the non-dimensional parameters for the force in normal and tangential direction:

$$C_n = \frac{p_N}{\frac{1}{2}\rho U_{rel}^2 c}, \tag{2.32}$$

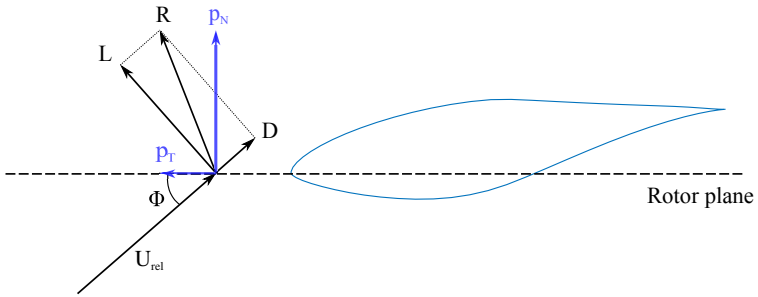

Figure 2.7: Decomposition of force acting on a generic annular element.

and

$$C_t = \frac{p_T}{\frac{1}{2}\rho U_{rel}^2 c}. \tag{2.33}$$

From the velocity triangle in Fig. 2.6, the relative velocity can be calculated as a function of both a and a':

$$U_{rel} = \frac{U(1-a)}{sin(\Phi)}, \tag{2.34}$$

$$U_{rel} = \frac{\Omega r(1+a')}{cos(\Phi)}. \tag{2.35}$$

With the parameters defined so far, the force and moment calculation based on blade element theory can be done. Since two-dimensional lift and drag coefficients are used for BEM calculation, p_N and p_T are both force per unit length and to calculate the total force they should be multiplied by element length (dr) and the number of blades (B):

$$dT = Bp_N dr \tag{2.36}$$

and

$$dM = rBp_T dr. \tag{2.37}$$

where B is the number of blades. Inserting p_N from 2.32 and U_{rel} from 2.34 into 2.36 the equation for the trust force on an annular element reads:

$$dT = \frac{1}{2}\rho B \frac{U^2(1-a)^2}{sin^2(\Phi)} cC_n dr. \tag{2.38}$$

Similarly, the moment can be calculated by inserting the corresponding terms into equation 2.37:

$$dM = \frac{1}{2}\rho B \frac{U(1-a)\Omega r(1+a')}{sin(\Phi)cos(\Phi)} cC_t r dr. \tag{2.39}$$

2.3.3 Solution Procedures

By equating equations 2.38 and 2.24 for the thrust force acting on the annular segment and equations 2.39 and 2.27 for the moment, induced tangential and angular induction factors can be calculated:

$$a = \frac{1}{1 + \frac{4sin^2(\Phi)}{\sigma C_n}} \tag{2.40}$$

and

$$a' = \frac{1}{\frac{4sin(\Phi)cos(\Phi)}{\sigma C_t} - 1} \tag{2.41}$$

where σ is the local solidity defined as the ratio of the annular element area to the area swept by the annular segment:

$$\sigma(r) = \frac{Bc}{2\pi r}. \tag{2.42}$$

The iterative solution procedure of the BEM method is summarized in Algorithm 1. For the first element, a and a' are usually initialized by zero. To improve convergence for the next elements, they could be initialized by the converged solution from their neighboring element.

```
for each element do
    initialize a and a';
    while convergence = false do
        calculate the relative flow angle (Eqn. 2.28);
        calculate angle of attack (Eqn. 2.29);
        interpolate C_l(α) and C_d(α) form tabular data;
        calculate C_n and C_t (Eqn. 2.31);
        calculate a and a' (Eqns. 2.40 and 2.41);
        check convergence;
    end
    do the post-processing;
end
```

Algorithm 1: Iterative BEM solution

2.4 Corrections Factors

In the previous sections, the basic BEM method and its underlying assumptions were discussed. Different correction factors are introduced to the method in order to improve BEM results and decrease the influence of the simplifications due to the assumptions of the model. They include corrections for heavily loaded rotors, yaw corrections, dynamic wake corrections, 3D corrections for airfoil data, etc. Applying the following two corrections is necessary for getting good results from BEM [18]:

2.4.1 Prandtl's Tipp Loss Factor

One of the underlying assumptions of the classical BEM theory is the infinite number of blades. Prandtl's loss factor corrects this assumption. The pressure on the blade side facing the wind is higher than the suction side, as a result, the fluid particles tend to flow around the tip of the blade from the wind facing side to the suction side where the pressure is lower. This phenomenon, which also happens at the tip of airplane wings, reduces power production at the tip of the blade and is most noticeable with fewer and wider blades [20]. The flow pattern in the wake of a rotor with a finite number of blades is different from the rotor with an infinite number of blades. For taking this into account, Prandtl introduced a correction factor, F, into equations 2.24 and 2.27:

$$dT = 4\pi r \rho U^2 a(1-a)F dr \tag{2.43}$$

and

$$dM = 4\pi r^3 \rho U \Omega (1-a) a' F dr \tag{2.44}$$

The correction factor (F) is calculated as:

$$F = \frac{2}{\pi} acos(e^{-f}) \tag{2.45}$$

where f is:

$$f = \frac{B}{2} \frac{R-r}{r sin(\Phi)} \tag{2.46}$$

using the above equations for equating annular thrust and moment derived from the momentum theory and the blade element theory, the equations for calculating the induction factors including tip loss effects read:

$$a = \frac{1}{1 + \frac{4F sin^2(\Phi)}{\sigma C_n}} \tag{2.47}$$

and

$$a' = \frac{1}{\frac{4Fsin(\Phi)cos(\Phi)}{\sigma C_t} - 1}. \tag{2.48}$$

2.4.2 Glauert's Correction Factor

The momentum theory is not valid for axial induction factors greater than approximately 0.4 [18]. For these cases empirical relations between thrust coefficient and the induction factor, like the one proposed by Spera[22], should be used:

$$C_T = \begin{cases} 4a(1-a)F & a \leq a_c \\ 4(a_c^2 + (1-2a_c)a)F & a > a_c \end{cases} \tag{2.49}$$

a_c is the critical axial induction factor and is approximately equal to 0.2. The thrust coefficient for an annular element, from the momentum theory reads:

$$C_T = \frac{dT}{\frac{1}{2}\rho U^2 2\pi r dr} = \frac{(1-a)^2 \sigma C_n}{sin^2(\Phi)}. \tag{2.50}$$

Equating the analytical equation with the empirical equation for $a > a_c$, results in:

$$4(a_c^2 + (1-2a_c)a)F = \frac{(1-a)^2 \sigma C_n}{sin^2(\Phi)} \tag{2.51}$$

and consequently the axial induction factor can be corrected for the cases where it exceeds the critical value:

$$a = \frac{1}{2}[2 + K(1-2a_c) - \sqrt{(K(1-2a_c)+2)^2 + 4(Ka_c^2 - 1)}] \tag{2.52}$$

where:

$$K = \frac{4Fsin^2(\Phi)}{\sigma C_n}. \tag{2.53}$$

2.5 Unsteady Blade Element Method

While the classical BEM method is sufficient for calculating the mean loading on a wind turbine or deriving the power curve for estimation of the annual energy production of the machine, an unsteady model is necessary for studying the aeroelastic response of the turbine. Wind shear, atmospheric turbulence and

the presence of the tower are among the factors contributing to the unsteadiness of the aerodynamic load on the rotor.

Taking wind shear and atmospheric turbulence into account, the BEM method should be used for each blade separately and the local undisturbed wind velocity for each annular element should be calculated as a function of time and section's position vector. The velocity components at the generic annular element are shown in Fig. 2.8.

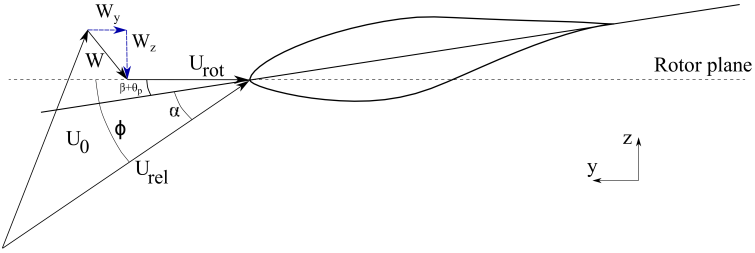

Figure 2.8: Decomposition of the relative velocity vector at a generic blade section.

$\mathbf{W}$ is the induced velocity and the relative velocity vector could be decomposed into three parts:

$$\begin{bmatrix} U_{rel_y} \\ U_{rel_z} \end{bmatrix} = \begin{bmatrix} U_y \\ U_z \end{bmatrix} + \begin{bmatrix} -\Omega r \\ 0 \end{bmatrix} + \begin{bmatrix} W_y \\ W_z \end{bmatrix}. \tag{2.54}$$

The relative velocity angle Φ reads:

$$\Phi = atan(\frac{U_{rel_y}}{U_{rel_z}}) \tag{2.55}$$

and the components of the induced velocity vector are computed as [18]:

$$W_z = \frac{-BLcos(\Phi)}{4\pi\rho r F|\mathbf{U} + f_g\mathbf{n}(\mathbf{n}\cdot\mathbf{W})|} \tag{2.56}$$

and

$$W_y = \frac{-BLsin(\Phi)}{4\pi\rho r F|\mathbf{U} + f_g\mathbf{n}(\mathbf{n}\cdot\mathbf{W})|} \tag{2.57}$$

where $\mathbf{n}$ is the vector normal to the rotor plane and f_g corresponds to Glauert correction factor:

$$f_g = \begin{cases} 1 & a \le a_c \\ \frac{a_c}{a}(2 - \frac{a_c}{a}). & a > a_c \end{cases}. \tag{2.58}$$

2.5.1 Dynamic Wake (Inflow) Model

The induced velocities calculated from equations 2.56 and 2.57 are quasi-static induced velocities, implying that the calculated velocities are valid when the wake is in equilibrium with the forces acting on the blade. In the case of transient conditions, there is a time delay before the velocities calculated from equations 2.56 and 2.57 are in equilibrium with the load. This time delay is proportional to the ratio of the rotor diameter to the undisturbed wind velocity [21].

Different engineering models are proposed for the modeling of dynamic inflow conditions [23, 24, 25]. In the later one, the induced velocities are modeled by two first-order ordinary differential equations:

$$W_{int} + \tau_1 \frac{dW_{int}}{dt} = W_{qs} + 0.6\tau_1 \frac{dW_{qs}}{dt} \tag{2.59}$$

and

$$W + \tau_2 \frac{dW}{dt} = W_{int}. \tag{2.60}$$

The two equations are separately solved for the two velocity components in y and z direction. W_{qs} is the quasi-static induced velocity, W_{int} is an intermediate value and W is the final filtered induced velocity. The time constants, τ_1 and τ_2, depend on the ratio of the rotor diameter to the undisturbed wind velocity and are computed as:

$$\tau_1 = \frac{1.1R}{(1 - 1.3a)U} \tag{2.61}$$

and

$$\tau_2 = (0.39 - 0.26(\frac{r}{R})^2)\tau_1. \tag{2.62}$$

For calculating the filtered induced velocities, first the quasi-static induced velocities should be calculated at each time step (equations 2.56 and 2.57). Then equation 2.59 should be solved for the intermediate induced velocities. Having W_{int} calculated, equation 2.60 is solved for the final value of the induced velocities.

2.5.2 Solution Procedure for Unsteady BEM

The solution procedure for the unsteady BEM method is presented in Algorithm 2.

```
initialize the position vector for all elements;
initialize a and a';
for each time step do
    for each blade do
        update blade's position;
        for each element do
            calculate the local wind velocity;
            calculate relative wind velocity (use the induced velocities
              form the previous time step);
            calculate the relative flow angle (Eqn. 2.55);
            calculate angle of attack (Eqn. 2.29);
            interpolate C_l(α) and C_d(α) form tabular data;
            calculate C_n and C_t (Eqn. 2.31);
            calculate the quasi-static induced velocities (Eqns. 2.56 and
              2.57);
            calculate the intermediate and final values of the induced
              velocities (Eqns. 2.59 and 2.60);
        end
    end
    do the post-processing;
end
```

Algorithm 2: Unsteady BEM solution procedure

2.6 Turbulent Inflow Condition for Unsteady Calculations

Generating the turbulent inlet conditions for unsteady simulations is based on the method developed by Mann at the Risø national laboratory for sustainable energy in Denmark [16, 17]. Detailed explanation of the algorithm can be found in mentioned publications. Most equations presented here are also from them, so direct reference is not made for all equations in the coming subsections. Turbulent flow consists of groups of eddies with different length scales. It is common to describe it in frequency domain, i.e. different length scales are described as waves with different frequencies and amplitudes. Wind

modeling starts also from this point in frequency domain (Fourier mode), the proposed method generates waves with amplitudes and phase angles such that after transforming these waves using inverse Fourier transform it ends up with the velocities which have the same statistics as in the atmospheric boundary layer. Generating the proper Fourier modes is based on the spectral tensor for incompressible isotropic turbulence. The velocity vector in the case of turbulent flow could be decomposed into a constant mean part and a fluctuating part:

$$\mathbf{u} = \mathbf{U} + \mathbf{u}' \tag{2.63}$$

In Mann's method, the fluctuating part of the velocity components is calculated for the grid points of an equidistant Cartesian grid (Fig. 2.9). It is done in three steps:

1. Evaluate the coefficients $C_{ij}(\mathbf{k})$.
2. Generate the random vectors $\mathbf{n}_j(\mathbf{k})$ and multiply.
3. calculate the fluctuating velocities by taking the inverse Fourier transform:

$$u_i(\mathbf{x}) = \sum_{\mathbf{k}} exp(i\mathbf{k}\cdot\mathbf{x})C_{ij}(\mathbf{k})n_j(\mathbf{k}) \tag{2.64}$$

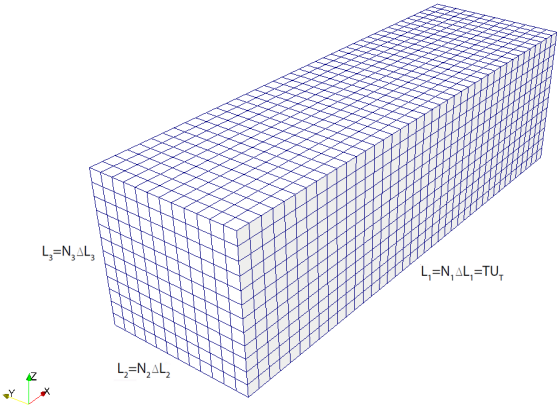

Figure 2.9: Precursor domain for generating turbulent inflow.

$\mathbf{x}$ here shows spatial coordinate of the corresponding node with $x_l = N_l \Delta L_l$ for $l = 1, 2, 3$ and N_l is number of cells in each spatial direction. $\mathbf{k}$ is the

vector of wave number $\mathbf{k} = [k_1, k_2, k_3]^T$, where each component of $\mathbf{k}$ is equal to:

$$k_i = \frac{2\pi m}{L_i} \tag{2.65}$$

where m ranges from $-N_i/2$ to $N_i/2$. Superposition of waves of different amplitude and phase is done in a random way to generate the random field of wind velocity fluctuations. The method assumes a Gaussian distribution for the velocity fluctuations. Gaussian distribution is applied by the vector $\mathbf{n}$ which contains independent Gaussian random variables with the mean value of zero and standard deviation of one. The matrix $\mathbf{C}$, which is a function of wave number vector contains the information about how much each Fourier mode should contribute to the total velocity field. It is different for isotropic and anisotropic turbulence and is explained in more detail in the sequel.

2.6.1 Isotropic turbulence

In isotropic turbulence, the mean velocity field is assumed to be constant and as a result, the shear force is zero. For incompressible isotropic turbulence the spectral tensor, proposed by Batchelor [26] is

$$\phi_{ij}(\mathbf{k}) = \frac{E(k)}{4\pi k^4}(\delta_{ij}k^2 - k_i k_j) \tag{2.66}$$

k here is the magnitude of wave number vector, $k = \sqrt{k_1^2 + k_2^2 + k_3^2}$, and $E(k)$ is energy spectrum suggested by von Karman [27]:

$$E(k) = \alpha \epsilon^{\frac{2}{3}} L^{\frac{5}{3}} \frac{L^4 k^4}{(1 + L^2 k^2)^{\frac{17}{6}}} \tag{2.67}$$

L is the length characterizing the scale of turbulence, α is Kolmogorov constant and ϵ is the rate of turbulent kinetic energy dissipation. The matrix $\mathbf{C}$ in Eqn. 2.64 is calculated using the following equation:

$$\mathbf{C}_{ij}(\mathbf{k}) = (\Delta k_1 \Delta k_2 \Delta k_3)^{\frac{1}{2}} \mathbf{A}_{ij}(\mathbf{k}) \tag{2.68}$$

where $\Delta k_l = 2\pi / L_l$ and $\mathbf{A}$ is calculated from square root factorization of the spectral tensor:

$$A_{ij}^* A_{ij} = \phi_{ij}. \tag{2.69}$$

For isotropic turbulence, the matrix $\mathbf{A}$ reads:

$$\mathbf{A}(\mathbf{k}) = \frac{\sqrt{E(k)}}{\sqrt{4\pi}k^2} \begin{bmatrix} 0 & k_3 & -k_2 \\ -k_3 & 0 & k_1 \\ k_2 & -k_1 & 0 \end{bmatrix} \tag{2.70}$$

The advantage of the isotropic model is that it describes the power spectral density well and at lower cost in comparison with the anisotropic model, but it has one major deficit. Since it is isotropic, the generated velocity components have pretty much the same magnitude in different spatial directions, which is not supported by experimental measurements. In reality, velocity fluctuations in the main flow direction are larger than fluctuations in transverse and vertical direction. Experimental Measurements suggest the following numbers for the ratios of the variances (σ) of velocity fluctuations in different directions:

$$\frac{\sigma_w^2}{\sigma_u^2} \approx 0.25 \tag{2.71}$$

$$\frac{\sigma_w^2}{\sigma_u^2} \approx 0.5 - 0.75 \tag{2.72}$$

but for isotropic turbulence we have:

$$\sigma_u^2 \approx \sigma_v^2 \approx \sigma_w^2 \tag{2.73}$$

which is normal for isotropic turbulence but does not agree with the reality. Anisotropic turbulence should be modeled in order to get the correct ratios.

2.6.2 Anisotropic turbulence

In the anisotropic case the mean velocity field is not constant and shear force is applied to eddies of different sizes. Eddies are assumed to be initially homogeneous. The initially homogeneous eddies are then stretched because of the shear force and their size and orientation changes, making them more and more anisotropic in time. The stretching of eddies does not continue for an infinite time and after a while eddies are broken and a steady state is reached. Eddy life time is the time that eddies face this stretching effect before they break up. Mann assumes the homogeneous eddies described by homogeneous spectral tensor in the last section as the initial condition of eddies and suggests a model for eddy life time in which eddy life time is not the same for eddies of all sizes, as in Townsend [28], but depends on eddy size. It is furthermore assumed that shear is linear such that dU/dz is constant and with the application of rapid distortion theory and linearization of the Navier-Stokes equation, the effect of shear in making initially isotropic eddies anisotropic is modeled.

Initially, the following relation between eddy life time and eddy size, which is proportional to $|k|^{-1}$, was assumed:

$$\tau(k) \propto \epsilon^{-\frac{1}{3}} k^{-\frac{2}{3}} \tag{2.74}$$

but this relation is not necessarily valid for eddies outside the inertial subrange. Mann has then constructed an alternative model for eddy lifetime which assumes that eddies of size k^{-1} are broken up mainly under influence of eddies of similar or smaller size. Characteristic velocity of these eddies is written as $\left(\int_k^\infty E(p)dp\right)^{\frac{1}{2}}$ and lifetime is assumed to be simply proportional to eddy size divided by this velocity:

$$\tau(k) \propto k^{-1}\left(\int_k^\infty E(p)dp\right)^{-\frac{1}{2}} \propto k^{-\frac{2}{3}}\left({}_2F^1(\frac{1}{3},\frac{17}{6},\frac{4}{3},-(kL)^{-2})\right)^{-\frac{1}{2}} \propto \begin{cases} k^{-\frac{2}{3}} & \text{if } k \to \infty \\ k^{-1} & \text{if } k \to 0 \end{cases} \tag{2.75}$$

E is von Karman Energy spectrum and ${}_2F^1$ is the hypergeometric function, appendix A. The algorithm from Numerical Recipes [29] is used for calculation of hypergeometric function. The above equation can be written as

$$\tau(k) = \Gamma\left(\frac{d\overline{u}}{dz}\right)^{-1}(kL)^{-\frac{2}{3}}\left({}_2F^1(\frac{1}{3},\frac{17}{6},\frac{4}{3},-(kL)^{-2})\right)^{-\frac{1}{2}}. \tag{2.76}$$

Γ is the parameter determining the level of anisotropy. For Γ equal to zero eddy life time is zero and eddies do not undergo stretching but remain isotropic. The anisotropy level is increased as Γ is increased. The ratios of velocity covariance in different directions which can be a measure of the level of isotropy depend only on Γ and not on L or $\alpha\epsilon^{\frac{2}{3}}$.

Because of the shear interaction between eddies of different sizes and orientations (Fourier modes) during eddy life time, figure 2.10, the wave number of eddies changes.

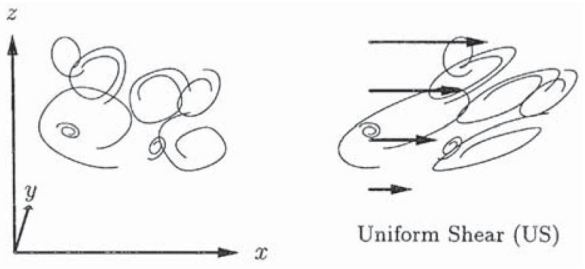

Figure 2.10: Uniform shear anisotropy from [17].

Using rapid distortion theory and by linearization of the Navier-Stokes equation, the change in wavenumber over time is found to be governed by the fol-

lowing equation:

$$\frac{dk_k}{dt} = -k_j \frac{\partial u_j}{\partial x_k}. \tag{2.77}$$

The mean velocity components in transversal and vertical direction are zero and for the main flow direction it depends only on height,

$$\mathbf{U} = (U, V, W) = (U(z), 0, 0). \tag{2.78}$$

As the initial condition for wave number vector, homogeneous Fourier modes are used $\mathbf{k}(t = 0) = (k_1, k_2, k_{30})$ and instead of time, non-dimensional time, β, defined as

$$\beta = \frac{d\bar{U}}{dz}\tau \tag{2.79}$$

is used. Solving Eqn. 2.77 with the above-mentioned initial condition yields the steady state wave number vector:

$$\mathbf{k}(t) = (k_1, k_2, k_{30} - \beta k_1) \tag{2.80}$$

Performing square root factorization of the spectral tensor with the above wave number vector, matrix $\mathbf{A}$ can be calculated for anisotropic turbulence: (more details could be found in [16])

$$A_{ij}(\mathbf{k}_0) = \frac{\sqrt{E(k_0)}}{\sqrt{4\pi}k_0^2} \begin{bmatrix} k_2\zeta_1 & k_{30} - k_1\zeta_1 & -k_2 \\ -k_{30} + k_2\zeta_2 & -k_1\zeta_2 & k_1 \\ k_2\frac{k_0^2}{k^2} & -k_1\frac{k_0^2}{k^2} & 0 \end{bmatrix} \tag{2.81}$$

k_0 is the magnitude of initial wave number vector and the two additional parameters are:

$$\zeta_1 = C_1 - \frac{k_2 C_2}{k_1} \tag{2.82}$$

and

$$\zeta_2 = C_2 + \frac{k_2 C_1}{k_1} \tag{2.83}$$

where

$$C_1 = \frac{\beta k_1^2 (k_0^2 - 2k_{30}^2 + \beta k_1 k_{30})}{k^2(k_1^2 + k_2^2)} \tag{2.84}$$

and

$$C_2 = \frac{k_2^2 k_0^2}{(k_1^2 + k_2^2)^{\frac{3}{2}}} tan^{-1}\left(\frac{\beta k_1 \left(k_1^2 + k_2^2\right)^{\frac{1}{2}}}{k_0^2 - \beta k_{30} k_1}\right). \tag{2.85}$$

To obtain an estimation of the parameters Γ, L and $\alpha\epsilon^{2/3}$ the explained spectral model is fitted to common wind spectra proposed in the literature, namely spectra from Kaimal and Simiu. Simultaneous least square fitting to Kaimal spectra leads to

$$\Gamma = 3.9, \tag{2.86}$$

$$L = 0.59z, \tag{2.87}$$

$$\alpha\epsilon^{2/3} = 3.2\frac{u_*^2}{z^{2/3}} \tag{2.88}$$

and

$$\Gamma = 3.8, \tag{2.89}$$

$$L = 0.79z, \tag{2.90}$$

$$\alpha\epsilon^{2/3} = 2.8\frac{u_*^2}{z^{2/3}} \tag{2.91}$$

for Simiu. u_* is friction velocity and z is the reference height for velocity measurements.

2.7 Structural Dynamics Modeling of Rotor Blades

The governing equation of motion for the dynamic system is:

$$\mathbf{M}\ddot{\mathbf{x}} + \mathbf{C}\dot{\mathbf{x}} + \mathbf{K}\mathbf{x} = \mathbf{F}. \tag{2.92}$$

Where $\mathbf{M}$, $\mathbf{C}$ and $\mathbf{K}$ are respectively the mass, damping and stiffness matrices and $\mathbf{F}$ is the load vector. The method proposed by Hansen [18] for structural dynamic modeling of blades is used in this work. It is based on modal superposition and approximates blade's displacement as a linear combination of its first three eigenmodes. They are the first two flapwise eigenmodes($1f, 2f$) and the first edgewise eigenmode($1e$). These eigenmodes are quantitatively demonstrated in Fig. 2.11.

Using these eigenmodes, blade's deformation in z direction reads:

$$d_z(x) = D_1 u_z^{1f}(x) + D_2 u_z^{1e}(x) + D_3 u_z^{2f}(x) \tag{2.93}$$

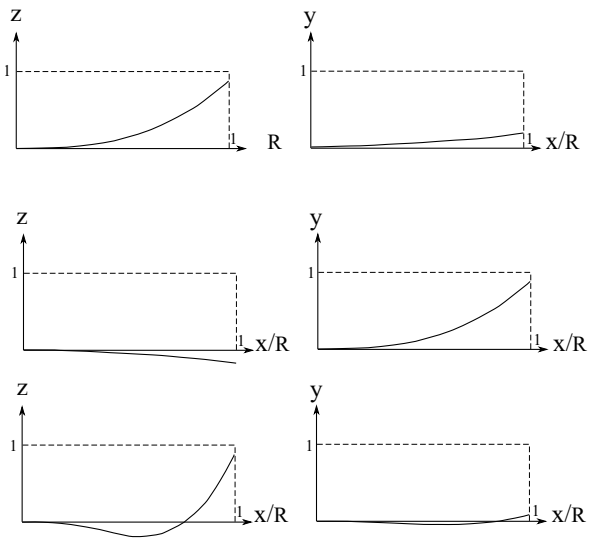

Figure 2.11: The first three eigenmodes of a generic blade, from [18].

Where the constants $D1$ to $D3$ are the generalized coordinates. Velocity and acceleration are calculated by taking the derivative of displacement with respect to time:

$$\dot{d}_z(x) = \dot{D}_1 u_z^{1f}(x) + \dot{D}_2 u_z^{1e}(x) + \dot{D}_3 u_z^{2f}(x), \tag{2.94}$$

$$\ddot{d}_z(x) = \ddot{D}_1 u_z^{1f}(x) + \ddot{D}_2 u_z^{1e}(x) + \ddot{D}_3 u_z^{2f}(x). \tag{2.95}$$

Displacement, velocity and acceleration in y direction are calculated analogously.

To solve the dynamic system using the generalized coordinates and eigenmodes, equation 2.92 should be solved for generalized coordinates and generalized mass, damping and stiffness matrices, as well as the generalized load vector, should be calculated. The equation of motion for the generalized coordinates is:

$$\mathbf{M}_g\ddot{\mathbf{D}} + \mathbf{C}_g\dot{\mathbf{D}} + \mathbf{K}_g\mathbf{D} = \mathbf{F}_g \tag{2.96}$$

where $\mathbf{D} = (D_1, D_2, D_3)$ is the vector of the generalized coordinates. The generalized force vector is calculated by multiplying the force vector by the

corresponding eigenmode and integrating it over the blade:

$$F_{g,i} = \int_0^R p_z(x) u_z^i(x) dx + \int_0^R p_y(x) u_y^i(x) dx \quad \text{for i=1,2,3} \tag{2.97}$$

u_z^i and u_y^i represent the components of the i^{th} eigenmode. The fist column of the mass matrix is equal to the force needed for unit acceleration of the first generalized coordinate ($\ddot{\mathbf{D}} = (1,0,0)$). The loading for such an acceleration is:

$$\begin{bmatrix} p_z \\ p_y \end{bmatrix} = \begin{bmatrix} m\ddot{d}_z(x) \\ m\ddot{d}_y(x) \end{bmatrix} = \begin{bmatrix} mu_z^{1f} \\ mu_y^{1f} \end{bmatrix}. \tag{2.98}$$

Inserting the loading form equation 2.98 into equation 2.97 yields:

$$\begin{bmatrix} m_{11} \\ m_{21} \\ m_{31} \end{bmatrix} = \begin{bmatrix} \int u_z^{1f}(x) m(x) u_z^{1f}(x) dx + \int u_y^{1f}(x) m(x) u_y^{1f}(x) dx \\ \int u_z^{1f}(x) m(x) u_z^{1e}(x) dx + \int u_y^{1f}(x) m(x) u_y^{1e}(x) dx \\ \int u_z^{1f}(x) m(x) u_z^{2f}(x) dx + \int u_y^{1f}(x) m(x) u_y^{2f}(x) dx \end{bmatrix} = \begin{bmatrix} GM_1 \\ 0 \\ 0 \end{bmatrix} \tag{2.99}$$

where the components m_{21} and m_{31} are vanished because of eigenmodes orthogonality condition. The two other columns of the mass matrix are similarly calculated. The mass matrix is a diagonal matrix because of eigenmodes orthogonality condition. The other two diagonal components are:

$$GM_2 = \int u_z^{1e}(x) m(x) u_z^{1e}(x) dx + \int u_y^{1e}(x) m(x) u_y^{1e}(x) dx \tag{2.100}$$

and

$$GM_3 = \int u_z^{2f}(x) m(x) u_z^{2f}(x) dx + \int u_y^{2f}(x) m(x) u_y^{2f}(x) dx. \tag{2.101}$$

The stiffness and damping matrices could be calculated analogously i.e. the first column of the stiffness matrix is for example equal to the necessary force vector for applying a unit displacement of $\mathbf{D} = (1,0,0)$ to the blade. These matrices read:

$$\mathbf{K} = \begin{bmatrix} \omega_1^2 GM_1 & 0 & 0 \\ 0 & \omega_2^2 GM_2 & 0 \\ 0 & 0 & \omega_3^2 GM_3 \end{bmatrix}, \tag{2.102}$$

and

$$\mathbf{C} = \begin{bmatrix} \omega_1 GM_1 \frac{\delta_1}{\pi} & 0 & 0 \\ 0 & \omega_2 GM_2 \frac{\delta_2}{\pi} & 0 \\ 0 & 0 & \omega_3 GM_3 \frac{\delta_3}{\pi} \end{bmatrix} \tag{2.103}$$

where ω_i is the i^{th} eigenfrequency and δ_i is the logarithmic decrement assigned to the i^{th} eigenmode. Inserting the coefficient matrices into equation 2.96 results in:

$$\begin{bmatrix} GM_1 & 0 & 0 \\ 0 & GM_2 & 0 \\ 0 & 0 & GM_3 \end{bmatrix} \begin{bmatrix} \ddot{D}_1 \\ \ddot{D}_2 \\ \ddot{D}_3 \end{bmatrix} + \begin{bmatrix} C_1 & 0 & 0 \\ 0 & C_2 & 0 \\ 0 & 0 & C_3 \end{bmatrix} \begin{bmatrix} \dot{D}_1 \\ \dot{D}_2 \\ \dot{D}_3 \end{bmatrix} + \begin{bmatrix} K_1 & 0 & 0 \\ 0 & K_2 & 0 \\ 0 & 0 & K_3 \end{bmatrix} \begin{bmatrix} D_1 \\ D_2 \\ D_3 \end{bmatrix} = \mathbf{F}_g \tag{2.104}$$

The matrix equation presents three uncoupled equations (due to eigenmodes orthogonality condition) which are solved independently using the Runge-Kutta technique for time integration.

2.8 Results

This section presents the results of using the developed BEM code for steady and unsteady analysis of the NASA-Ames Phase VI turbine (Appendix B). The unsteady BEM tool is coupled with the structural dynamic model presented in section 2.7 for performing the aeroelastic analysis of the blades. Steady, unsteady and aeroelastic analysis of the turbine follow in the next sections.

2.8.1 Steady Aerodynamic Analysis

This section presents the steady-state BEM results and compares them with the results obtained from Qblade [19]. Fig. 2.12 shows the extracted power by the rotor and the thrust force applied to the rotor for wind speed range of 4 to 16 m/s and and the pitch angle of 5 degrees.

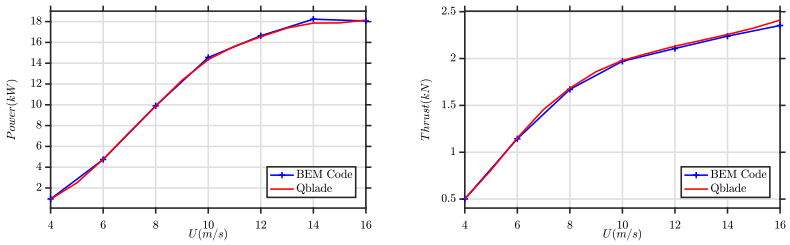

Figure 2.12: Power and the thrust force for different wind speeds.

Distribution of the loading on the blade in tangential and normal direction is presented in Fig. 2.13. Qblade discretized the whole blade including the cylindrical section, But in the Developed BEM the cylindrical part of the blade is neglected. A good match between Qblade results and the results from the developed BEM solver is observed.

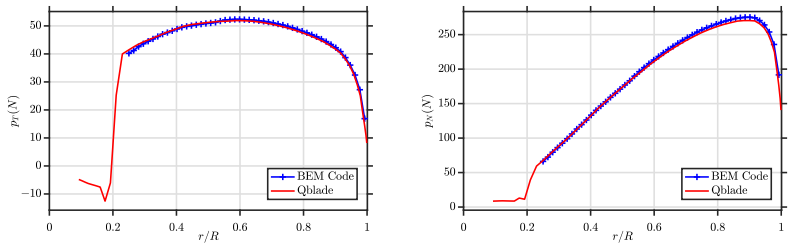

Figure 2.13: Loading distribution over the blade ($U = 8m/s$ and $\theta_p = 5°$).

Next, the distribution of the lift and drag coefficient over the blade is compared between the two codes (Fig. 2.14).

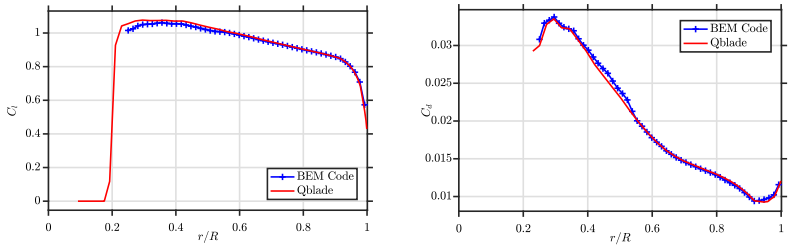

Figure 2.14: Lift and drag coefficient distribution over the blade ($U = 8m/s$ and $\theta_p = 5°$).

Finally the comparison is made for the axial induction factor (a) and the angle of attack over the blade (Fig. 2.15). The axial induction factor is the primary unknown in BEM method. The increase in the induction factor at the vicinity of blade's tip is because of the tip losses which are modeled via Prandtl's correction factor. The angle of attack for the current operational condition of the rotor ranges form about $11°$ at the root of the blade to about $3°$ at the tip. Therefore the blade is not stalled, since for the S809 airfoil stall starts at about $10°$ and the fully stalled flow is observed at $20°$ [30].

The NASA-Ames Phase VI turbine is a stall-controlled machine. With the

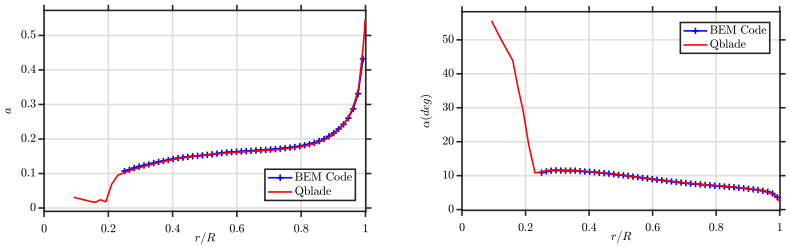

Figure 2.15: Axial induction factor and angle of attack distribution over the blade ($U = 8m/s$ and $\theta_p = 5°$).

increase of wind velocity, the blade is not pitched out of the wind as in pitch-controlled turbines. Consequently, the local angle of attack increases with the increase of wind velocity. The blades eventually stall at the designed wind speed to regulate the extracted power. The distribution of the local angle of attack along the blade for two different wind velocities is shown in Fig. 2.16. At the root of the blade the angle of attack increases by about 7° as wind velocity increase from $U = 8\,m/s$ to $U = 10\,m/s$. The local change in angle of attack decreases toward the tip of the blade with approximately 1.5° increase of the angle of attack at the tip, compared with the case of $U = 8\,m/s$.

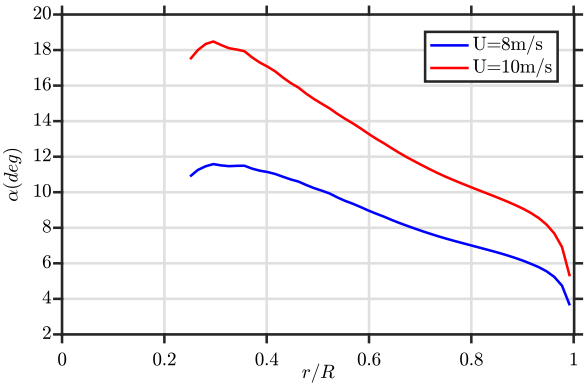

Figure 2.16: Angle of attack distribution for $U = 8\,m/s$ and $U = 10\,m/s$ at pitch angle of $\theta_p = 5°$.

2.8.2 Turbine's Unsteady Operation

Wind turbines continuously experience unsteady operating conditions with the main reason being unsteadiness in the wind hitting the blade due to both wind shear and atmospheric turbulence. The unsteady BEM solver enables the analysis of the instantaneous loading on the rotor at a reasonable computational cost. In the following, three scenarios of unsteady operating condition of wind turbines are presented.

2.8.2.1 Blade Pitching

In pitch-controlled wind turbines, blade's pitch angle (θ_p) is used to regulate the generated power. The Power could be decreased by pitching the blades out of the wind at higher wind speeds. As demonstrated in Fig. 2.17 the pitch angle in this example is increased from $3°$ at $t = 25\,s$ to $5°$ at $t = 25.5\,s$. It is then decreased back to $3°$ during $0.5\,s$ starting at $t = 35\,s$. The wind speed is $8\,m/s$.

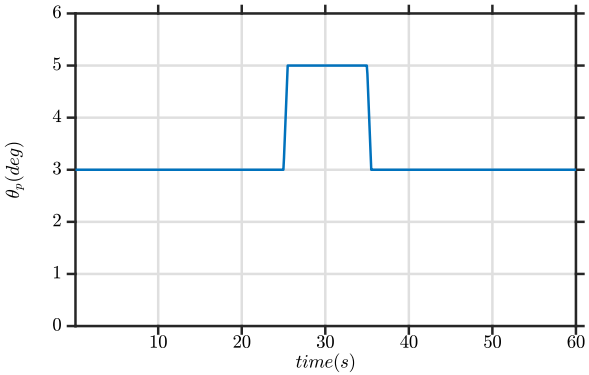

Figure 2.17: Time-dependent pitch angle.

The change in Power and thrust as a result of changing the pitch angle can be seen in Fig. 2.18. By increasing the pitch angle both the power and the thrust decrease. There is an initial overshoot right after changing the pitch angle, but after some time delay a new equilibrium state is reached. For this example, the time delay is about $5s$ for both the increase and the decrease of the pitch angle. The time delay increases with the decrease of wind speed, it depends on the ratio of rotor diameter to the wind speed.

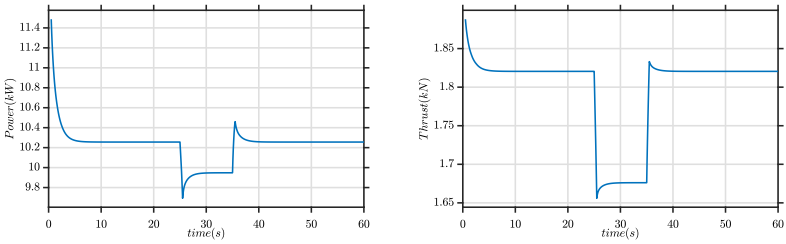

Figure 2.18: Change in power and thrust as a result of changing the pitch angle.

2.8.2.2 Wind Shear

In this second example the pitch angle is fixed at $\theta_p = 5^\circ$ but wind shear is taken into account rather than assuming a uniform wind velocity profile. The logarithmic profile suggested in [31] is used for the mean wind profile:

$$U(z) = \frac{u_*}{K} ln(\frac{z + z_0}{z_0}), \tag{2.105}$$

where u_* is the friction velocity, z_0 is the roughness length, and K is the von Karman constant. The roughness length is set to $z_0 = 0.01\,m$ (which corresponds to open areas covered with mown grass) and the friction velocity is calculated for a mean wind speed of $8\,m/s$ at hub height. For this example, the velocity at the rotor plane ranges forms $7.7\,m/s$ to $8.3\,m/s$. The difference between the minimum and maximum velocity is not very high (rotor diameter is $10\,m$), but it is still enough to observe oscillations in power and thrust at the frequency of rotor's rotation. Fig 2.19 shows the oscillation in the generated power and Fig. 2.20 shows the thrust applied on each blade. By definition, blade 1 is positioned at an azimuth angle of 0° at $t = 0\,s$. As it is expected for a 2-bladed rotor, because of the 180° angular distance between the blades, while the thrust of one blade is at its maximum value the other blade faces its minimum thrust.

2.8.2.3 Atmospheric Wind

This example takes both wind shear and atmospheric turbulence into account. The pitch angle is fixed at $\theta_p = 5^\circ$ and the mean wind speed at hub height is $8\,m/s$. The described method in section 2.6 is used for generating the fluctuating part of the velocity vector. Instantaneous wind field in front of the turbine is shown in Fig. 2.21. The wind velocity vector for each section of each blade

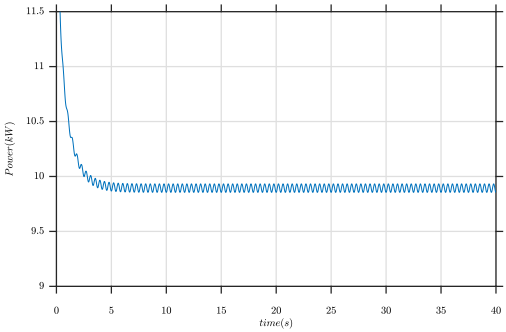

Figure 2.19: Influence of wind shear on the generated power.

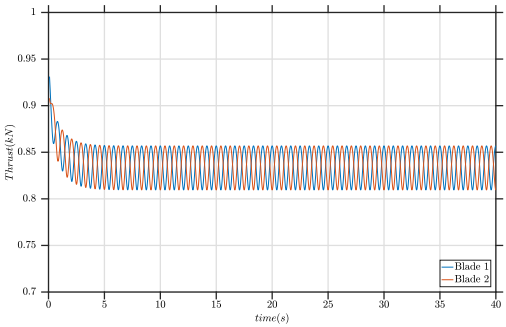

Figure 2.20: Influence of wind shear on the thrust applied to individual blades.

is calculated for every time step via bi-linear interpolation. The change in wind velocity for the section at the middle of the first blade over time is shown in Fig. 2.22. Because of the fluctuations in the wind field, the power output and the thrust applied on the blade have an oscillatory behavior. Next, they are compared with the case of using mean flow with no turbulent fluctuations.

The generated power by the rotor in plotted in Fig. 2.23. While for the mean wind profile the mean time-averaged power stays constant, the power oscillates about this mean value for the case of fluctuating wind.

Similar behavior is observed for the thrust applied on individual blades. The thrust applied on blade 1 is shown in Fig. 2.24. For the mean wind profile oscillation of the thrust force due to wind shear could be clearly observed, but it is not the case for the fluctuating wind case. Looking at the spectrum of

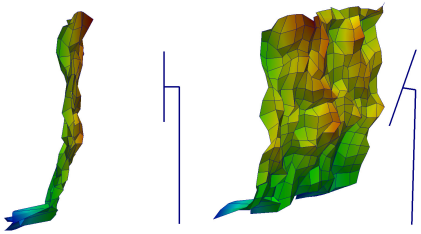

Figure 2.21: Three dimensional wind field in front of the turbine.

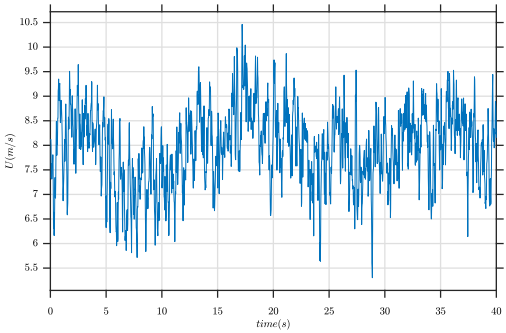

Figure 2.22: Change in wind velocity over time for a selected monitor point.

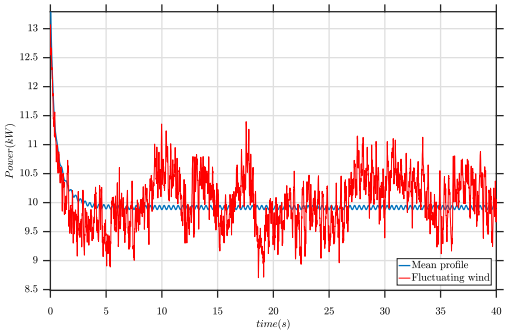

Figure 2.23: Comparison of the generated power.

the thrust force (Fig. 2.25) it is seen that for the uniform wind case, there is only one dominating frequency in the signal at $f = 1.196\,Hz$ which is the frequency of blade's rotation. For the fluctuating wind case on the other hand, the

frequency of blade's rotation has still the maximum amplitude, but other frequencies have a higher contribution to the thrust force compared with the mean profile case. Taking all these frequencies into account is crucial for fatigue life analysis of the blade and other mechanical components of the turbine.

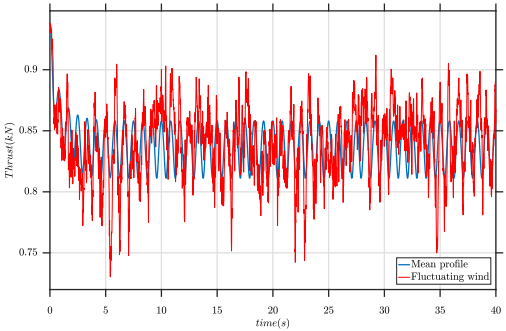

Figure 2.24: Comparison of the thrust force on blade 1.

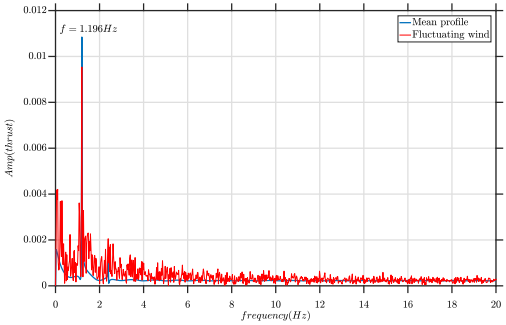

Figure 2.25: Fourier transform of the thrust on blade 1.

2.8.3 Aeroelastic Analysis

The aeroelastic response of the blades to unsteady loading due to atmospheric turbulence and wind shear is studied in this section. The same operating conditions as in the last example (section 2.8.2.3) holds for this example. The generalized forces applied to the first blade is presented in Fig. 2.26. The spectra of the applied forces is similar to the one shown in Fig. 2.25. Different frequencies are clearly visible in the generalized forces, which would not be

the case if only wind shear was taken into account. The consequence of exciting the structure with a rather wide range of frequencies could be seen in the aeroelastic response of the blade.

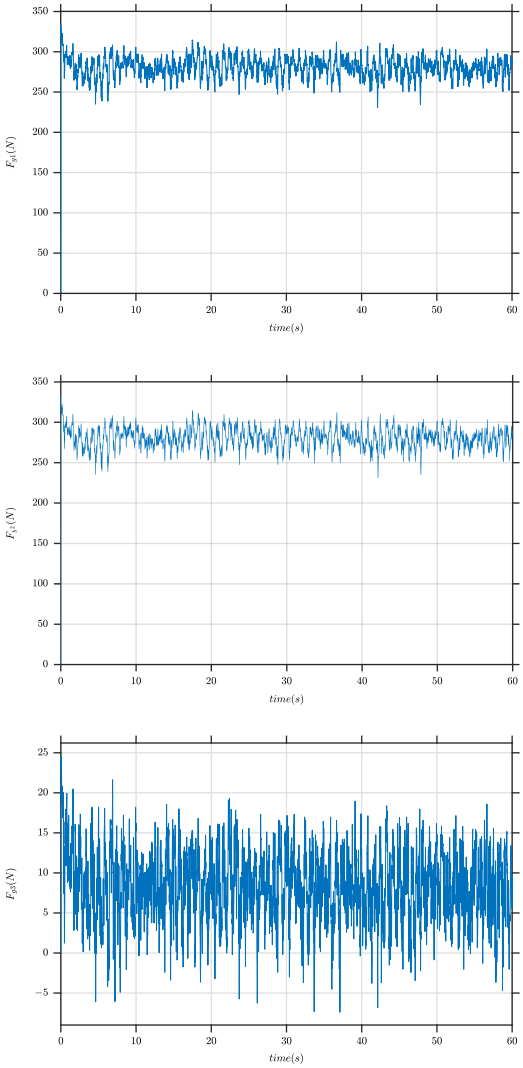

Figure 2.26: Generalized forces applied to blade 1.

The displacement at blade's tip due to wind shear is presented in Fig. 2.27. The dominant frequency for the loading this case is the frequency of rotor's rotation. Consequently, there is also only one frequency in blade's oscillations. After the initial response of the blade, it continues to oscillate in a periodic pattern. Taking atmospheric turbulence into account (Fig. 2.28) the aeroelastic response is entirely different. Due to the presence of eddies with different sizes in the atmospheric wind, the structure is excited with different frequencies including frequencies near the natural frequencies of the blade, therefore the beating phenomenon happens [32].

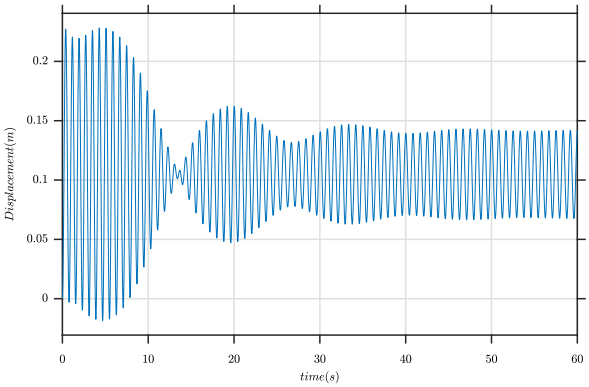

Figure 2.27: Tip displacement of blade 1 due to wind shear.

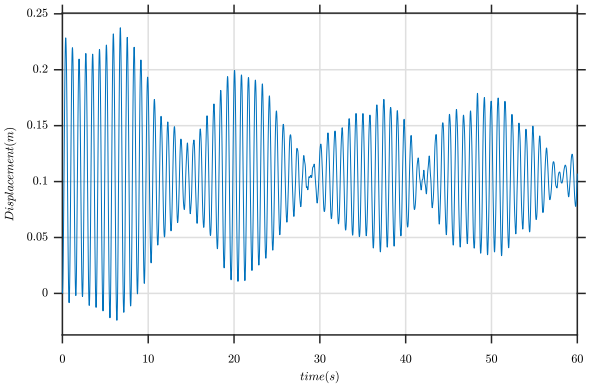

Figure 2.28: Tip displacement of blade 1 due to wind shear and atmospheric turbulence.

3 *Vortex Panel Method*

This chapter presents the theory behind the implemented panel method solver. The ultimate goal of implementing the panel method solver was to speed-up the FSI analysis for streamlined bodies within the applicability range of the panel method. The chapter starts with the two-dimensional panel method, followed by three-dimensional steady state and three-dimensional unsteady panel method. The implementations are based on the approach and the formulation in [33].

Verification of the implemented solver is made by comparing the obtained results with experimental results and numerical results form other solvers. Finally, examples such as pitching oscillation of a wing and flow over a wind turbine rotor are presented.

3.1 Two-Dimensional Panel Method

The velocity field for the case of irrotational, incompressible and inviscid flow can be represented by a velocity potential Φ. This is the basis for vortex panel method. The flow velocity in this case is nothing but the derivative of the potential and can be calculated from the potential in the following way:

$$u = \frac{\partial \Phi}{\partial x}, \tag{3.1}$$

$$v = \frac{\partial \Phi}{\partial y}. \tag{3.2}$$

The continuity equation for two-dimensional fluid flow with the above mentioned assumptions reads:

$$\frac{\partial u}{\partial x} + \frac{\partial v}{\partial y} = 0. \tag{3.3}$$

Inserting the velocities form equations 3.1 and 3.2 into the continuity equation (3.3) results in the continuity equation in terms of the potential:

$$\nabla^2 \Phi = 0. \tag{3.4}$$

There are two boundary conditions for solving this Laplacian equation:

1. At no-slip walls in the domain (e.g. on wing surface) the velocity component normal to the surface should vanish. This is called the zero normal flow boundary condition and is expressed in mathematical terms as:

$$\nabla \Phi \cdot \mathbf{n} = 0, \tag{3.5}$$

   where $\mathbf{n}$ is the vector normal to the surface.

2. the disturbance in the freestream flow caused by the elementary solutions should vanish with the increase of the distance, r, from the wing surface:

$$\lim_{\mathbf{r} \to \infty} \nabla \Phi = 0. \tag{3.6}$$

The so-called elementary solutions are used in the panel method to enforce the above conditions.

3.1.1 Elementary solutions

In the following the three basic elementary solutions are explained:

3.1.1.1 Point Source

A point source pumps fluid into the domain at the point it is located or sucks the fluid in if its strength is negative (it is then called sink). The velocity field induced by a point source is demonstrated in Fig. 3.1. The strength of point

source is designated by σ. The potential created by a two-dimensional point source located at (x_0, y_0) is:

$$\Phi(x,y) = -\frac{\sigma}{4\pi\sqrt{(x-x_0)^2+(y-y_0)^2}}. \tag{3.7}$$

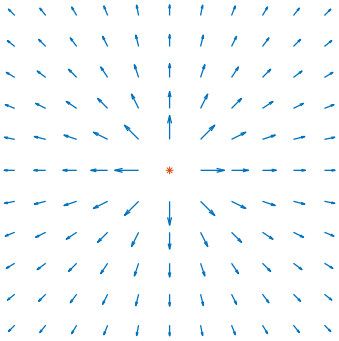

Figure 3.1: Velocity induced by a point source.

The velocity induced by the point source can be calculated by taking the derivative of the potential. The velocity components read:

$$u(x,y) = \frac{\partial\Phi}{\partial x} = \frac{\sigma(x-x_0)}{4\pi[(x-x_0)^2+(y-y_0)^2]^{\frac{3}{2}}} \tag{3.8}$$

and

$$v(x,y) = \frac{\partial\Phi}{\partial y} = \frac{\sigma(y-y_0)}{4\pi[(x-x_0)^2+(y-y_0)^2]^{\frac{3}{2}}}. \tag{3.9}$$

3.1.1.2 Point Doublet

Point doublet is a combination of point source and point sink as they approach each other. The velocity field around a point doublet is shown in Fig. 3.2. The potential due to a point doublet with a strength of μ is:

$$\Phi(x,y) = -\frac{\mu}{4\pi}(x-x_0)[(x-x_0)^2+(y-y_0)^2]^{-\frac{3}{2}} \tag{3.10}$$

and the induced velocities are:

$$u(x,y) = -\frac{\mu}{4\pi}\frac{(y-y_0)^2-2*(x-x_0)^2}{[(x-x_0)^2+(y-y_0)^2]^{\frac{5}{2}}} \tag{3.11}$$

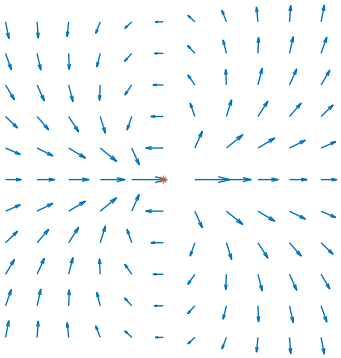

Figure 3.2: Velocity induced by a point doublet.

and

$$v(x,y) = \frac{3\mu}{4\pi} \frac{(x-x_0)(y-y_0)}{[(x-x_0)^2+(y-y_0)^2]^{\frac{5}{2}}}. \tag{3.12}$$

3.1.1.3 Point Vortex

Similar to the doublet term, the point vortex introduces rotation into the fluid flow about the point where it is located. The velocity introduced by the vortex term is shown in Fig. 3.3.

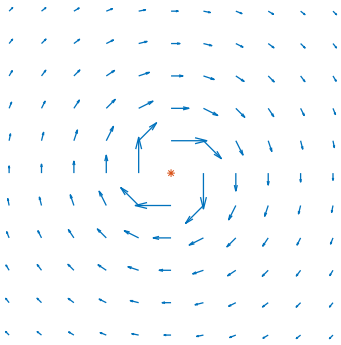

Figure 3.3: Velocity induced by a point vortex.

The vortex strength is designated by Γ. The induced potential by the vortex

term is:

$$\Phi(x,y) = -\frac{\Gamma}{2\pi} atan(\frac{y-y_0}{x-x_0}) \tag{3.13}$$

and the induced velocities read:

$$u(x,y) = \frac{\Gamma}{2\pi} \frac{y-y_0}{(x-x_0)^2+(y-y_0)^2} \tag{3.14}$$

and

$$v(x,y) = -\frac{\Gamma}{2\pi} \frac{x-x_0}{(x-x_0)^2+(y-y_0)^2}. \tag{3.15}$$

3.1.2 Numerical Panel Method

In panel method the surface of the wing, or the airfoil itself in the two-dimensional case, is discretized into a number of panels (Fig. 3.4). In order to represent the flow around the airfoil elementary solutions of the potential flow are distributed over the airfoil in either lumped or continuous way.

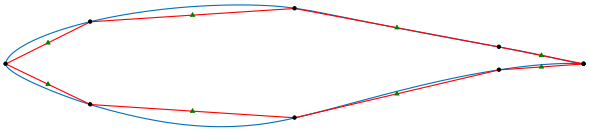

Figure 3.4: Discretization of the S809 airfoil (blue) into 8 panels (red): Panel nodes (circles) and collocation points (triangles).

The varieties for distribution of the elementary solutions include: point distribution (lumped), constant strength panels, linear strength panels and higher order strength distribution. Geometry of the panels could be either a flat line in first order description or a curved line for higher order models. Different types of elementary solution could be combined for describing the fluid flow around streamlined bodies. Point source, doublet and vortex are the three most commonly used ones. For the two-dimensional panel method, linear strength vortex distribution is used in this work with flat panels for geometry representation.

The velocity induced by a single linear-strength vortex panel with the start point 1 and end point 2 (Fig. 3.5) is calculated by integrating equations 3.14 and 3.15 over panel's length:

$$u(x_p,y_p) = \frac{1}{2\pi} \int_{x_1}^{x_2} \Gamma \frac{y_p-y}{(x_p-x)^2+(y_p-y)^2} dx$$

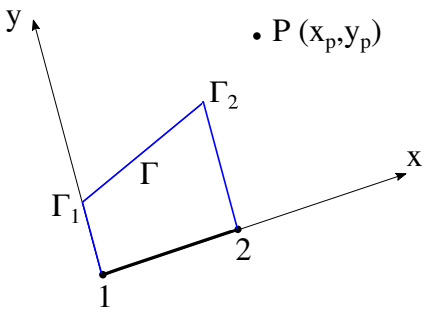

Figure 3.5: Linear vortex distribution on a generic 2D panel.

$$= \frac{1}{2\pi}\left([-\Gamma_1 atan(\frac{x_p - x}{z_p})]_{x_1}^{x_2} + \frac{\Gamma_2 - \Gamma_1}{l}[\frac{1}{2}y_p ln((x_p - x)^2 + (y_p - y)^2) - x_p atan(\frac{x_p - x}{z_p})]_{x_1}^{x_2}\right) \tag{3.16}$$

and

$$v(x_p, y_p) = -\frac{1}{2\pi}\int_{x_1}^{x_2} \Gamma \frac{x_p - x}{(x_p - x)^2 + (y_p - y)^2} dx$$

$$= -\frac{1}{2\pi}\left(\Gamma_1[\frac{1}{2}ln(x^2 - 2xx_p + x_p^2 + y_p^2)]_{x_1}^{x_2} + \frac{\Gamma_2 - \Gamma_1}{l}[-\frac{1}{2}ln(x^2 - 2xx_p + x_p^2 + y_p^2) + z_p atan(\frac{x_p - x}{z_p}) - x]_{x_1}^{x_2}\right) \tag{3.17}$$

where l is the length of the panel. The coordinates in panel's frame of reference must be used in the above equations. In panel method the strength of the elementary solutions (vortex strength at panel nodes in this case) are calculated in a way that the component of the total velocity vector at the collocation point of the panels in the normal direction vanishes.

There are two ways to enforce the zero normal flow boundary condition. It can be enforced either as a Dirichlet boundary condition by setting a constant value for the potential inside the body or as a Neumann boundary condition which deals with the derivative of the potential, i.e. the velocity. The latter approach is used to enforce the zero normal flow boundary condition at the collocation points. The collocation point of a panel is at the center of the panel (in the case of Dirichlet boundary condition the collocation points are shifted inside the body). The velocity at the i^{th} collocation point P_i (the numbering is presented in Fig. 3.6) is calculated by summing up the contribution of each panel to the

total velocity at this point with the free stream velocity:

$$\mathbf{u}(P_i) = \sum_{k=1}^{N} A_{ik}\Gamma_k + \mathbf{u}_\infty \tag{3.18}$$

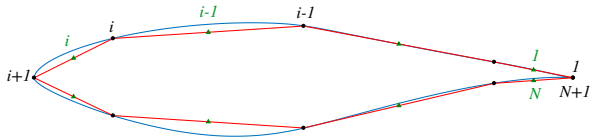

Figure 3.6: Panel nodes and collocation points numbering, respectively in black and green.

where N is the number of panels. The coefficients A_{ik} are all gathered in an $(N+1) \times (N+1)$ coefficient matrix $\mathbf{A}$. A_{ik} is equal to the velocity induced at collocation point i, by a unit vortex strength of the k^{th} panel and zero vortex strength at other panels. To set the total velocity in the normal direction to the panel to zero, the contribution of panels should cancel out that of the free stream velocity, for the i^{th} collocation point it reads:

$$(\sum_{k=1}^{N} A_{ik}\Gamma_k) \cdot \mathbf{n}_i = -\mathbf{u}_\infty \cdot \mathbf{n}_i. \tag{3.19}$$

Equation 3.19 should hold at every collocation point. Applying this equation to each collocation point results in a system of N equations with $N+1$ unknowns, which are the vortex strengths at panel nodes 1 to $N+1$. One more equation is needed in order to have a well-posed system of linear equations.

The Kutta condition provides the last equation necessary for solving the system. It states that: "*The flow leaves the sharp trailing edge of an airfoil smoothly and the velocity there is finite*" [33]. The Kutta condition implies that the circulation at the trailing edge should be zero. Two panels from the suction and the pressure side of the airfoil meet at the trialing edge, so there are two panel nodes located at the trailing edge. Zero circulation at the trailing edge is satisfied by enforcing:

$$\Gamma_{Trailing\ Edge} = \Gamma_1 + \Gamma_{N+1} = 0. \tag{3.20}$$

The set of N equation for zero normal flow at the collocation points and the one equation for enforcing the Kutta condition provide the linear system which

is solved for the $N+1$ vortex strengths. In the post-processing step the velocity at the points of interest, which are the collocation points in particular, is calculated. The pressure is then calculated from the steady state Bernoulli equation. Using the Bernoulli equation, the pressure coefficient reads:

$$c_p = \frac{p - p_\infty}{\frac{1}{2}\rho \left\|\mathbf{u}_\infty\right\|^2} = 1 - \frac{\left\|\mathbf{u}\right\|^2}{\left\|\mathbf{u}_\infty\right\|^2} \tag{3.21}$$

3.1.3 Results

The results obtained from the implemented two-dimensional panel code are presented in this section for the well-known NACA0012 airfoil. The pressure distribution over the airfoil for the angles of attack of 4 and 8 degrees are shown in Figs. 3.7 and 3.8 respectively. The reference data are from Mason [34].

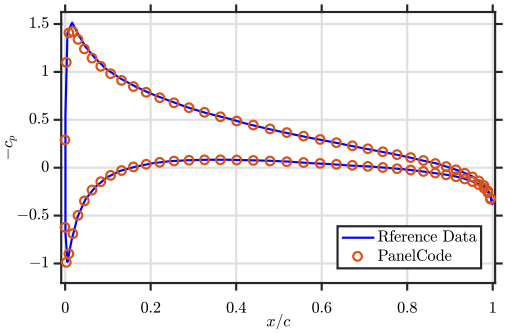

Figure 3.7: c_p distribution over the NACA0012 airfoil for $\alpha = 4.0°$.

Comparison of the two-dimensional lift coefficient with reference panel code data [34] as well as experimental results is made in Fig. 3.9. In the linear region of the lift curve both panel codes predict quite the same lift coefficient as measured in the experiments, but the results deviate form the experimental results as the angle of attack increases. At $\alpha = 10°$, panel code over-predicts the lift coefficient by about 8%.

The results form the implemented panel code match well with the reference panel code results from [34]. Overall, there is a good agreement between panel codes and experimental results for lower angles of attack, but obviously with further increase of the angle of attack and with the emergence of stall panel code results cannot be used.

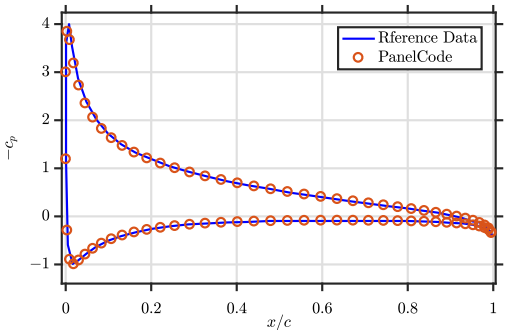

Figure 3.8: c_p distribution over the NACA0012 airfoil for $\alpha = 8.0°$.

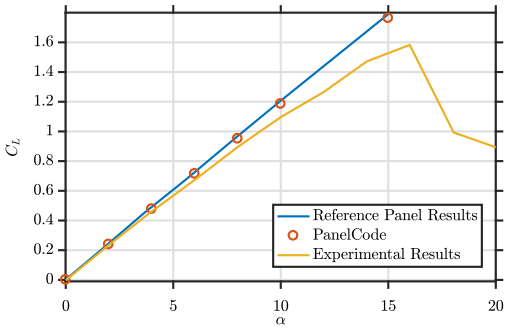

Figure 3.9: Two-dimensional lift coefficient for the NACA0012 airfoil.

3.2 Three-Dimensional Panel Method

For the three-dimensional implementation of the panel method source terms are combined with vortex rings. The addition of the source terms improves the numerical stability in solving the resulting linear system of equation. The geometry of the wing is described by first-order flat panels. The flow in the wake of the wing is presented by one row of wake panels starting from the trailing edge and extending far enough away from the wing (Fig. 3.10).

Each panel on the wing represents a constant source panel. In addition to the source terms the edges of each panel represent 4 line vortices. The edges of each wake panel represent 4 line vortices as well. These elementary solutions and the velocity induced by them are explained in the following:

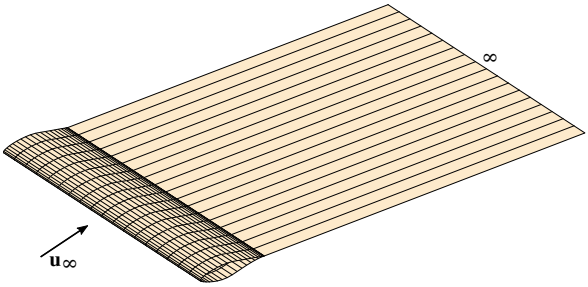

Figure 3.10: Discretization into wing and wake panels.

3.2.1 Quadrilateral Source

A generic panel with constant strength source distribution, σ, is shown in Fig. 3.11. The potential due to this element at point P, with the coordinates (x_p, y_p, z_p) in the panel coordinate system, is the integral of the potential due to point source terms over the entire panel surface:

$$\Phi(x,y,z) = \frac{-\sigma}{4\pi} \int_S \frac{dS}{\sqrt{(x_p - x)^2 + (y_p - x)^2 + z_p^2}}. \tag{3.22}$$

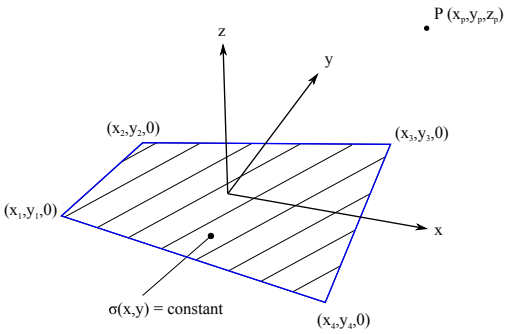

Figure 3.11: Quadrilateral source element.

The velocity induced by the element at point P is calculated by differentiating the potential:

$$\mathbf{u} = (\frac{\partial \Phi}{\partial x}, \frac{\partial \Phi}{\partial y}, \frac{\partial \Phi}{\partial z}). \tag{3.23}$$

Calculating the potential and the differentiation is a lengthy process, the formula for the velocity components are not included here to avoid clutter. They are available in [33].

3.2.2 Line Vortex

Fig. 3.12 shows a line vortex with a constant vortex strength (Γ). The velocity induced by the line segment (connecting point 1 to point 2) at point P is:

$$\mathbf{u} = K(\mathbf{r}_1 \times \mathbf{r}_2) \tag{3.24}$$

where

$$K = \frac{\Gamma}{4\pi|\mathbf{r}_1 \times \mathbf{r}_2|^2}\left(\frac{\mathbf{r}_0 \cdot \mathbf{r}_1}{r_1} - \frac{\mathbf{r}_0 \cdot \mathbf{r}_2}{r_2}\right). \tag{3.25}$$

$\mathbf{r}_0$ is the vector connecting point 1 to point 2 and r_1 and r_2 are respectively the magnitudes of the vectors $\mathbf{r}_1$ and $\mathbf{r}_2$.

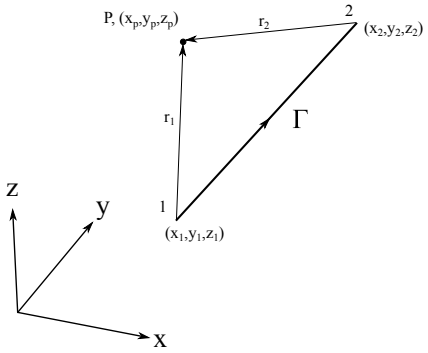

Figure 3.12: Straight line vortex.

A quadrilateral vortex ring consists of 4 connected vortex lines as in Fig. 3.13. The velocity induced by a vortex ring is the sum of the velocities induced by its 4 edges.

3.2.3 Zero normal flow boundary condition

The zero normal flow boundary condition (Eqn. 3.5) is enforced at the center of each wing panel (collocation points) using the Neumann's approach. The velocity at each collocation point is equal to the free stream velocity ($\mathbf{u}_\infty$) plus

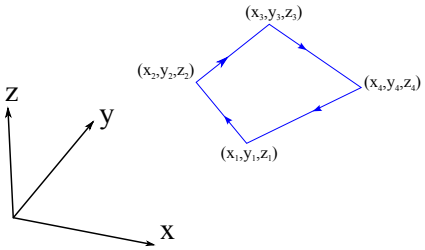

Figure 3.13: Quadrilateral vortex ring with constant strength Γ.

the contributions from wing panels and wake panels. For the i^{th} collocation point (P_i)the velocity reads:

$$\mathbf{u}(P_i) = \mathbf{u}_\infty + \sum_{k=1}^{N} C_{ik}\Gamma_k + \sum_{k=1}^{N_w} W_{ik}\Gamma_k + \sum_{k=1}^{N} B_{ik}\sigma_k \tag{3.26}$$

where N is the number of wing panels and N_w is the number of wake panels. The first summation is for the contribution of vortex rings on the wing, the second one is for the contribution of vortex rings in the wake panels and finally the third one is for the contribution of source terms on the wing. The value of the coefficient C_{ik} is equal to the velocity at the i^{th} collocation point induced by the k^{th} wing panel of unit strength, while all other panels have a vortex strength of zero. Similar comment could be made about W_{ik} for wake panels and B_{ik} for source panels on the wing. The velocity component normal to the i^{th} panel is the dot product of the velocity vector at P_i with the normal vector of the panel ($\mathbf{n}_i$). Performing the dot product and bringing the term due to the free stream stream velocity to the right hand side, the equation for enforcing the zero normal flow boundary condition for the collocation point number i reads:

$$\left(\sum_{k=1}^{N} C_{ik}\Gamma_k + \sum_{k=1}^{N_w} W_{ik}\Gamma_k + \sum_{k=1}^{N} B_{ik}\sigma_k\right) \cdot \mathbf{n}_i = -\mathbf{u}_\infty \cdot \mathbf{n}_i. \tag{3.27}$$

This equation holds for all collocation points, resulting in a linear system of N equations to be solved (The C++ linear algebra library, Armadillo [35], is used to solve the system). The unknowns in Eqn. 3.27 are the strength of source terms, panel vortex rings and wake vortex rings. The value of the strength of source terms is not solved for, but is assigned in advance:

$$\sigma_k = \mathbf{u}_\infty \cdot \mathbf{n}_k. \tag{3.28}$$

The Kutta condition in 3D is applied by setting the strength of the wake panels in terms of the neighboring wing panels in a way that the total circulation at the trailing edge vanishes (Fig. 3.14).

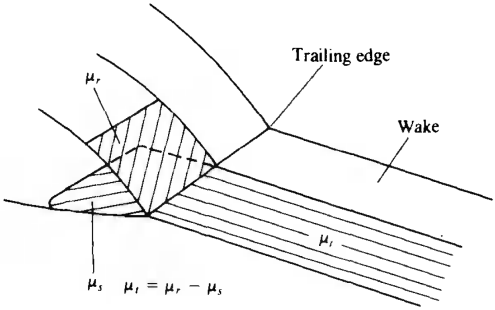

Figure 3.14: Applying the Kutta condition at the trailing edge, from [33].

Three panels intersect at the trailing edge. These are the wake panel and the two wing panels on the upper and lower surface of the wing. The Kutta condition is satisfied by setting the difference in the strength of the upper and the lower panel equal to wake strength:

$$\Gamma_w = \Gamma_{upper} - \Gamma_{lower}. \tag{3.29}$$

The strength of the vortex ring panels on the wing is calculated by solving the system of linear equations resulting form enforcing Eqn. 3.27 at each collocation point. As in the two-dimensional case, in the post-processing step the velocity at the points of interest, which are the collocation points in particular, and consequently the pressure (from Bernoulli equation) are calculated.

3.2.4 Results

The three-dimensional implementation of the panel code is verified against XFLR5 [36] results for two examples: a rectangular wing with an aspect ratio of 6.0 and a delta wing configuration. The obtained results are in good agreement with XFLR5 results in both cases. The two examples are presented in the following:

3.2.4.1 Rectangular Wing

The studied NACA0012 rectangular wing is discretized into circa 4000 panels. The convergence of the obtained lift coefficient with the increase of the number of panels is shown in Fig. 3.15.

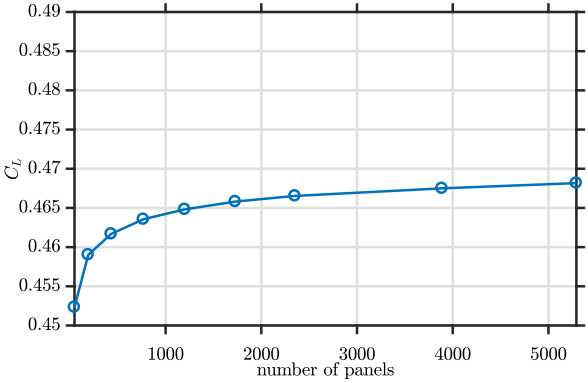

Figure 3.15: Convergence of the lift coefficient.

The comparison between the obtained lift and drag coefficient and XFLR5 results is made in Fig. 3.16.

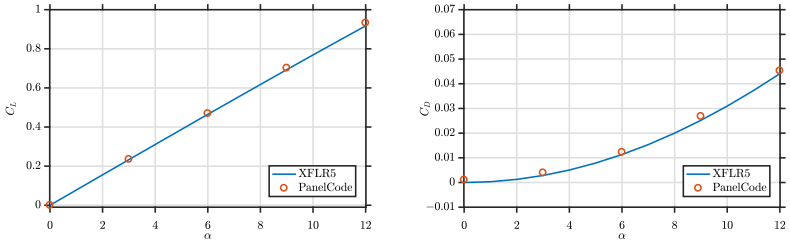

Figure 3.16: Comparison of the lift and drag coefficient for the rectangular wing.

Finally, the distribution of pressure coefficient at the mid-span section of the wing is compared for $\alpha = 3°$ and $\alpha = 6°$. For both lift and drag coefficient as well as for the pressure distribution, the obtained results from the implemented three-dimensional panel code match well with XFLR5 results.

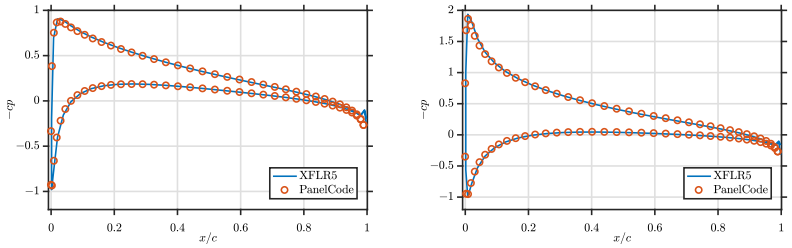

Figure 3.17: Comparison of pressure distribution, $\alpha = 3°$ (left) and $\alpha = 6°$ (right).

3.2.4.2 Delta Wing

As the second example a delta wing (Fig. 3.18) with a more complicated geometry compared with the rectangular wing is studied. The cross section of the wing is again the NACA0012 airfoil. Its geometrical properties are summarized in table 3.1.

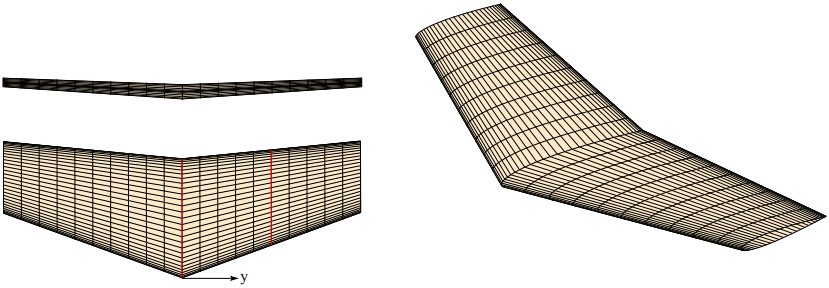

Figure 3.18: Isometric, top and front view of the delta wing.

Comparison of the lift and drag coefficients are made in Fig. 3.19. The verification of pressure coefficient distribution is made for two different angles of attack and at two different spanwise positions which are marked by red lines in Fig. 3.18 ($\frac{2y}{b} = 0$ and $\frac{2y}{b} = 0.5$, where b is the span of the wing). Also for this example, the compared quantities are in good agreement with XFLR5 results.

Table 3.1: Geometric properties of the delta wing

span	$6\,m$
root chord	$2\,m$
taper ratio	0.6
sweep angle	$20°$
dihedral angle	$3°$

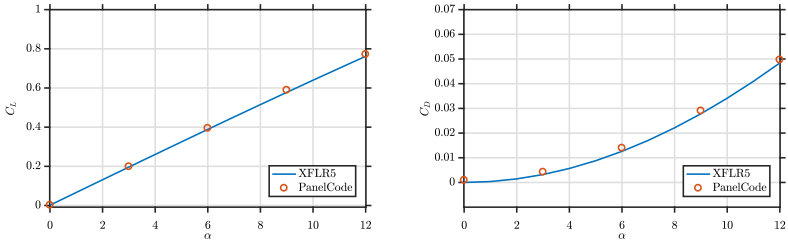

Figure 3.19: Comparison of the lift and drag coefficient for the delta wing.

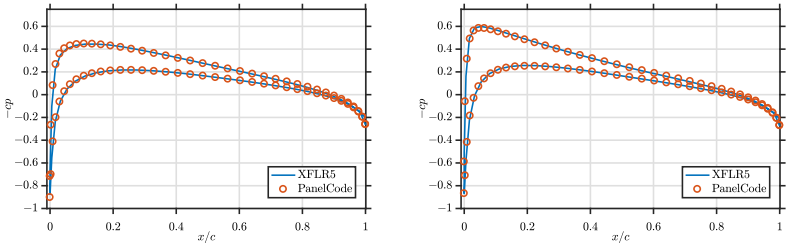

Figure 3.20: Pressure coefficient comparison at $\frac{y}{b} = 0$ (left) and $\frac{y}{b} = 0.5$ (right) for $\alpha = 2°$.

3.3 Unsteady Panel Method

So far the steady state implementation of the panel method has been explained. The unsteady implementation is based on the steady state code, however some modifications are necessary for the unsteady version. The three most important ones are: kinematic description of wing's motion, unsteady Bernoulli equation and wake roll-up:

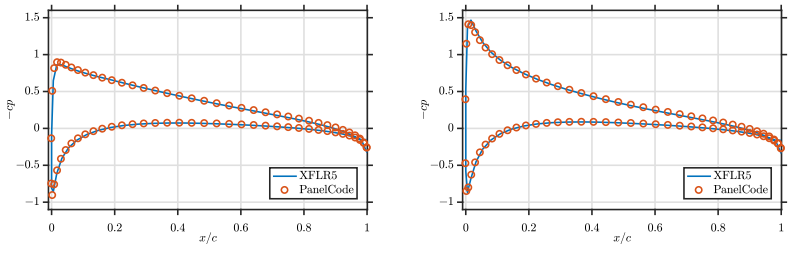

Figure 3.21: Pressure coefficient comparison at $\frac{y}{b} = 0$ (left) and $\frac{y}{b} = 0.5$ (right) for $\alpha = 6°$.

3.3.1 Kinematics

In case of a moving wing (translation or rotation) or a stationary wing with vibrating surface, as in the case of the membrane wing, deflection of the wing influences the zero normal flow boundary condition. Kinematic description of the wing's motion is necessary for enforcing the zero normal flow boundary condition for a moving wing. Consider the coordinate system xyz attached to the wing and the inertial reference frame XYZ as in Fig. 3.22. Velocity of the wing undergoing translation and rotation for an observer in the inertial reference frame is:

$$\mathbf{u}(\mathbf{r}) = \mathbf{U}_0 + \mathbf{\Omega} \times \mathbf{r} \tag{3.30}$$

where $\mathbf{U}_0$ is the velocity of translation and $\mathbf{\Omega}$ is the rotation rate:

$$\mathbf{\Omega} = (p, q, r) \tag{3.31}$$

with p, q and r being respectively rotation rate about x, y and z axis. If there is also motion relative to the body attached coordinate system like deflection of a flap or deformation of the flexible wing surface for the membrane wing, the relative velocity ($\mathbf{u}_{rel}$) should also be added to the total velocity of the wing:

$$\mathbf{u}(\mathbf{r}) = \mathbf{U}_0 + \mathbf{u}_{rel} + \mathbf{\Omega} \times \mathbf{r}. \tag{3.32}$$

Taking the wing motion into account the zero normal flow boundary condition for unsteady flow reads:

$$(\nabla\Phi - \mathbf{U}_0 - \mathbf{u}_{rel} - \mathbf{\Omega} \times \mathbf{r}) \cdot \mathbf{n} = 0. \tag{3.33}$$

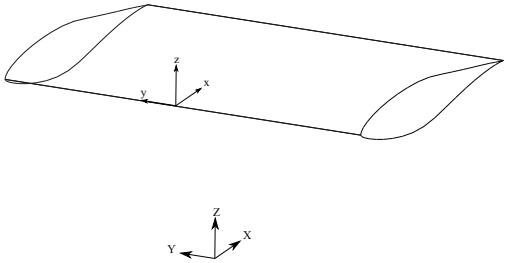

Figure 3.22: Body attached frame (xyz) and inertial reference frame (XYZ).

3.3.2 Unsteady Bernoulli equation

Without change of the elevation level between the reference point and the point of interest (where pressure should be calculated for, in this case the collocation points) the steady state Bernoulli equation is:

$$p_{ref} + \rho \frac{\|\mathbf{u}_{ref}\|^2}{2} = p + \rho \frac{\|\mathbf{u}\|^2}{2}. \tag{3.34}$$

For the case of unsteady flow there is an additional term in the equation due to change of the potential with time. The unsteady Bernoulli equation reads:

$$p_{ref} + \rho \frac{\|\mathbf{u}_{ref}\|^2}{2} = p + \rho \frac{\|\mathbf{u}\|^2}{2} + \frac{\partial \Phi}{\partial t}. \tag{3.35}$$

Taking the undisturbed flow as the reference point, the unsteady panel method solver calculates the pressure coefficient from Eqn. 3.35:

$$c_p = \frac{p - p_\infty}{\frac{1}{2}\rho \|\mathbf{u}_\infty\|^2} = 1 - \frac{\|\mathbf{u}\|^2}{\|\mathbf{u}_\infty\|^2} - \frac{2}{\|\mathbf{u}_\infty\|^2} \frac{\partial \Phi}{\partial t} \tag{3.36}$$

3.3.3 Wake roll-up

The unsteady panel method follows a time marching approach. At each time step, wake panels are shed from the trailing edge of the wing (Fig. 3.23) and are convected by the flow. The velocity at the vertices of each wake panel is calculated using the same routine, used to calculate velocity at the collocation points. Knowing the velocity and the time step size, displacement of the vertices is calculated and the position of the vertices is updated accordingly. The

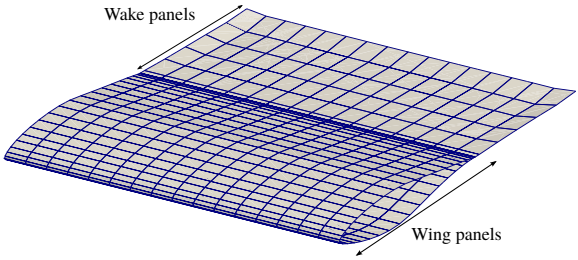

Figure 3.23: Shedding of wake panels from the trailing edge.

algorithm of the unsteady vortex panel method is presented in Algorithm 3.

Discretize the wing into panels;
for *each time step* **do**
    Calculate the influence coefficient matrices ($\mathbf{C}$, $\mathbf{W}$ and $\mathbf{B}$);
    Calculate the instantaneous RHS vector;
    Solve the linear system;
    Calculate the velocity and pressure distribution;
    Wake rollup;
end

Algorithm 3: The unsteady panel method algorithm.

3.3.4 Results

The unsteady implementation of the panel method is tested for solving three transient cases:

3.3.4.1 Sudden acceleration of a rectangular wing

This example deals with flow around a rectangular wing ($AR = 4$) initially at rest at $t = 0\,s$ which is set into movement at the velocity of $10\,m/s$ and with an angle of attack of $5°$. The wing is discretized into 80 panels in the chordwise direction and 40 panels in the spanwise direction. Time step length is $0.01\,s$. Fig. 3.24 shows the change in lift coefficient over time. Since the wing's velocity is not a function of time the lift coefficient converges to the steady

state solution. The change in the pressure distribution over wing's surface for the mid-span section is shown in Fig. 3.25. At the beginning of the simulation wake panels are shed at the trailing edge which are convected downstream. The pressure near the trailing edge during the initial time steps is highly influenced by the wake panels which are shed with relatively high circulations. As these initially shed panels are convected downstream and new panels with smaller circulation are shed, the pressure at the pressure side progressively increases and consequently increases the lift. The course of lift coefficient over time could be seen in Fig. 3.24 after about 0.5 seconds the lift coefficient reaches its steady state value. Fig. 3.25 show the convergence of pressure distribution at the mid-span section of the wing over time. Development of the wake panels in the downstream region of the flow and the tip vortices could be seen in figure 3.26. The cross section of the wake panels is shown at 4 different section, which are respectively 4, 8, 12 and 16 meters away from the trailing edge. In order to precisely capture the structure of the tip vortices, mesh refinement in the spanwise direction near the wingtips is necessary. The refinement is realized by sine discretization in both chordwise and spanwise directions.

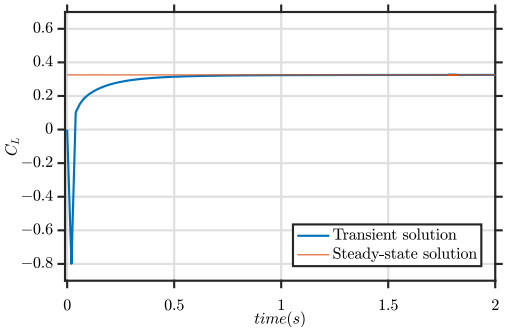

Figure 3.24: Convergence of transient solution to steady state solution from [37] over time.

3.3.4.2 Pitching oscillation of a rectangular wing

This example deals with the same wing geometry as in the previous example. The very same discretization in space and time are being used as well. But rather than translation, the wing undergoes pitch oscillations about its quarter-chord. The change of the pitch angle (in degrees) in time is governed by:

$$\theta_p = 5sin(\frac{2\pi}{T}t) \tag{3.37}$$

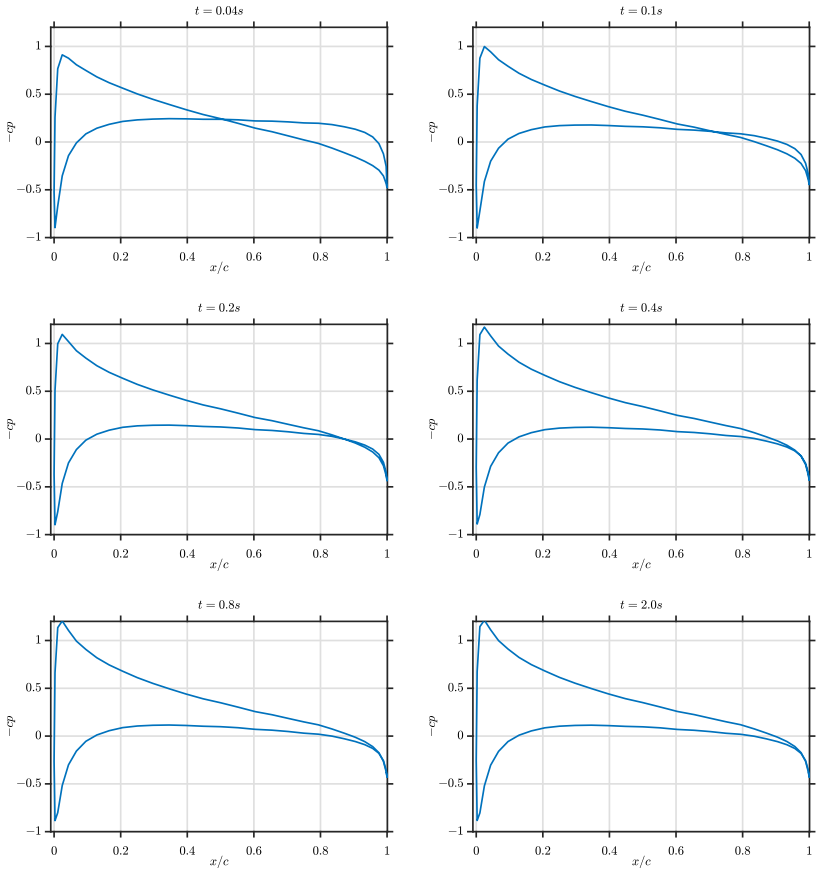

Figure 3.25: Convergence of the pressure distribution in the mid-section of the wing over time.

where T is time period of the oscillations. The development of vortices in the wake of the wing is shown in Fig. 3.27. The figure presents a slice of wake panels made at the mid-span section of the wing.

The influence of the time period of the oscillations on the lift coefficient could be seen in Fig. 3.28. Four different time periods are studied. The maximum angle of attack occurring during pitch oscillations is $5.0°$. The steady-state lift coefficient for $\alpha = \pm 5°$ is demonstrated in Fig. 3.28 by horizontal lines. As the period of the pitching oscillations increases the wing passes the point where

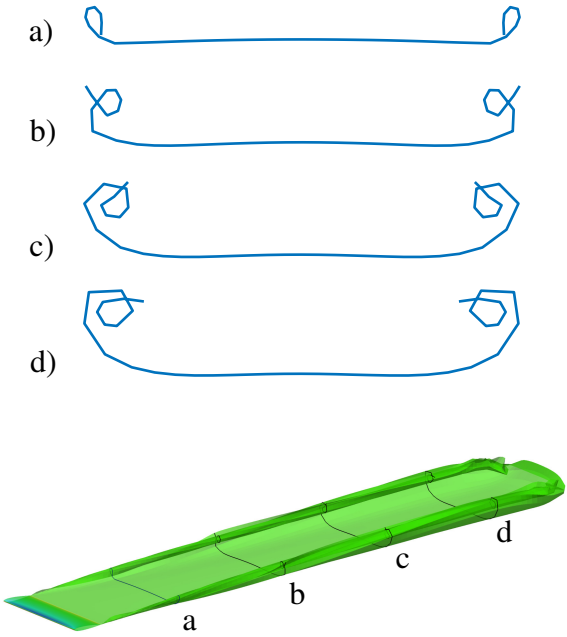

Figure 3.26: Developement of wake panels in the downstream of the flow.

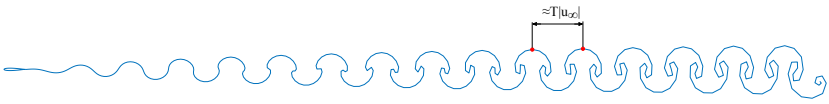

Figure 3.27: Development of vortices in the wake of an oscillating wing.

the angle of attack becomes $\pm 5^\circ$ more slowly and consequently the maximum lift coefficient becomes closer to the steady-state solution at $\alpha = \pm 5^\circ$.

3.3.4.3 NREL Phase VI turbine

Panel method could be used as a "medium fidelity" approach to bridge the gap between BEM and computationally expensive CFD simulations. Analysis of the NASA-Ames Phase VI wind turbine using the unsteady panel method is presented in this section. General information about the turbine is available in Appendix B. Fig. 3.29 shows the total thrust force applied on each blade over

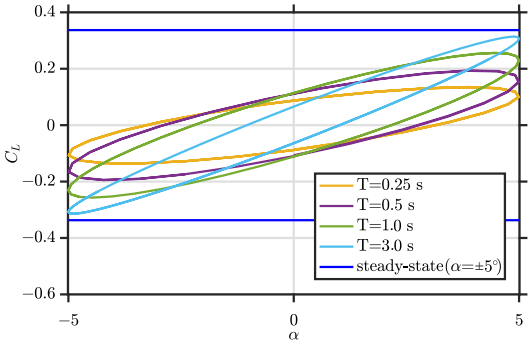

Figure 3.28: Change of the lift coefficient during pitching oscillations for different periods of the oscillations.

time. Wind shear is taken into account using logarithmic velocity profile (Eqn. 2.105) for a roughness length of $z_0 = 0.01\,m$. The Period of the oscillations is 0.84 seconds, which correspond to rotor's rotational velocity of 72 RPM.

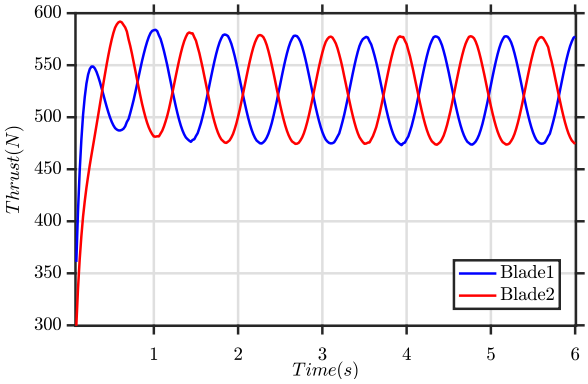

Figure 3.29: Total thrust applied to individual blades ($U_{Hub} = 8\,m/s$, $\theta_p = 5°$).

Comparison between the thrust force obtained from panel method and the unsteady BEM method is made in Fig. 3.30. It can be seen that, the panel method over-predicts the thrust force. For the wind velocity of $6\,m/s$ it over-predicts the thrust force by about $4\,\%$ compared with BEM. This overprediction increases with the increase in wind speed upto $12\,\%$. The same trend is also re-

ported in [38]. The reason for the over-prediction is the fact that panel method neglects the viscous effects and consequently the lift force increases linearly with angle of attack (Fig. 3.9). Overprediction of the lift force leads to higher thrust force computed by the panel method. On the other hand, in the absence of pitch control mechanism for the blade, the local angle of attack increases with increase in wind speed (Fig. 2.16). This causes larger over-estimation of the lift force by the panel method and, as a consequence, larger difference between panel method results and BEM result with the increase of wind speed.

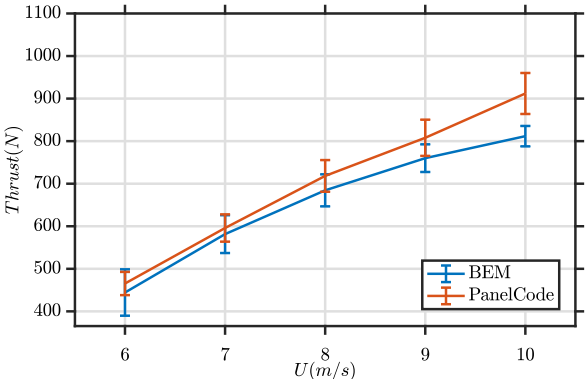

Figure 3.30: Mean thrust force applied on a single blade obtained from panel method and unsteady BEM ($\theta_p = 5°$).

The difference in the calculated thrust force can be understood better by examining the pressure distribution obtained form the panel method. The comparison between panel method's results and experimental as well as CFD results [39] is made in Figs. 3.31 and 3.32. The pitch angle is $\theta_p = 3°$ for both cases and wind shear is not taken into account. In general, there is a very good agreement between panel code results and the experimental and CFD results. Two observation could be made from the figures: First of all, for both wind speeds, panel code results match better with the reference results as we move towards the tip of the blade. Furthermore, the agreement between the results is better of the case with lower wind speed (higher tip speed ratio). Both observation could be attributed to the increase of local angle of attack as wind speed increases (for stall-control wind turbines) or as we move toward the root of the blade. The presented results are obtained from discretization of each blade into 100 panels in the chordwise direction and 30 panels in the spanwise. A time step size of $\Delta t = 0.01\ s$ is used. With this setup, using a normal PC (3.4 GHz, 8 M Cache, 15 GB RAM) the serial panel code simulates 6 seconds in a time

frame which is in order of hours, while CFD computations (depending on the degree of refinement and available computational resources) take days if not weeks.

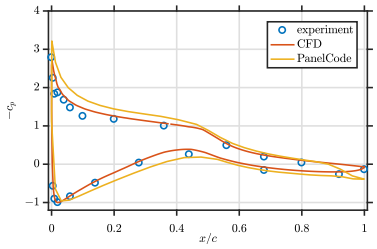

(a) $r/R = 0.3$

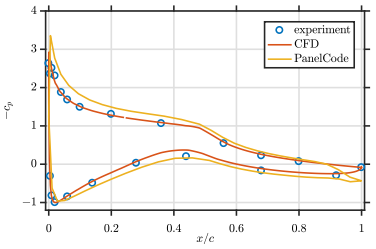

(b) $r/R = 0.47$

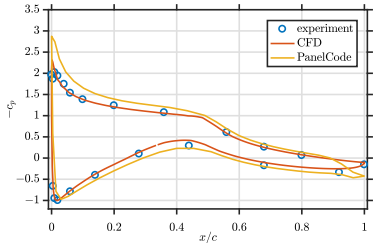

(c) $r/R = 0.63$

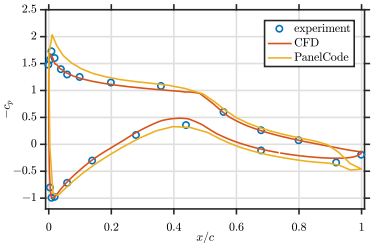

(d) $r/R = 0.8$

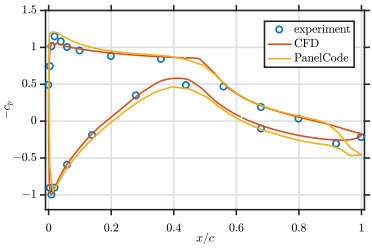

(e) $r/R = 0.95$

Figure 3.31: Pressure distribution at different blade sections for $U = 7\,m/s$.

The structure of the wake panels as they are shed from the trailing edge and convected downstream of the flow is presented in Fig. 3.33. Using cosine discretization at the tip of the blade, the method is also able to capture tip vortices (Fig. 3.34).

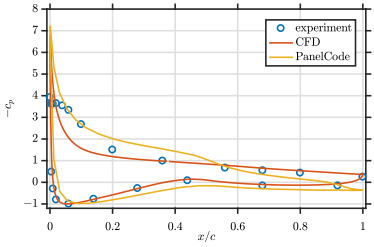

(a) $r/R = 0.3$

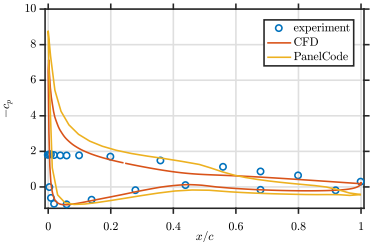

(b) $r/R = 0.47$

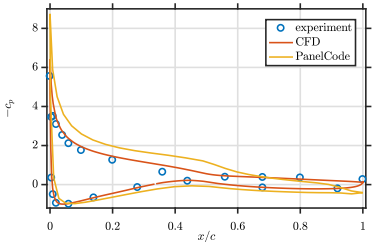

(c) $r/R = 0.63$

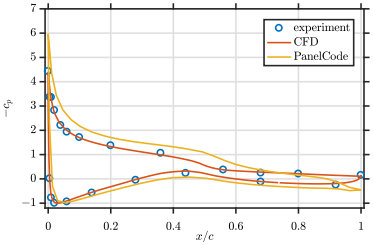

(d) $r/R = 0.8$

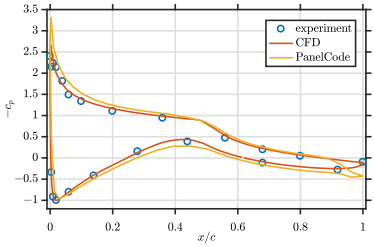

(e) $r/R = 0.95$

Figure 3.32: Pressure distribution at different blade sections for $U = 10\,m/s$.

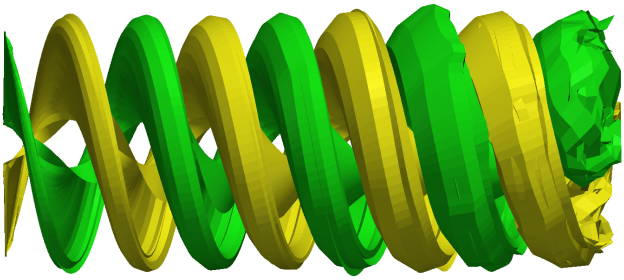

Figure 3.33: Wake panels shed at the trailing edge of the two blades.

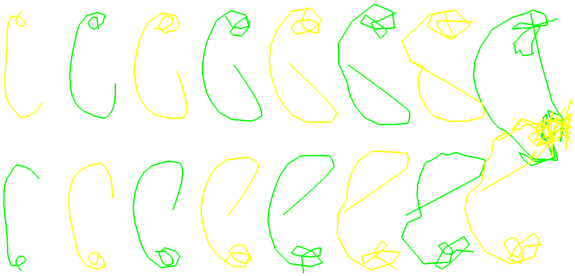

Figure 3.34: Wake panels shed at the trailing edge of the two blades.

4 *Fluid Dynamics*

In this chapter, the fundamental equations of fluid mechanics and computational fluid dynamics (CFD) are presented briefly together with a very basic introduction to the numerical solution of the Navier-Stokes equation using the finite volume method. The chapter concludes with an overview of turbulence modeling and details of the two models which are used in the simulations presented in the coming chapters. More details about the presented content could be found in fluid mechanics textbooks like the books by Fox [40] or White [41].

4.1 The governing equations

The governing equations of fluid flow are the mathematical expressions of the conservation laws in physics. They are: conservation of mass, momentum and energy.

4.1.1 Mass conservation

Conservation of mass states that the total mass of the studied fluid system is conserved, i.e. the rate of increase or decrease of mass in the system is equal to the net rate of mass flow into or out of the system. Taking the fluid element with the dimensions δx, δy and δz (shown in Fig. 4.1) into account, the change of mass within the element is:

$$\frac{\partial}{\partial t}(\rho \delta x \delta y \delta z) \tag{4.1}$$

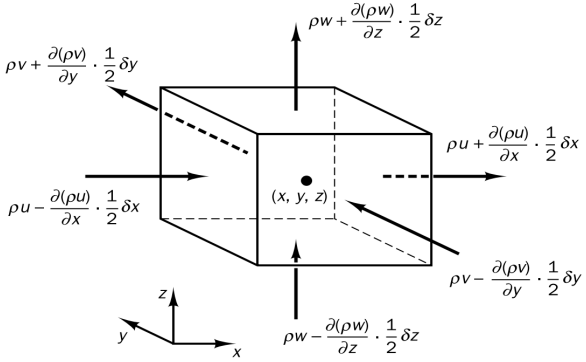

Figure 4.1: Mass flows through the surfaces of a generic fluid element, from [42].

and with $\mathbf{u} = (u, v, w)$ designating the velocity vector at the center of the element, the net mass flow through element faces normal to the x axis is:

$$(\rho u - \frac{1}{2}\frac{\partial(\rho u)}{\partial x}\delta x)\delta y\,\delta z - (\rho u + \frac{1}{2}\frac{\partial(\rho u)}{\partial x}\delta x)\delta y\,\delta z. \tag{4.2}$$

Similarly the net mass flow in the y and z direction could also be calculated. Setting the net change of mass in the fluid element equal to the net mass flow through the element's faces yields the conservation of mass (continuity) equation:

$$\frac{\partial \rho}{\partial t} + \frac{\partial(\rho u)}{\partial x} + \frac{\partial(\rho v)}{\partial y} + \frac{\partial(\rho w)}{\partial z} = 0 \tag{4.3}$$

for steady, incompressible flows the continuity equation is further simplified to:

$$\frac{\partial u}{\partial x} + \frac{\partial v}{\partial y} + \frac{\partial w}{\partial z} = 0 \tag{4.4}$$

.

4.1.2 Momentum conservation

Conservation of the linear momentum is simply Newton's second law of motion applied to a fluid element. It states that the rate of increase of the momentum for the fluid element is equal to the sum of forces acting on it. The forces acting on a fluid element can be categorized into body forces, like the gravitational force or electromagnetic force and surface forces, like the pressure and

viscous forces. In the sequel a more detailed look is taken at the conservation of linear momentum in x direction.

The rate of change of momentum per unit volume in x direction is:

$$\frac{D\,(\rho u(t,x,y,z))}{D\,t} = \frac{\partial(\rho u)}{\partial t} + u\frac{\partial(\rho u)}{\partial x} + v\frac{\partial(\rho u)}{\partial y} + w\frac{\partial(\rho u)}{\partial z} \tag{4.5}$$

which is called the material or total derivative. In vector notation it reads:

$$\frac{D\,(\rho u(t,x,y,z))}{D\,t} = \frac{\partial(\rho u)}{\partial t} + div(\rho\, u\, \mathbf{u}). \tag{4.6}$$

Surface forces acting on a generic fluid element are shown in Fig. 4.2.

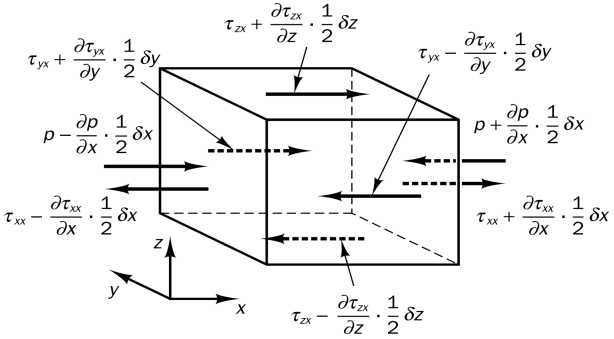

Figure 4.2: Pressure and shear forces acting on a generic fluid element, from [42].

The sum of surface forces acting on the element in the x direction is:

$$\Big[(-\frac{\partial p}{\partial x} + \frac{\partial \tau_{xx}}{\partial x}) + \frac{\partial \tau_{yx}}{\partial y} + \frac{\partial \tau_{zx}}{\partial z}\Big]\delta x\delta y\delta z \tag{4.7}$$

where the first term in the bracket is the sum of forces acting on the left and right faces. The second term corresponds to the forces acting on the front and back sides and finally the third term corresponds to the force resultant acting on the top and bottom faces of the element. The shear components for Newtonian fluids in incompressible flow is:

$$\tau_{xx} = \mu(\frac{\partial u}{\partial x} + \frac{\partial u}{\partial x}), \quad \tau_{yx} = \mu(\frac{\partial v}{\partial x} + \frac{\partial u}{\partial y}), \quad \tau_{zx} = \mu(\frac{\partial w}{\partial x} + \frac{\partial u}{\partial z}) \tag{4.8}$$

Inserting the shear components form Eqn. 4.8 into Eqn. 4.7 and setting the sum of the forces equal to the rate of change of momentum in x direction (Eqn. 4.6) yields the equation for the conservation of linear momentum in the x direction:

$$\rho\frac{Du}{Dt} = -\frac{\partial p}{\partial x} + \mu\Big(\frac{\partial^2 u}{\partial x^2} + \frac{\partial^2 v}{\partial y^2} + \frac{\partial^2 w}{\partial z^2}\Big) + \rho g_x \tag{4.9}$$

g_x is the gravitational acceleration in the x direction. Conservation of momentum in y and z direction could be derived similarly. Together they are called Navier-Stokes equations. The Navier-Stokes equations in vector notation for incompressible flow read:

$$\begin{aligned}
\frac{\partial u}{\partial t} + div(u\,\mathbf{u}) &= -\frac{1}{\rho}\frac{\partial p}{\partial x} + div\big(\nu\ grad(u)\big) + g_x \\
\frac{\partial v}{\partial t} + div(v\,\mathbf{u}) &= -\frac{1}{\rho}\frac{\partial p}{\partial y} + div\big(\nu\ grad(v)\big) + g_y \\
\frac{\partial w}{\partial t} + div(w\,\mathbf{u}) &= -\frac{1}{\rho}\frac{\partial p}{\partial z} + div\big(\nu\ grad(w)\big) + g_z
\end{aligned} \tag{4.10}$$

The Navier-Stokes equations alongside with the continuity equation are the fundamental governing equations of fluid flow. In a CFD code the discretized form of these equations (either using the finite volume or finite element method) is solved via numerical techniques which are discussed in the next sections.

4.2 Numerical solution of the Navier-Stokes equations

The CFD results presented in this work are obtained using the open-source CFD software, OpenFOAM, which is a finite volume based fluid solver. In the finite volume method, the integral form of the governing equations is used. After discretizing the fluid domain into a number of elements (finite volumes) the integral form of the equations is used to enforce conservation of mass and momentum for each element. The discretization process can be divided into two parts:

1. **Domain discretization:** discretizing the computational domain into non-overlapping elements. The outcome of this step is the computational mesh for solving the fluid flow problem.

2. **Equation discretization:** deriving the algebraic equivalent of the governing equations which are originally in form of partial differential equations. The outcome of this step is a system of algebraic equations which presents the conservation laws applied to each element in the mesh.

In the following, discretization of the momentum equation in the x direction is discussed in more detail. Discretization starts from the integral form of the conservation of linear momentum in x direction (Eqn. 4.10) which reads:

$$\int_{CV} \frac{\partial u}{\partial t} dV + \int_{CV} div(u\mathbf{u}) dV = \int_{CV} -\frac{1}{\rho}\frac{\partial p}{\partial x} dV + \int_{CV} div\big(\nu\ grad(u)\big) dV + \int_{CV} g_x dV. \tag{4.11}$$

The volume integrals for the convective and diffusion terms are then converted to surface integrals using the convergence theorem. The convergence theorem states:

$$\int_{CV} div(\mathbf{u})\, dV = \int_{A} \mathbf{n} \cdot \mathbf{u}\, dA \tag{4.12}$$

the integration is then done over all surfaces of the element. $\mathbf{n}$ is the normal vector of the element faces. Applying the convergence theorem to Eqn. 4.11 yields:

$$\frac{\partial}{\partial t}\Big(\int_{CV} u\, dV\Big) + \int_{A} \mathbf{n} \cdot u\mathbf{u}\, dA = \int_{CV} -\frac{1}{\rho}\frac{\partial p}{\partial x} dV + \int_{A} \mathbf{n} \cdot (\nu\ grad(u)) dA + \int_{CV} g_x dV. \tag{4.13}$$

The first term on the left hand side of the equation is the rate of change of the momentum in the x direction within the control volume and the second term shows momentum flux through element faces. The terms on the right hand side correspond respectively to the pressure, viscous and gravitational force acting on the control volume.

The volume integrals are calculated using Gauss quadrature. In a staggered grid velocities are stored at the face centers which makes the calculation of the flux over element faces easier. Calculating the diffusion term involves estimation of the velocity gradient at the face center. Different interpolation techniques could be used for this purpose. More details on implementation of the finite volume method and the methods for estimation of the involved terms in the discretized equation could be found in [43].

Two different approaches could be used for solving the Navier-Stokes equation:

- **Simultaneous approach:** In the simultaneous approach the system of equations is solved simultaneously for all the unknowns. It is robuster than the staggered (iterative) approach, but demands more memory and computational power [44].

- **Staggered approach:** In the staggered approach the equations are solved sequentially. The coupling between the pressure and velocity field is enforced iteratively. The solver assumes an initial pressure distribution to solve the velocity field. The assumed pressure is then corrected by the obtained solution of the velocity field. The procedure is iterated until convergence is reached. This approach is also called pressure correction method, since the assumed pressure is corrected during the iterations. OpenFOAM uses the staggered approach for solving the fluid problem. Common algorithms using the staggered approach include the SIMPLE (Semi-Implicit Method for Pressure-Linked Equations) algorithm by Patankar and Spalding [45] or the PISO (Pressure Implicit with Splitting of Operators) algorithm [46].

4.3 Turbulence modeling

Fluid flow can be categorized into two regimes: laminar and turbulent flows. Laminar flow, or streamline flow, is the type of flow where fluid particles move in parallel layers with no disruption between the layers [47], while in the case of turbulent flow the streamlines do not have any layered pattern and chaotic changes occur in the pressure and velocity field.

Random, three-dimensional fluctuations exist in all the three components of the velocity vector in turbulent flow. The velocity vector for turbulent flow can be decomposed into a mean component and a fluctuating component:

$$\mathbf{u} = \mathbf{U} + \mathbf{u}'. \tag{4.14}$$

The fluctuating part of the velocity vector ($\mathbf{u}'$) is completely irregular or in other words, random. Because of the randomness of velocity fluctuations it is impossible to use a deterministic approach for modeling of turbulent flows, statistical methods are used to describe turbulent flows instead [47]. Diffusivity is generally very high in turbulent flows which increases the rate of momentum exchange between adjacent fluid particles. One other characteristic of turbulent flows is their large Reynolds number. The Reynolds number describes the ratio

of inertial forces to viscous forces and is defined as:

$$Re = \frac{uL}{\mu}, \tag{4.15}$$

where μ is the kinematic viscosity and L is a characteristic length. For pipe flows the diameter of the pipe is used as the characteristic length, while for flow over airfoils the chord length is used to calculate the Reynolds number. The large Reynolds number in the case of turbulent flow means that inertia forces dominate viscous forces, while laminar flows are characterized by higher diffusion of momentum due to viscous effects.

Eddies of different length scales are present in turbulent flows. Based on eddy's size, they are categorized into the energy-containing range, the inertial subrange and the dissipation range. They are illustrated in Fig. 4.3. The Kolmogorov length scale and the length scale of the largest existing eddies is designated respectively by the η and L_0. L_{DI} is the demarcation length scale between dissipation range and inertial subrange, while L_{EI} is used for the demarcation length scale between inertial subrange and the energy-containing rage and L designates the characteristic length of the flow.

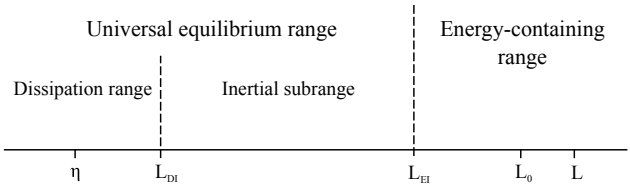

Figure 4.3: Existing lengthscales and ranges in turbulent flow, from [48].

The characteristics of the existing eddies in turbulent flows are described using the following three hypotheses (taken directly from [48]):

- **Kolmogorovs hypothesis of local isotropy.** At sufficiently high Reynolds number, the small-scale turbulent motions ($l << L_0$) are statistically isotropic.

- **Kolmogorovs first similarity hypothesis.** In every turbulent flow at sufficiently high Reynolds number, the statistics of the small-scale motions ($l < L_{EI}$) have a universal form that is uniquely determined by ν and ϵ. (ν is the kinematic viscosity of the fluid and ϵ is the rate of dissipation of turbulent kinetic energy.)

- **Kolmogorovs second similarity hypothesis.** In every turbulent flow at sufficiently high Reynolds number, the statistics of the motions of scale l in the range ($\eta << l << L_0$) have a universal form that is uniquely determined by ϵ, independent of ν.

More detailed explanation of the three Kolmogrov hypotheses and the Kolmogorov's velocity, time and length scales could be found in [48].

The ratio of the smallest eddies to the largest eddies available in turbulent flow decreases with increase of the Reynolds number:

$$\frac{\eta}{L_0} \approx Re^{-\frac{3}{4}}. \tag{4.16}$$

For the exact solution of the flow problem involving turbulence, even the smallest existing eddies should be resolved. It requires a very fine spatial discetization, specially for high Reynolds numbers. Time discretizations also needs to be small enough to resolve the life time of the very small eddies. Based on the complexity level of modeling the existing eddies in a turbulent flow, the methods of turbulent flow calculation are grouped into the following three categories:

- **Direct Numerical Simulation (DNS):** DNS is about computing all available scales of the motion in the flow, from the largest scales to the smallest turbulent velocity fluctuations. In DNS, instantaneous continuity and Navier-Stokes equations are solved on a grid which is fine enough to resolve the Kolmogorov scales where energy is dissipated in form of heat and using a time step small enough to resolve the very fast turbulence fluctuations of the small eddies. DNS is computationally a very expensive approach and,as a result, is not common practice for industrial flow computation [42].

- **Large Eddy Simulation (LES):** In LES, the larger turbulent motions are directly computed, while the influence of the smaller eddies is not directly computed, but modeled. It involves a filtering operation to separate larger and smaller eddies. A cutoff length is chosen in LES with the goal of resolving only eddies larger than the selected cutoff length. The interaction between the smaller eddies, which are not resolved, and the computed eddies is modeled using a so-called sub-grid-scale stress (SGS) models. LES solves the filtered equations together with a SGS model for the unresolved eddies.

- **Reynolds-Averaged Navier-Stokes equations (RANS):** Rather than solving the flow equations for the instantaneous values, in RANS the focus is on the mean flow and how it is affected by turbulence. Time-averaged Navies-Stokes equations are solved in RANS. New terms do appear in the time-averaged equations, which are called Reynolds stresses. These extra terms should be modeled via turbulence models. Spalart-Allmaras and $k-\omega$ SST are two of the models used in RANS, which are used in the simulations presented in sections 6.1.3, 7.2.1, 7.2.2 and 7.4. They are explained in more detail in the upcoming sections.

4.3.1 Spalart-Allmaras

The model is proposed by Spalart and Allmaras [49] and is mainly developed for aerodynamic applications. It has proved to provide reliable results for aerodynamic flows [50], but because of some limitations, the model can not serve as a general purpose turbulence model. It is for example unable to correctly model the decay of eddy viscosity in isotropic turbulence [48].

The Spalart-Allmaras model uses a single equation for the transport of kinematic eddy viscosity parameter ($\tilde{\nu}$). The dynamic eddy viscosity is then calculated from $\tilde{\nu}$:

$$\mu_t = \rho\tilde{\nu}f_{v1} \tag{4.17}$$

where f_{v1} is the wall-damping functions. For high Reynolds numbers, f_{v1} tend to unity and the kinematic eddy viscosity (ν_t) is becomes equal to the eddy viscosity parameter ($\tilde{\nu}$). The transport equation for $\tilde{\nu}$ is:

$$\frac{\partial\rho\tilde{\nu}}{\partial t}+div(\rho\tilde{\nu}\mathbf{U}) = \frac{1}{\sigma_v}div\Big[(\mu+\rho\tilde{\nu})grad(\tilde{\nu})+C_{b2}\,\rho\frac{\partial\tilde{\nu}}{\partial x_k}\frac{\partial\tilde{\nu}}{\partial x_k}\Big]+C_{b1}\rho\tilde{\nu}\tilde{\Omega}-C_{w1}\rho\Big(\frac{\tilde{\nu}}{\kappa y}\Big)^2 f_w \tag{4.18}$$

where $\tilde{\Omega}$ is a combination of the mean vorticity (Ω) and $\tilde{\nu}$:

$$\tilde{\Omega} = \Omega + \frac{\tilde{\nu}}{(\kappa y)^2}f_{v2}. \tag{4.19}$$

In the above equations y is the distance to the solid wall, f_w and f_{v2} are wall-damping functions and κ, σ_v, C_{b1} and C_{b2} are model constants whose value could be found in [42]. The boundary conditions for $\tilde{\nu}$ are:

$$\tilde{\nu}_{wall} = 0 \tag{4.20}$$

and

$$\tilde{\nu}_{farfield} = 3\nu_\infty \;\; to \;\; 5\nu_\infty. \tag{4.21}$$

4.3.2 $\mathbf{k-\omega}$ SST

The $k-\omega\ SST$ model is a two-equation turbulence model which solves one equation for the turbulent kinetic energy (k) and one for the specific dissipation rate (ω). It was proposed in 1992 by Menter [51] with the goal of having the advantages of both the $k-\epsilon$ model and the $k-\omega$ model. The $k-\omega\ SST$ model uses the $k-\omega$ model for near wall regions and the $k-\epsilon$ model for regions away from the wall. Switching between the two models is realized via blending functions. The blending functions are chosen in a way that:

1. They are zero at the wall.
2. They tend to unity towards the far field.
3. They provide a smooth transition at the distance half way between the wall and the far field boundary [42].

The transport equation for k and ω at high Reynolds number flows read:

$$\frac{\partial \rho k}{\partial t} + div(\rho k \mathbf{U}) = div\Big[(\mu + \frac{\mu_t}{\sigma_k})grad(k)\Big] + P_k - \beta^* \rho k \omega \tag{4.22}$$

where P_k is the rate of production of turbulent kinetic energy, and

$$\frac{\partial \rho \omega}{\partial t} + div(\rho \omega \mathbf{U}) = div\Big[(\mu + \frac{\mu_t}{\sigma_{\omega,1}})grad(\omega)\Big] + \gamma_2\Big[2\rho S_{ij}\cdot S_{ij} - \frac{2}{3}\rho\omega\frac{\partial U_i}{\partial x_j}\delta_{ij}\Big] - \beta_2\rho\omega^2 + 2\frac{\rho}{\omega\sigma_{\omega,2}}\frac{\partial k}{\partial x_k}\frac{\partial \omega}{\partial x_k}. \tag{4.23}$$

σ_k, $\sigma_{\omega,1}$, $\sigma_{\omega,2}$, γ_2, β_1, β_2 and β^* are all model constants. The boundary conditions for k and ω are [52]:

$$k_{farfield} = \frac{10^{-5}U_\infty^2}{Re_L}\ \ to\ \ \frac{0.1U_\infty^2}{Re_L}, \tag{4.24}$$

$$k_{wall} = 0, \tag{4.25}$$

$$\omega_{farfield} = \frac{U_\infty}{L}\ \ to\ \ 10\frac{U_\infty}{L}, \tag{4.26}$$

and

$$\omega_{wall} = 10\frac{6\nu}{\beta_1(\Delta d_1)^2}. \tag{4.27}$$

where Δd_1 is the height of the first cell layer.

5 *Structural Mechanics*

The topic of this chapter is structural analysis of membrane structures and Fluid-Structure Interaction (FSI). Analysis of membrane structures is done in two steps. First, the equilibrium shape of the membrane, given the pre-stress and support condition, needs to be calculated. This step is taken care of in form finding analysis. Form finding analysis is followed by static or dynamic analysis of the structure, where the response of the structure to the applied external loading is analyzed.

The chapter starts with the theory behind form finding analysis of membrane structures, followed by finite element formulation of the membrane element. Finally, an overview of the general approach in FSI analysis and different coupling methods is presented.

5.1 Form finding of membrane structures

Form finding analysis is inspired among others by the pioneering work of the late German architect Frei Otto to find the equilibrium shape of cable structures. Different approaches are available for form finding analysis ranging from dynamic relaxation [53] to force density method [54] and the updated reference strategy (URS) [55]. The goal of form finding analysis of membrane structures is to find the equilibrium shape of the membrane confined to a given boundary, given the prescribed pre-stresses in the membranes and supporting cables. The position of each point on the membrane is described by the surface coordinates θ^1 and θ^2:

$$\mathbf{x} = \mathbf{x}(\theta^1, \theta^2). \tag{5.1}$$

Derivatives of the position vector with respect to the spatial coordinates form the covariant base vectors:

$$\mathbf{g}_i = \frac{\partial \mathbf{x}}{\partial \theta^i} \qquad i = 1, 2. \tag{5.2}$$

Form finding analysis starts from a reference configuration (Fig. 5.1) where applied pre-stresses are not necessarily in equilibrium. In an iterative solution procedure, the initial configuration converges to the equilibrium shape. The

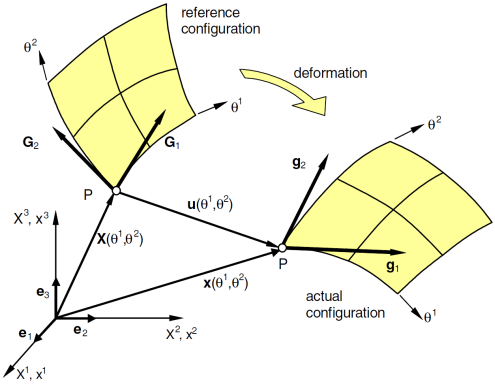

Figure 5.1: Surface description of membrane element.

displacement of each point on the membrane is:

$$\mathbf{u}(\theta^1, \theta^2) = \mathbf{x}(\theta^1, \theta^2) - \mathbf{X}(\theta^1, \theta^2) \tag{5.3}$$

where $\mathbf{X}$ is the position vector in the reference configuration. The transformation from the reference configuration to the actual configuration is done via the deformation gradient:

$$\mathbf{F} = \frac{d\mathbf{x}}{d\mathbf{X}}. \tag{5.4}$$

Using the principle of virtual work the governing equation for the equilibrium state of the membrane could be derived:

$$\delta w = t_s \int_a \sigma_s : \frac{\partial(\delta \mathbf{u})}{\partial \mathbf{x}} da = t_s \int_a \sigma_s : \delta \mathbf{u}_{,x} da = 0, \tag{5.5}$$

In the above equation, t_s is the membrane thickness. The integral is calculated over the actual area and $\delta \mathbf{u}_{,x}$ can be expressed in terms of the deformation

gradient:

$$\delta \mathbf{u}_{,x} = \frac{\partial(\delta \mathbf{u})}{\partial \mathbf{x}} = \frac{\partial(\delta \mathbf{x})}{\partial \mathbf{X}} \cdot \frac{\partial \mathbf{X}}{\partial \mathbf{x}} = \delta(\frac{\partial \mathbf{x}}{\partial \mathbf{X}}) \cdot \mathbf{F}^{-1} = \delta \mathbf{F} \cdot \mathbf{F}^{-1}. \tag{5.6}$$

Inserting Eqn. 5.6 into Eqn. 5.5 and doing some rearrangements, the equation for the virtual work reads:

$$\delta w = t_s \int_A \sigma_{\mathbf{s}} : (\delta \mathbf{F} \cdot \mathbf{F}^{-1}) det(\mathbf{F}) dA = t_s \int_A det(\mathbf{F})(\sigma_{\mathbf{s}} \cdot \mathbf{F}^{-T}) : \delta \mathbf{F} dA = 0. \tag{5.7}$$

In form finding, the discretized form of Eqn. 5.7 is solved using the finite element method. Nodal displacements of the discretized nodes are arranged in a column vector $\mathbf{b}$. Variation of the deformation gradient then reads:

$$\delta \mathbf{F} = \frac{\partial \mathbf{F}}{\partial b_r} \delta b_r \qquad r = 1, ..., ndof \tag{5.8}$$

where b_r is the r^{th} component of $\mathbf{b}$. Inserting variation of deformation gradient from Eqn. 5.8 into Eqn. 5.7 yields:

$$\delta w = \delta b_r t_s \int_A det(\mathbf{F})(\sigma_{\mathbf{s}} \cdot \mathbf{F}^{-T}) : \frac{\partial \mathbf{F}}{\partial b_r} dA = 0 \tag{5.9}$$

and finally the non-linear discretized equation is derived which holds for each degree of freedom:

$$\frac{\partial w}{\partial b_r} = t_s \int_A det(\mathbf{F})(\sigma_{\mathbf{s}} \cdot \mathbf{F}^{-T}) : \frac{\partial \mathbf{F}}{\partial b_r} dA = 0. \tag{5.10}$$

In the updated reference strategy the linearized form of Eqn. 5.10 is solved iteratively to find the equilibrium shape.

5.1.1 Membrane element

Linearization of Eqn. 5.10 for a membrane element reads:

$$LIN\Big(\frac{\partial w}{\partial b_r}\Big) = t_s \int_A det(\mathbf{F})(\sigma_{\mathbf{s}} \cdot \mathbf{F}^{-T}) : \frac{\partial \mathbf{F}}{\partial b_r} dA + \Delta b_s t_s \int_A \frac{\partial}{\partial b_s} \Big(det(\mathbf{F})(\sigma_{\mathbf{s}} \cdot \mathbf{F}^{-T}) : \frac{\partial \mathbf{F}}{\partial b_r} \Big) dA = 0. \tag{5.11}$$

Using standard finite element method notation, the equation can be written as:

$$\mathbf{R} + \mathbf{K} \boldsymbol{\Delta} \mathbf{b_s} = \mathbf{0} \tag{5.12}$$

where $\mathbf{R}$ is the out of balance force vector and $\mathbf{K}$ is the tangential stiffness matrix. The base vectors $\mathbf{g}_i$ depend linearly on the degrees of freedom b_r. Consequently, the second derivative of the deformation gradient vanishes and the components of the stiffness matrix and the out of balance force vector are simplified to:

$$K_{rs} = t_s \int_A \big(det(\mathbf{F})\sigma_s^{\alpha\beta}(\mathbf{g}_{\alpha,r}\cdot\mathbf{g}_{\beta,s}) + (det(\mathbf{F})\sigma^{\alpha\beta})_{,s}(\mathbf{g}_{\alpha,r}\cdot\mathbf{g}_{\beta})\big)dA, \quad (5.13)$$

and

$$R_r = t_s \int_A det(\mathbf{F}\sigma_s^{\alpha\beta})(\mathbf{g}_{\alpha,r}\cdot\mathbf{g}_{\beta})dA. \quad (5.14)$$

5.1.2 Cable element

In order to derive the stiffness matrix and the out of balance force for the cable element, Eqn. 5.7 is first of all reduced to one dimension.

$$\delta w = A_c \int_S det(\mathbf{F})(\sigma_{\mathbf{c}}\cdot\mathbf{F}^{-T}) : \delta\mathbf{F}dA = 0. \quad (5.15)$$

Only one base vector, $\mathbf{g}_1$, is needed for the kinematic description of cable element which is tangential to the cable. The determinant of the deformation gradient in this case reduces to $det(\mathbf{F}) = ||\mathbf{g}_1||/||\mathbf{G}_1||$. Inserting it into Eqn. 5.15, yields the equation of virtual work:

$$\delta w = A_c \int_S \frac{||\mathbf{g}_1||}{||\mathbf{G}_1||}(\sigma_c g^{11}\mathbf{g}_1\otimes\mathbf{g}_1\cdot\mathbf{g}^1\otimes\mathbf{G}_1) : \delta\mathbf{g}_1\otimes\mathbf{G}^1 dS = A_c\sigma_c \int_S \frac{||\mathbf{g}_1||}{||\mathbf{G}_1||} g^{11}(\delta\mathbf{g}_1\cdot\mathbf{g}_1)dS. \quad (5.16)$$

Discretizing the cable by 2-node elements and performing the integration, the discretized form of Eqn. 5.16 reads:

$$\delta w = \sigma_c A_c \frac{l}{L}\frac{1}{l^2}(\mathbf{g}_{1,r}\cdot\mathbf{g}_1)L\delta b_r = \frac{\sigma_c A_c}{l}(\mathbf{g}_{1,r}\cdot\mathbf{g}_1)\delta b_r \quad (5.17)$$

where L is the initial length and l is the actual length of the element. With the same procedure, as for the membrane element, the stiffness matrix and the out of balance force vector for the cable element are calculated by linearizing Eqn. 5.17:

$$K_{rs} = \frac{\sigma_c A_c}{l}\big[(\mathbf{g}_{1,r}\cdot\mathbf{g}_{1,s}) - \frac{1}{l^2}(\mathbf{g}_{1,r}\cdot\mathbf{g}_1)(\mathbf{g}_{1,s}\cdot\mathbf{g}_1)\big], \quad (5.18)$$

and

$$R_r = \frac{\sigma_c A_c}{l}(\mathbf{g}_{1,r}\cdot\mathbf{g}_1). \quad (5.19)$$

An example of form finding analysis is presented in Fig. 5.2. The reference configuration of the 4 point tent example consists of four flat membrane patches. They are connected to four edge cables at the boundaries and are fixed at four support points. After applying pre-stresses to the 4 membranes and the supporting edge cables, the structure evolves from the initially flat membranes to a double curved surface where internal membrane pre-stresses are in equilibrium with the forces from the 4 edge cables.

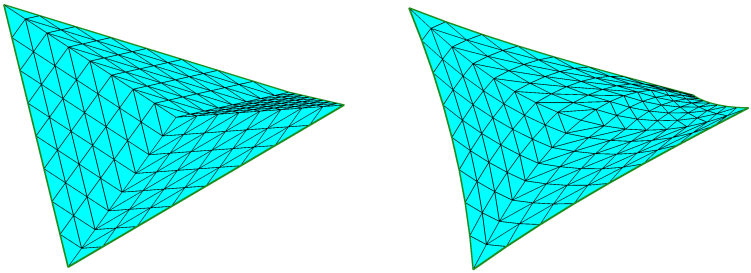

Figure 5.2: Form finding analysis of a 4 point tent. Left: initial state. Right: equilibrium state.

As mentioned before, the goal of form finding analysis is to calculate the geometry for which internal forces form membrane and edge cables are in equilibrium. It should be noted that the result of a form finding analysis depends on the topology of the structure and its support condition (position of supporting edge cables and pre-defined fixed supports), pre-stresses, membrane thickness and cable cross section. Parameters like the elastic modulus, Poisson's ratio and density are not influencing form finding results since they do not show up in calculating the forces resulting from the prescribed stress distribution.

5.2 Finite element formulation of the membrane element

For the analysis of the membrane blade, the upper and the lower surface of the blade are discretized into quadrilateral membrane elements. Finite element formulation of the quadrilateral membrane element using bilinear shape functions is presented in this section. Similar to the form finding analysis the formulation uses a reference configuration, which corresponds to the undeformed membrane, and the actual configuration of the deformed structure (Fig. 5.3).

The base vectors for the reference configuration and for the actual configuration

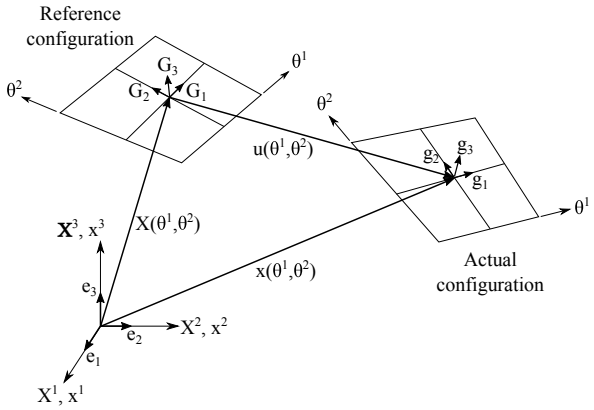

Figure 5.3: Reference and actual configuration of the membrane element.

are calculated by taking the derivative of the corresponding position vector:

$$\mathbf{G}_i = \frac{\partial \mathbf{X}(\theta^1, \theta^2)}{\partial \theta^i} \qquad i = 1, 2$$
$$\mathbf{G}_3 = \mathbf{G}_1 \times \mathbf{G}_2 \tag{5.20}$$

and

$$\mathbf{g}_i = \frac{\partial \mathbf{x}(\theta^1, \theta^2)}{\partial \theta^i} \qquad i = 1, 2$$
$$\mathbf{g}_3 = \mathbf{g}_1 \times \mathbf{g}_2. \tag{5.21}$$

Membrane's displacement is easily calculated as the difference between the position vector in the deformed configuration and in the reference configuration (Eqn. 5.3). Using the base vectors, the components of Green-Lagrange strain tensor are:

$$E_{ij} = \frac{1}{2}(\mathbf{g}_i \cdot \mathbf{g}_j - \mathbf{G}_i \cdot \mathbf{G}_j) \tag{5.22}$$

For calculation of the element stiffness matrix, the first derivative and the second derivative of the Green-Lagrange strain tensor with respect to the degrees of freedom are needed. These derivatives are:

$$\frac{\partial E_{mn}}{\partial u_i} = \frac{1}{2}\left(\frac{\partial \mathbf{g}_m}{\partial u_i} \cdot \mathbf{g}_n + \mathbf{g}_m \cdot \frac{\partial \mathbf{g}_n}{\partial u_i}\right) \tag{5.23}$$

and

$$\frac{\partial^2 E_{mn}}{\partial u_i \partial u_j} = \frac{1}{2}\Big(\frac{\partial^2 \mathbf{g}_m}{\partial u_i \partial u_j} \cdot \mathbf{g}_n + \frac{\partial \mathbf{g}_m}{\partial u_i} \cdot \frac{\partial \mathbf{g}_n}{\partial u_j} + \frac{\partial \mathbf{g}_m}{\partial u_j} \cdot \frac{\partial \mathbf{g}_n}{\partial u_i} + \mathbf{g}_m \cdot \frac{\partial^2 \mathbf{g}_n}{\partial u_i \partial u_j} \Big). \quad (5.24)$$

5.2.1 Discretization

Using the isoparametric approach, the geometry and displacement are both discretized by the same shape functions which are the bilinear shape functions in this case:

$$\begin{aligned} N_1(\theta^1, \theta^2) &= \frac{1}{4}(1-\theta^1)(1-\theta^2) \\ N_2(\theta^1, \theta^2) &= \frac{1}{4}(1+\theta^1)(1-\theta^2) \\ N_3(\theta^1, \theta^2) &= \frac{1}{4}(1+\theta^1)(1+\theta^2) \\ N_4(\theta^1, \theta^2) &= \frac{1}{4}(1-\theta^1)(1+\theta^2) \end{aligned} \quad (5.25)$$

The geometry of the deformed and undeformed membrane element, as well as the displacement field, can be described using the shape functions:

$$\begin{aligned} \mathbf{X}(\theta^1, \theta^2) &= \sum_{i=1}^{4} N_i(\theta^1, \theta^2)\mathbf{X}_i \\ \mathbf{x}(\theta^1, \theta^2) &= \sum_{i=1}^{4} N_i(\theta^1, \theta^2)\mathbf{x}_i \\ \mathbf{u}(\theta^1, \theta^2) &= \sum_{i=1}^{4} N_i(\theta^1, \theta^2)\mathbf{u}_i \end{aligned} \quad (5.26)$$

Describing the geometry of the element as a linear combination of shape functions makes the description of the base vectors and also their derivatives in terms of the shape functions possible. The base vectors can be formulated

based on the derivatives of the shape functions:

$$\begin{aligned} \mathbf{G}_i &= \sum_{i=j}^{4} \frac{\partial N_j}{\partial \theta^i} \mathbf{X}_j \quad for \;\; i = 1:3 \\ \mathbf{g}_i &= \sum_{i=j}^{4} \frac{\partial N_j}{\partial \theta^i} \mathbf{x}_j \quad for \;\; i = 1:3 \end{aligned} \tag{5.27}$$

and the derivatives of the base vectors read:

$$\begin{aligned} \frac{\partial \mathbf{g}_m}{\partial u_i} &= \sum_{k=1}^{4} \frac{\partial N_k}{\partial \theta^m} \frac{\partial \mathbf{x}_k}{\partial u_i} \\ \frac{\partial^2 \mathbf{g}_m}{\partial u_i \partial u_j} &= \sum_{k=1}^{4} \frac{\partial N_k}{\partial \theta^m} \frac{\partial^2 \mathbf{x}_k}{\partial u_i \partial u_j} \end{aligned} \tag{5.28}$$

5.2.2 Principle of virtual work

The principal of virtual work states that for a system in equilibrium the sum of the work done by internal and external forces is zero as the system undergoes a virtual displacement of $\delta \mathbf{u}$:

$$\delta W = \delta W_{int} + \delta W_{ext} = 0 \tag{5.29}$$

The internal work is:

$$\delta W_{int} = -t_s \int_A \mathbf{S} : \delta \mathbf{E} dA = -t_s \int_A \begin{bmatrix} S_{11} \\ S_{22} \\ S_{12} \end{bmatrix} \cdot \begin{bmatrix} \delta E_{11} \\ \delta E_{22} \\ \delta E_{12} \end{bmatrix} dA. \tag{5.30}$$

Where $\mathbf{S}$ is the second Piola-Kirchhoff stress tensor, which can be decomposed into the elastic stress and the applied pre-stress to the membrane:

$$\mathbf{S} = \mathbf{S}_{el} + \mathbf{S}_{pre} = \mathbf{C} : \mathbf{E} + \mathbf{S}_{pre}. \tag{5.31}$$

$\mathbf{C}$ in Eqn. 5.31 is the elasticity tensor. The virtual work done by the external force is:

$$\delta W_{ext} = \lambda \int_A \mathbf{f} \cdot \delta \mathbf{u} dA \tag{5.32}$$

where $\mathbf{f}$ is the loading on the membrane element and λ is the load factor.

For nonlinear static analysis of the membrane problem in CARAT++, the linearized form of Eqn. 5.29 is solved iteratively using the Newton-Raphson method. The linearized form of Eqn. 5.29 after inserting the corresponding terms for internal and external work is:

$$\frac{\partial W}{\partial u_i}\delta u_i = -t_s \int_A \left(\mathbf{C} : \mathbf{E} + \mathbf{S}_{pre}\right) : \frac{\partial \mathbf{E}}{\partial u_i}\delta u_i dA + \lambda \int_A \mathbf{f} \cdot \frac{\partial \mathbf{u}}{\partial u_i}\delta u_i dA = 0. \tag{5.33}$$

Since the principal of virtual work is valid for any virtual displacement, equation 5.33 could be simplified by dividing it by the virtual displacement δu_i:

$$R_i = \frac{\partial W}{\partial u_i} = -t_s \int_A \left(\mathbf{C} : \mathbf{E} + \mathbf{S}_{pre}\right) : \frac{\partial \mathbf{E}}{\partial u_i} dA + \lambda \int_A \mathbf{f} \cdot \frac{\partial \mathbf{u}}{\partial u_i} dA = 0 \tag{5.34}$$

where R_i is the so-called out of balance force corresponding to the i^{th} degree of freedom. The out of balance vector of all the degrees of freedom are collected in the residual vector ($\mathbf{R}$). Convergence criterion for the nonlinear solution of the membrane problem is that the residual vector to converges to zero. This could be realized using predictor-corrector methods like displacement control, force control or arc length control [56].

5.3 Fluid-Structure Interaction

Fluid-Structure Interaction studies the interaction between a solid body and its surrounding fluid. The interface between the fluid field (Ω_F) and the structure field (Ω_S) is designated by Γ_I. The load from the fluid field is coupled with the displacement from the structure field. Two coupling conditions are enforced at the interface:

Kinematic continuity condition

Enforcing this constraint ensures that the fluid and structure interfaces lie on each other during the simulation. It is satisfied if the displacement at the fluid interface is the same as the displacement at the solid interface:

$$\mathbf{d}^F_{\Gamma_I}(t) = \mathbf{d}^S_{\Gamma_I}(t). \tag{5.35}$$

Dynamic continuity condition

Dynamic continuity condition is about mapping the correct force vector from the fluid interface to the solid interface. It implies:

$$\mathbf{f}^S_{\Gamma_I}(t) = \mathbf{f}^F_{\Gamma_I}(t). \tag{5.36}$$

There are two classes of methods for tackling FSI problems: Monolithic and partitioned methods. In the monolithic approach fluid and structure equations are merged into a single system of equations and are solved simultaneously, while in the partitioned approach the problem is divided into two separate sub-problems for fluid and structure field. Each field is solved separately in the partitioned approach and exchange of information takes place in a separate coupling step. The monolithic approach has an advantage over the partitioned one in terms of stability and accuracy [44]. On the other hand, solving the two fields independently in a modular environment provides the possibility of using the most efficient available solution techniques for each field [57]. The coupling in the partitioned approach is done either in an implicit or explicit way.

5.3.1 Explicit coupling

In explicit coupling, the coupling is implemented according to the flowing steps:

1. Solve the fluid problem for time step n.
2. Send the resulting force at the interface to the structure solver.
3. Solve the structure problem.
4. Send the calculated displacement to the fluid solver and proceed to the next time step.

Schematic representation of these steps is shown in Fig. 5.4.

Inter-field exchange of information occurs only once per time step in the explicit coupling. The calculated displacement at the end of the time step has been calculated based on the fluid load at the beginning of the time step. The loading at the end of the time step is different from the loading at the beginning of the time step, but this change is neglected in the explicit coupling. It is

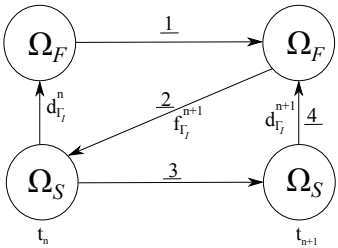

Figure 5.4: Explicit coupling scheme.

a source of error in the explicit coupling approach. The error might accumulate during the simulation and cause the simulation to crash. For cases where solid to fluid density ratio is high enough this might be a minor problem and accurate and stable solution might be obtained [58]. But it is not the case for less stiff structures. The stability issue for explicit coupling could be improved by using a predictor for interface displacement at the end of the time step [59]. The predictor uses the information from previous time steps to predict the position of the interface at the end of the current time step. This information is used to provide a better approximation of the loading from the fluid side at the end of the time step, resulting in a more stable solution.

5.3.2 Implicit coupling

In implicit coupling, stability is improved by performing multiple exchanges of information (inner iterations) between fluid and structure field within one single time step. Fig. 5.5 shows the procedure of exchange of information in implicit coupling between the two fields. Because of having multiple inner iterations in implicit coupling, this method is more accurate and more stable compared to explicit coupling.

In the following the structure problem is abbreviated by the function S and the fluid problem by the function F. On the structure side the solver receives the loading from the fluid solvers and calculates the displacement at the interface:

$$\mathbf{d}^{n+1}_{\Gamma_I} = S(\mathbf{f}^{n+1}_{\Gamma_I}). \tag{5.37}$$

For the fluid solver it is just the opposite, it receives the displacement at the interface and delivers the load applied by the fluid:

$$\mathbf{f}^{n+1}_{\Gamma_I} = F(\mathbf{d}^{n+1}_{\Gamma_I}). \tag{5.38}$$

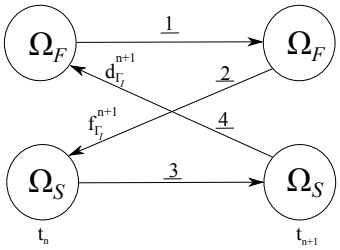

Figure 5.5: Implicit coupling scheme.

Inserting $\mathbf{d}_\Gamma$ from Eqn. 5.37 into Eqn. 5.38 yields:

$$\mathbf{d}_{\Gamma_I}^{n+1} = S(\mathbf{f}_{\Gamma_I}^{n+1}) = S\Big(F(\mathbf{d}_{\Gamma_I}^{n+1})\Big) = S \circ F(\mathbf{d}_{\Gamma_I}^{n+1}). \tag{5.39}$$

Equation 5.39 could be solved either using fixed-point iteration based methods or Newton-based methods. Within current thesis, Gauss-Seidel method is used to solve the equation iteratively. The iterations start from the initial guess for the interface displacement $\mathbf{d}_{\Gamma_I}$ and continue until it converges to the fixed point of $S \circ F$ function. The algorithm for the coupling is shown below:

for $i = 0$ *to* $NumTimeSteps$ **do**
  for $k = 0$ *to* $maxIter$ **do**
    predictor: $\mathbf{d}_{\Gamma_I,0}^{i+1} = \mathbf{d}_{\Gamma_I}^{i} + \Delta t \dot{\mathbf{d}}_{\Gamma_I}^{n}$;
    solve fluid: $\mathbf{f}_{\Gamma_I,k+1}^{n+1} = F(\mathbf{d}_{\Gamma_I,k}^{n+1})$;
    solve structure: $\mathbf{d}_{\Gamma_I,k+1}^{n+1} = S(\mathbf{f}_{\Gamma_I,k+1}^{n+1})$;
    check convergence;
    if *convergence* == *true* **then**
      break;
    end
  end
end

Algorithm 4: Implicit coupling using Gauss-Seidel method.

5.3.3 Mapping

The interface mesh at the fluid side is almost always finer than the mesh on the structure side. Non-matching mesh mapping techniques are necessary to cal-

culate the equivalent nodal force and nodal displacement at the FSI interface. Throughout this thesis, Mortar mapping method is used in the FSI simulations.

A basic criterion for mapping algorithms is consistency. It implies that a constant field is mapped exactly from one mesh to the other mesh. Another criterion is the conservation of energy, which is used to derive the so-called conservative mapping operators. In conservative mapping total energy is conserved as the fields are mapped between the meshes at the interface. The conservation of interface energy reads:

$$\int_{\Gamma} \mathbf{d}_{\Gamma}^{F^T} \mathbf{f}_{\Gamma}^{F} \, d\Gamma = \int_{\Gamma} \mathbf{d}_{\Gamma}^{S^T} \mathbf{f}_{\Gamma}^{S} \, d\Gamma. \tag{5.40}$$

Normal and dual mortar algorithms for mapping are not consistent in general. A novel technique for enforcing consistency on the mapping algorithm by scaling up the structural shape functions for the calculation of mapping matrices is utilized. Details of the formulation and its implementation are explained in [60].

6 *FSI Analysis Using Panel Method*

As discussed in chapter 5, Fluid-Structure Interaction (FSI) simulations are very time-consuming and computationally expensive. Depending on the complexity of the problem and the necessary degree of refinement, solving a multiphysics problem in an FSI framework might take several days or even weeks if an extremely fine discretization is used to resolve the turbulent fluid flow. It takes many inter-field iterations between the fluid and structural solver until convergence is reached. Consequently, solving the fluid problem, which is in general more time consuming than the structure problem, should be repeated multiple times for each time step which makes FSI simulations very costly. Using models with lower fidelity for the fluid problem is one way of getting a reasonable solution to the FSI problem in a shorter time frame. By using simpler models for the fluid problem some physical details of the fluid flow are neglected, but the overall cost-effectiveness of simpler approaches for flow modeling, e.g. the panel method, makes them a proper candidate for performing multi-fidelity FSI simulations. Limitations of the chosen method and its range of applicability have to be considered when it is opted for solving a specific coupled problem.

Panel method based approaches for FSI problems have been applied in analysis of certain coupled problems like biologically inspired flapping flight [61], horizontal axis tidal turbines [62], ship hydro-elasticity [63] and wind turbine computations [64].

In this chapter, a low-fidelity FSI simulation workflow using the vortex panel method (discussed in chapter 3) for solving the fluid problem is discussed. The cross-comparison between low-fidelity FSI simulation using panel method

(FSI_Panel) and the high-fidelity approach using the finite volume method via OpenFOAM (FSI_CFD) is made. The developed workflow could be used for performing both steady state and transient FSI analysis. It is applied for studying the aeroelastic characteristics of a demonstrative membrane wing with an aspect ratio of 4.5. Steady state and transient FSI analysis of the membrane wing follow.

Parts of the results presented in this chapter have been published in AIAA Journal of Aircraft [65]. They are presented here with written consent from the publisher.

6.1 Steady State FSI

The studied membrane wing with S809 airfoil profile can be seen in Fig. 6.1. It has a span of $4.5\,m$ and a uniform chord length of $1\,m$ along the span. Dihedral and sweep angles are both zero.

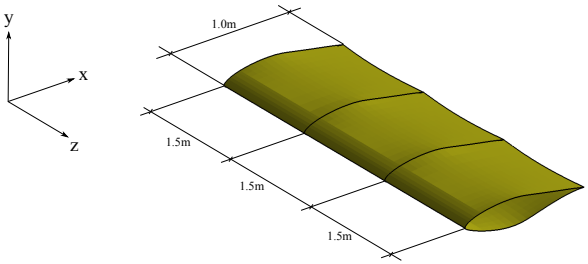

Figure 6.1: Isometric view of the wing.

The upper and lower membranes are attached to the rigid leading edge mast which extends up to 15% of the chord. The membranes are supported by 4 ribs and by an edge cable at the trailing edge. The 4 ribs divide the wing into 3 uniform segments. Structural properties of the membranes, ribs (which are modeled as beams) and the edge cables are summarized in Tables 6.1 to 6.3. The finite element model of the wing is shown in Fig. 6.2. It consists of four structural parts. The rigid leading edge extending up to 15% of the chord length. The ribs which are modeled as beams, the cable at the trailing edge which is modeled as truss and finally, upper and lower surface of the wing which are modeled via membrane elements with no bending stiffness.

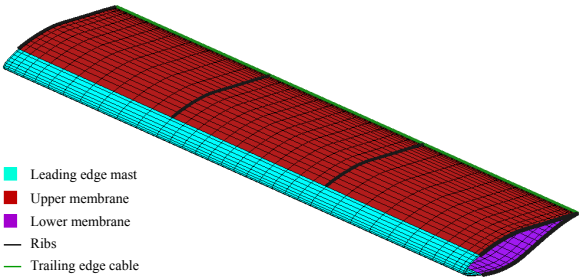

Figure 6.2: Finite element model of the wing.

6.1.1 Form Finding

Table 6.1: Membrane properties, (u: upper, l: lower)

E	$84\,MPa$
ρ	$1400\,kg/m^3$
t	$0.48\,mm$
$\sigma^u_{chordwise}$	$300\,kPa$
$\sigma^u_{spanwise}$	$1600\,kPa$
$\sigma^l_{chordwise}$	$300\,kPa$
$\sigma^l_{spanwise}$	$1600\,kPa$

Table 6.2: Trailing edge cable properties

E	$125\,GPa$
ρ	$7800\,kg/m^3$
$radius$	$4\,mm$
σ	$50\,MPa$

The equilibrium shape of the wing with the structural parameters presented in the Tables 6.1 to 6.3 is calculated using form finding analysis. The deformed state is compared with the reference state in Figs. 6.3 and 6.4. The membranes and the edge cables pull against each other and as a result, the edge cables are moved toward the leading edge with maximum displacement at the middle of each wing segment. The pre-stresses in the membranes form double-curved

Table 6.3: Beam properties

E	$190\,GPa$
ρ	$7800\,kg/m^3$
A	$2\,cm \times 12\,cm$

surfaces, where the upper membranes are moved downwards and lower membranes are moved upwards. While the cross section remains unchanged at the 4 ribs, due to the deformation of the two membranes, the cross section of the wing changes continuously on other sections along the span. Fig. 6.4 shows how the cross section at the middle of the wing deviates from the initial S809 profile.

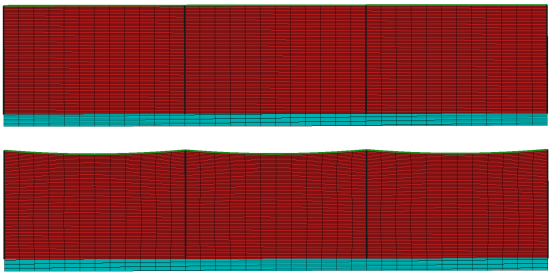

Figure 6.3: Form finding of the membrane wing. Top: initial state. Bottom: equilibrium state.

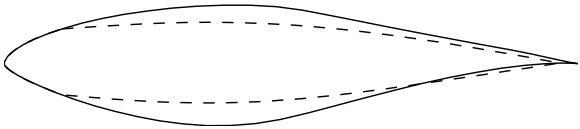

Figure 6.4: Form finding of the membrane wing (mid-span section). Solid line: initial state. Dashed line: equilibrium state.

6.1.2 Fluid Setup (FVM)

For the fluid side, SimpleFoam solver from OpenFOAM has been used for performing steady state CFD simulations using the finite volume method (FVM).

Necessary modifications to the solver are made to handle the moving mesh problem. Fig. 6.5 shows the discretized computational domain used for CFD simulations. It consists of about 2.9 million elements, which results in a y^+ value of about 70. To check if the mesh is fine enough, the results for the Reynolds number of $Re = 10^6$ are compared with the experimental and numerical results reported in [67]. The comparison has been made only up to an angle of attack of $9°$, for higher angles of attack a finer mesh is needed to properly capture stall effects.

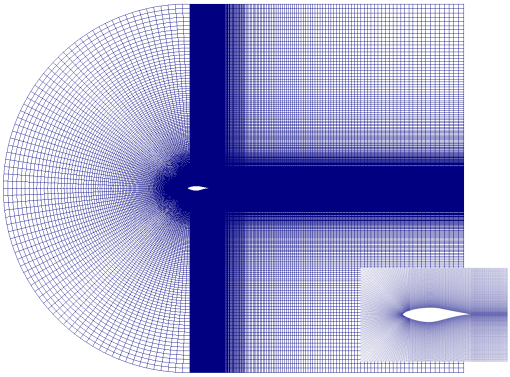

Figure 6.5: Computational domain.

The $k - \omega SST$ model has been used. OpenFOAM wall functions are used at the wing surface, kqRWallFunction for k and omegaWallFunction for ω. The velocity at the inlet is $30\,m/s$ which corresponds to a Reynolds number of 2×10^6.

6.1.3 FSI Simulations

FSI simulations have been done for 7 different angles of attack from $0°$ to $9°$ with an increment of $1.5°$. Convergence to the steady state solution for the case of using panel method solver is about 25 times faster than using the simpleFoam solver in OpenFOAM. For both cases, a relaxation factor of 0.15 has been used for the displacement field.

First, the convergence behavior of the displacements for each approach to the steady state solution is compared in Fig. 6.6. Displacement in the y direction for the point at the mid-span section of the wing with $x/c = 0.5$ is compared (c is the chord length). While with the panel method convergence is reached within 20 iterations, FSI simulation using SimpleFoam takes 450 iterations to

converge. The time each iteration takes is also different in the two approaches. Overall, in the case of the panel method convergence is reached approximately 25 times faster. For this particular case, FSI_CFD simulation takes about 7.5 hours to converge using 4 processors, but FSI_Panel converges within about 20 minutes on a single processor of the same machine. For $\alpha = 3°$ the converged displacement is $0.033m$ from FSI_Panel and $0.035m$ from FSI_CFD.

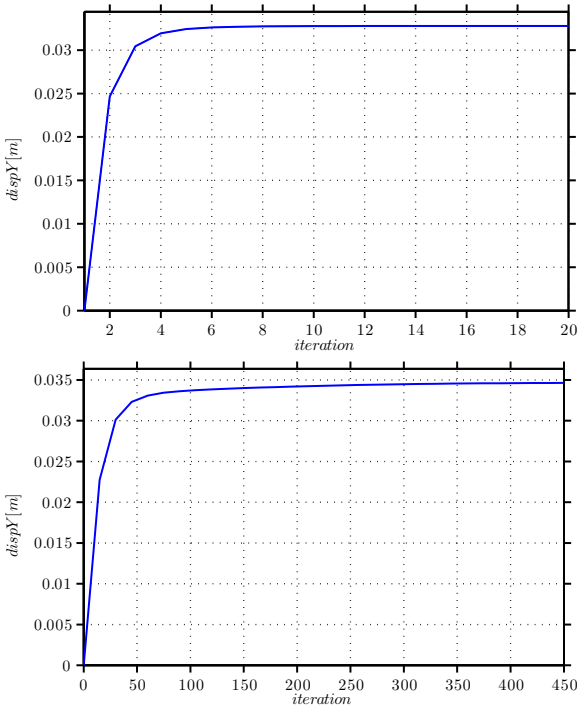

Figure 6.6: Convergence of the displacement for a selected point. Top: FSI_Panel. Bottom: FSI_CFD.

The comparison of the two approaches for the selected point is summarized in Table 6.4. For $\alpha = 0°$ both approaches result in the same displacement. But, it is not the case for higher angles of attack as the panel solver tends to underpredict the overall pressure distribution and as a consequence, it results in smaller displacements. It is not the case for $\alpha = 9°$. For this angle of attack, the panel solver overpredicts the pressure and results in a larger displacement. It should be a consequence of neglecting the viscous effects, which play an

Table 6.4: Comparison of displacement (m) in y direction at different angles of attack.

$\alpha(deg)$	FSI_Panel	FSI_CFD	$\%diff$
0	0.028	0.028	0
1.5	0.030	0.031	3.22
3	0.033	0.035	5.71
4.5	0.035	0.038	7.89
6	0.038	0.040	5.00
7.5	0.04	0.041	2.44
9	0.042	0.039	7.69

important role as the flow gets closer to the stall region at $\alpha = 9°$.

A better comparison can be made by comparing the displacement along the whole chord and not only at one certain point. This has been done for the section at the mid-span of the wing (Fig. 6.7). For the first 4 angles of attack (up to $4.5°$) and especially on the upper surface of the wing, there is a very good agreement between the resulting displacement from the two approaches. But from the angle of attack of $6°$, they start to deviate from each other.

As the angle of attack increases, viscous effects become more and more important. These effects are neglected in the panel method which causes its accuracy to decrease as the angle of attack is increased. Moreover, as the angle of attack increases, the pressure peak on the membrane part of the lower surface of the wing increases as well. The fluid pushes the membrane upward, while the leading edge part of the wing remains undeformed. This results in a discontinuity in the slope of the wing surface, as shown in Fig. 6.8. The panel solver is not able to capture the flow physics at the kink: it overpredicts the pressure in the vicinity of the kink and consequently the resulting displacement from the two solvers deviate from each other.

Membrane wings enable a lighter wing construction and their flexibility is an advantage in terms of dynamic loading applied to the wing. The lift coefficient of the membrane wing is compared with that of the baseline rigid wing. As it can be seen in Fig. 6.9, at smaller angles of attack, the rigid wing has better lift characteristics than the membrane wing, but from $\alpha \approx 2.5°$ it is the membrane wing which shows a higher lift coefficient. The reason for that is mainly the flexibility of the upper surface. The upper membrane is pulled upward which increases the thickness and the camber of the wing section and causes greater

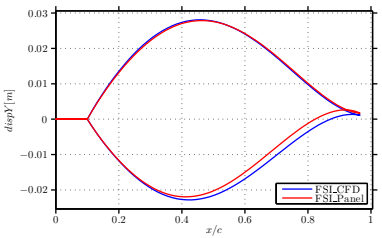

(a) $\alpha = 0.0°$

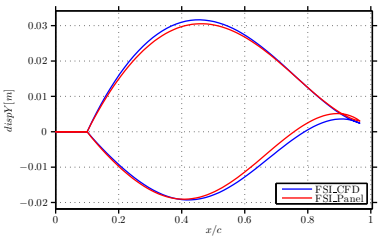

(b) $\alpha = 1.5°$

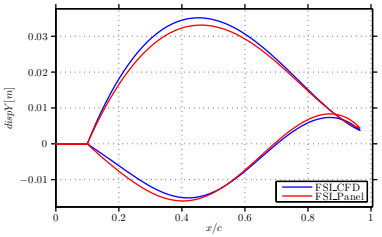

(c) $\alpha = 3.0°$

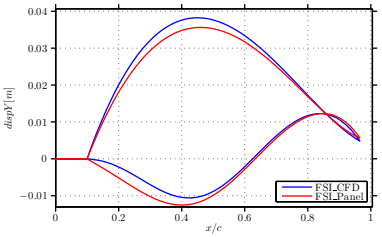

(d) $\alpha = 4.5°$

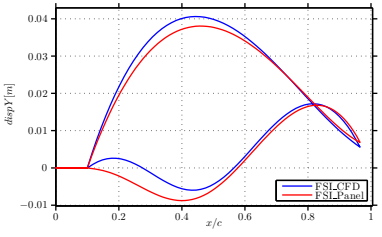

(e) $\alpha = 6.0°$

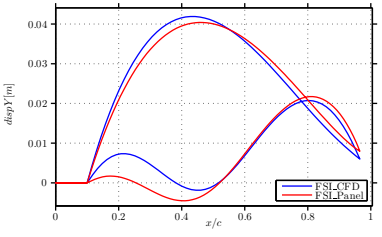

(f) $\alpha = 7.5°$

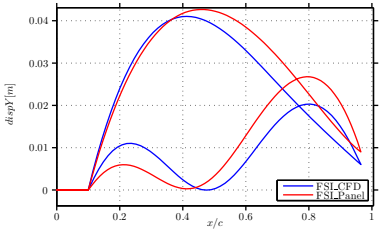

(g) $\alpha = 9.0°$

Figure 6.7: Displacement in y direction along the mid-span section. FSI_CFD: blue. FSI_Panel: red.

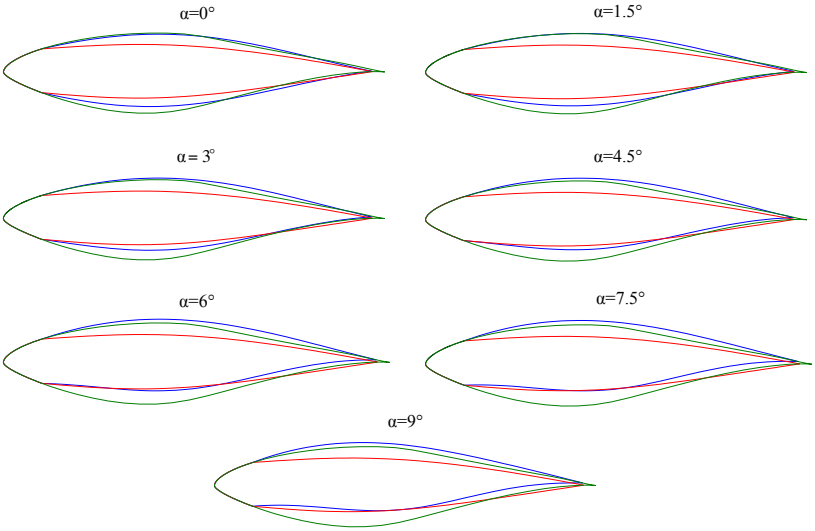

Figure 6.8: Cross section shape at the mid-span section. S809 airfoil: green. Undeformed section: red. Deformed section: blue.

lift compared with the rigid case.

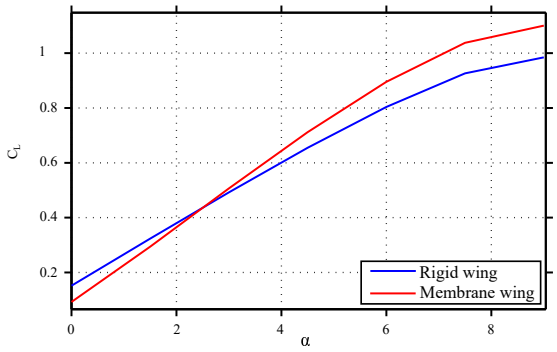

Figure 6.9: Comparison of the lift coefficient between the membrane wing and the rigid baseline wing.

Finally, it can be said that the panel method saves the computation time while providing a good accuracy up to an angle of attack of 6° . This makes the

panel method an appropriate tool for early design stages where an extensive parameter study needs to be done. The studied membrane wing concept has a higher slope of the lift curve as a function of the angle of attack.

6.2 Transient FSI

Unsteady FSI analysis of the same wing configuration (Fig. 6.1) with the very same structural properties is presented in the following. To study the influence of pre-stresses on the aerodynamic performance of the wing, three sets of pre-stresses have been investigated (Table 6.5). The stiffness of the membrane wing decreases and as a result its ability to adapt itself to the surrounding flow increases from $S1$ to $S3$.

Table 6.5: Pre-stress sets

	$\sigma_c^u(kPa)$	$\sigma_s^u(kPa)$	$\sigma_c^l(kPa)$	$\sigma_c^l(kPa)$	$\sigma_{cable}(MPa)$
$S1$	300	1600	300	1600	50
$S2$	200	1066.67	200	1066.67	33.33
$S3$	100	533.33	100	533.33	16.67

Total simulated time in FSI analysis is 3 seconds with a time step length of $\Delta t = 0.01\,s$. Newmark-Beta method with $\beta = 0.25$ and $\gamma = 0.5$ is used for time integration. To calculate the Rayleigh damping coefficients, modal analysis has been performed for the three pre-stress sets. The first two mode shapes of the $S2$ pre-stress set are demonstrated in Fig. 6.10. The first two natural frequencies and the coefficients of the Rayleigh damping are presented in Table 6.6. For these cases where the pre-stresses in the upper and lower membranes are the same, the first two eigenfrequencies are close to each other, but it is not the case when upper and lower membranes have different pre-stresses.

Table 6.6: Natural frequencies and Rayleigh damping coefficients

	$f_1(Hz)$	$f_2(Hz)$	$\alpha(s)$	$\beta(s^{-1})$
$S1$	15.36	15.74	9.7689	0.0010
$S2$	13.55	13.74	8.5730	0.0012
$S3$	10.35	10.40	6.5188	0.0015

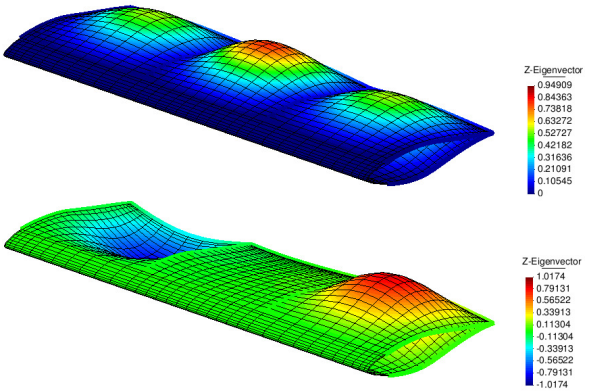

Figure 6.10: First (upper) and second (lower) mode shape for $S2$ pre-stress set.

6.2.1 Fluid Setup

The wing is discretized into 100 panels in the chordwise direction and 36 panels in the spanwise direction. The free stream velocity is $30\,m/s$. Simulations are done for a range of angles of attack from 0° to 9° with an increment of 1.5°. In order to save computational time, quadrilateral source terms are approximated as point sources as the distance from them reaches 20 times the maximum dimension of the largest panel (discretization is not uniform neither in the spanwise direction nor in chordwise direction). As the simulation goes on, the number of panels in the wake increases, which slows down the computation. As the wake panels are convected downstream of the wing, their influence of the wing panels decreases as their distance from the wing increases. Deleting the wake panels which are far away from the wing speeds up the computations without any visible influence on the results. Therefore, wake panels are truncated as their distance from the wing increases 30 times the mean aerodynamic chord of the wing. To ensure whether 30 times the mean aerodynamic chord is far enough for truncating wake panels, lift coefficient with and without wake panel truncation is compared in Fig. 6.11. Even though wake panels are deleted as their distance from the wing increases the pre-defined limit, lift coefficient converges to the value obtained without wake panel truncation. The presented example corresponds to flow around a wing with the S809 airfoil profile and an aspect ratio of 2 at an angle of attack of 5°. The wing has been discretized by about 3000 panels. Wake panels truncation reduces the

computational time by 20% for this case where only 3 seconds are simulated. The reduction in computational time with wake panels truncation increases for longer simulation time and with the higher number of panels in span direction of the wing.

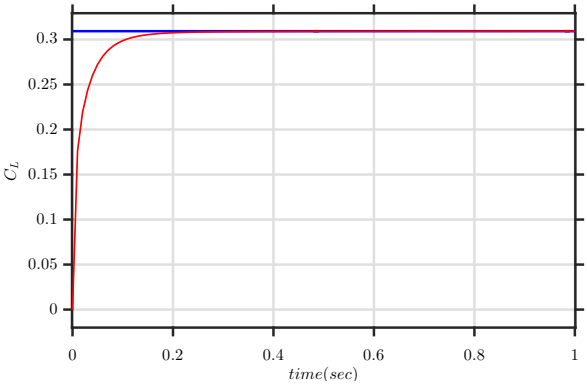

Figure 6.11: Comparison of the lift coefficient: with wake panels truncation (red) versus the converged value without wake panels truncation (blue).

Fig. 6.12 compares the obtained lift coefficients from the panel code implementation with XFLR5. Steady state results from XFLR5 are compared with the converged results from the unsteady panel code implementation with time independent inflow conditions. The average relative error for the 7 cases is 3.11%. Comparison of the pressure distribution from the two codes is also

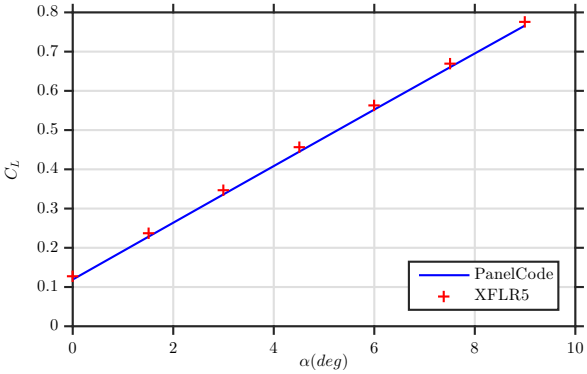

Figure 6.12: Comparison of the lift coefficient with XFLR5.

made in Fig. 6.13 for the case of $\alpha = 3°$.

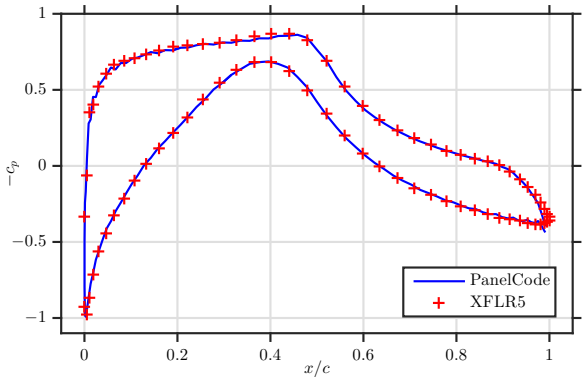

Figure 6.13: Comparison of the pressure coefficient at the middle section of the wing with XFLR5.

6.2.2 Results and Discussion

FSI simulations have been done for three different sets of pre-stresses and 7 angles of attack, from $0°$ to $9°$ with an increment of $1.5°$. Same surface discretization has been used for both fluid and structure side. Total simulation time is three seconds. In the form finding step, the membrane surfaces shrink and get closer to each other (Fig. 6.4), which decreases wing's thickness. During FSI simulation, the aerodynamic load is applied to the membranes. On the suction side of the wing, negative pressure causes the upper membrane to move upward. Depending on the angle of attack, either positive or negative pressure acts on the lower membrane, causing it to move upward or downward. Membrane deflection increases the thickness of the wing and as a result, lift increases. The goal of FSI analysis is to study the aerodynamic characteristics of the membrane wing for different pre-stress states, as they are one of the main design criterion of the membrane wing.

Transient behavior of the membrane wing could be studied using an unsteady fluid model coupled with a structural dynamics solver. Depending on the pre-stress level and the angle of attack, the membrane wing might demonstrate a steady or unsteady response. For the cases where the response is not transient and initial oscillations are damped after a while, the problem could be tackled using the steady state approach utilizing steady state panel method implemen-

tation coupled with static structure solver. Using the steady state approach, convergence to the steady state solution is reached at a much higher pace compared with the unsteady approach. However, if the instantaneous response of the membrane wing is of interest and not only the mean steady state response, the unsteady approach is inevitable.

In the following, verification of the unsteady aeroelastic tool against the steady one is presented. The steady aeroelastic code using steady panel method for the fluid part is itself verified against steady Navier-Stokes based FSI solver presented in section 6.1. The comparison between the steady and unsteady approach is made for two angles of attack with the $S2$ pre-stress set. For $\alpha = 4.5°$ the unsteady approach converges to the steady state solution, but for $\alpha = 7.5°$ there is no steady state response. Fig. 6.14 presents the comparison of the displacement at the selected monitor point in the mid-span section of the upper membrane at $x/c = 0.5$ from the two approaches. As expected, the unsteady solution converges to the steady state solution for $\alpha = 4.5°$, whereas for $\alpha = 7.5°$ without a physically steady state solution, the unsteady structural response oscillates around the steady state result. It should be noted that for the studied cases the transient approach takes approximately 13 times longer to converge compared with the steady state approach. Comparison of the calculated lift coefficient from the two solution approaches is also presented in Fig. 6.15.

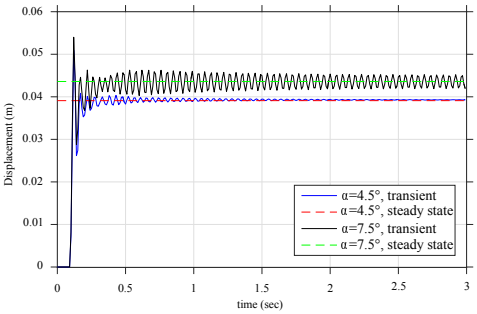

Figure 6.14: Displacement comparison between steady state and transient approach, S2 pre-stress set.

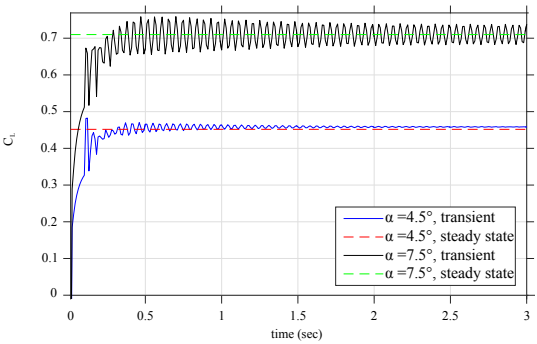

Figure 6.15: Lift coefficient comparison between steady state and transient approach, S2 pre-stress set.

Oscillations in lift coefficient

Because of the interaction between displacement and the applied load (mainly the lift force) the same oscillatory behavior is seen in the lift coefficient (Fig. 6.15). For a small angle of attack like 4.5° lift coefficient converges to a steady state value, whereas for $\alpha = 7.5^\circ$ there is no steady state solution and the lift coefficient continues to oscillate around a constant mean value. For the base airfoil of the wing (S809) stall happens at approximately 10°. For a conventional wing and at angles of attack lower than the stall point a steady lift coefficient is expected, but for the sailwing it is not the case. Due to self-excited vibrations in the membranes even for angles of attack smaller than 10° there is an oscillating lift coefficient.

Membrane deflection

The deformation of the membranes increases as the pre-stress is subsequently decreased from $S1$ to $S3$. Displacement at the selected monitor point located in mid-span section of the upper membrane at $x/c = 0.5$ is presented in Table 6.7. For smaller angles of attack where the membranes reach a steady state after initial vibrations, the steady state displacement is presented in the table, whereas for the cases in which oscillations are not damped over time, the mean value is presented. Pre-stresses in $S3$ are smaller compared with the other two sets. For $\alpha = 9^\circ$ at this pre-stress state wrinkles develop in the membranes

(Fig. 6.16), which suggests that higher pre-stresses are needed for $\alpha = 9^\circ$ at the studied wing configuration. It must be noted, that a detailed investigation of the wrinkling process would require a significantly refined structural mesh. These local structural instabilities have not been the topic of the current project.

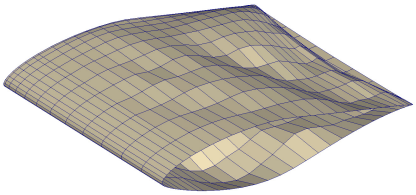

Figure 6.16: Development of wrinkles on membrane's surface for $S3$ pre-stress set at $\alpha = 9.0^\circ$.

Table 6.7: Membrane displacement (m) at the monitored point for different pre-stresses

$\alpha(deg)$	$S1$	$S2$	$S3$
0.0	0.0273	0.0315	0.0368
1.5	0.0290	0.0343	0.0402
3.0	0.0320	0.0368	0.0433
4.5	0.0342	0.0393	0.0459
6.0	0.0363	0.0416	0.0482
7.5	0.0382	0.0436	0.0501
9.0	0.0400	0.0454	-

Displacement of the monitored point over time for the $S2$ pre-stress set is plotted in Fig. 6.17. It should be mentioned that during the first 10 time steps no force and displacement transfer between the two solvers has been done to avoid initial overshoots in the membrane deformation because of high pressure spikes at the beginning of the unsteady solution process. As it can be seen, for smaller angles of attack up to 4.5° the membrane reaches the steady state after initial vibrations in the membrane, but for higher angles of attack vibrations are not damped over time and the membranes continue to oscillate.

These flow-induced vibrations are explored via spectral analysis of the response of the system, which is displayed in Fig. 6.18 for the three pre-stress sets at the studied angles of attack. As a result of membrane oscillations, vortices are shed in the wake of the wing. Development of the wake panels is

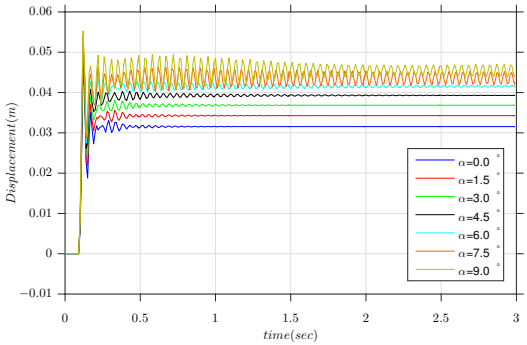

Figure 6.17: Displacement at the monitored point on the suction side, S2 pre-stress set.

shown in Fig. 6.19 for the S2 pre-stress set. For the cases where membrane oscillations are not damped with time, wake panels have an oscillatory pattern, too. The frequency of the oscillatory pattern in the wake panels correlates with the frequency of membrane oscillation, which itself correlates with the dominant frequency in spectral analysis of the lift coefficient.

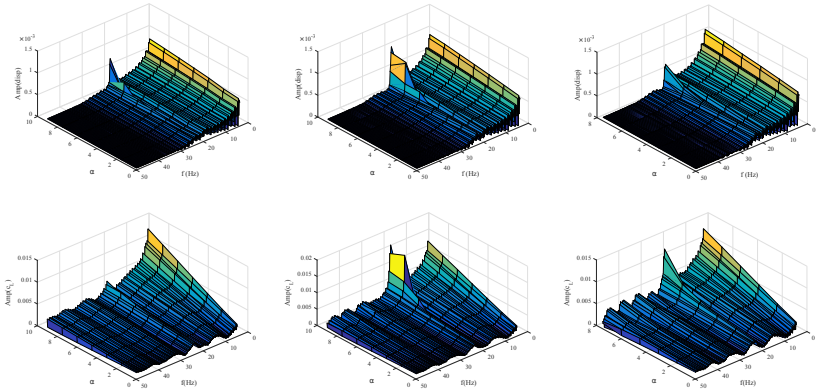

S1 pre-stress S2 pre-stress S3 pre-stress

Figure 6.18: Spectral analysis of displacement at the monitor point (top) and lift coefficient (bottom) for the three studied pre-stress sets.

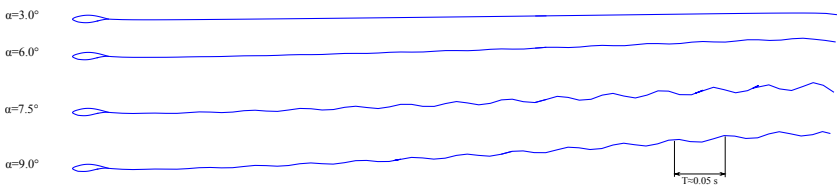

Figure 6.19: 2D slice of wake panels at the mid-span section of the wing, development of wake vortices for S2 pre-stress set.

Even though this dominant frequency is not exactly the same for the three studied pre-stress levels, the difference in the dominating frequency is not large and for all sets, it is about $21.5Hz$. As presented in Table 6.6, the first natural frequency for the 3 pre-stress sets are in the range of about $15Hz$, $13Hz$ and $10Hz$, respectively. But for all these sets the membrane is oscillating at a higher frequency. The difference in the natural frequencies of the unloaded membrane wing is due to the difference in the pre-stress level. The actual stress in the membrane is the sum of the pre-stress and the additional stress due to the elastic deformation of the membrane. In the presence of the aerodynamic loading the stress level in the membrane, and consequently, the natural frequency of the structure increases. The mean actual stress in chord direction for the three pre-stress sets is visualized in Fig. 6.20. The increase in pre-stress level from S3 to S2 is 100% and from S2 to S1 it is 50%. Yet the difference in the actual stress level is only about 4% in the consequent pre-stress cases. It shows that for the studied membrane with Young's modulus of $E = 84\,MPa$, induced stresses as a result of elastic deformation of the membrane have a greater contribution to the actual stress state, compared with the pre-stress. Since the actual stress level under the loading is quite similar for the three pre-stress cases, they should also have similar natural frequencies in the actual loading condition. This explains why for all the three studied pre-stress levels, the membrane oscillates at approximately the same frequency.

Comparison with the baseline rigid wing: Camber line

Next, the aerodynamic performance of the membrane wing is compared with that of the baseline rigid wing. Cross section of the membrane wing varies along the span, the profile of wing's cross section at the mid-span of the wing is shown for the $S2$ pre-stress set in Fig. 6.21. The red curve shows the cross section of the undeformed configuration ($t = 0.0\,s$), the green one shows the deformed configuration at $t = 3.0\,s$ and the blue curve is for the S809 air-

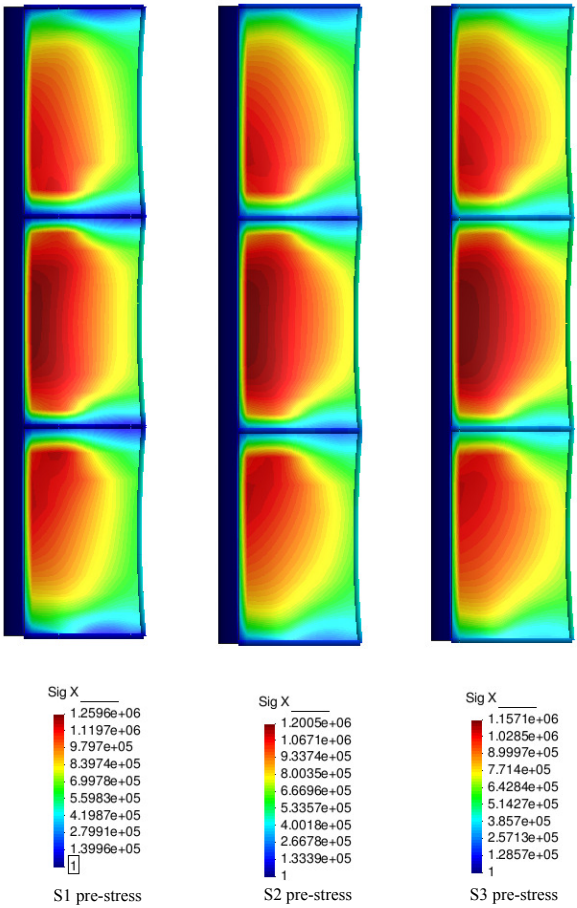

Figure 6.20: Distribution of mean stress in chordwise direction.

foil profile (rigid wing). Membrane's deformation changes the cross section properties of the wing like the maximum camber and thickness. The original S809 airfoil has a maximum camber of 1% at 82.3% chord position, but for the membrane wing, the maximum camber and its location change with the angle of attack (Table 7.6). It is also shown in Fig. 6.22 that with the increase of angle of attack the maximum camber increases as well and the point of maximum camber moves slightly towards the leading edge of the wing.

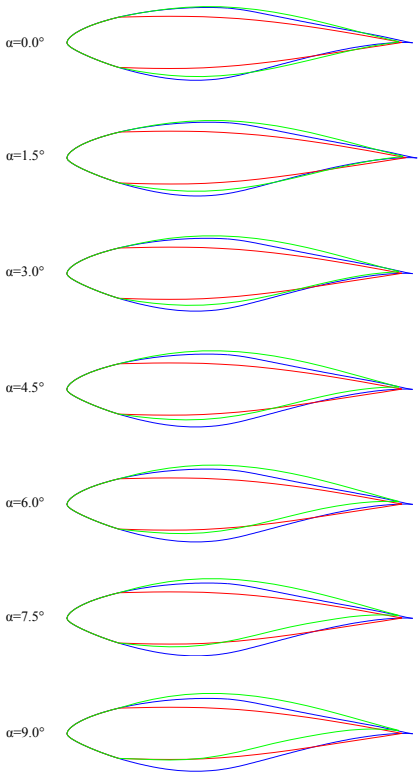

Figure 6.21: Cross section comparison at mid-span section of the wing. Blue: S809 Airfoil, Red: Undeformed configuration (output of form finding analysis), Green: deformed configuration.

Comparison with the baseline rigid wing: Pressure distribution

Pressure coefficient distribution at the mid-span section of the membrane wing for $\alpha = 6.0°$ is plotted in Fig. 6.23 for the three studied pre-stress levels. The distribution of the pressure coefficient of the membrane wing has kinks at $x/c = 0.15$ positions where the membrane is attached to the leading edge mast. The reason for that is the discontinuity in surface's slope at the attachment point. The area enclosed by the c_p curve shows the lift coefficient. It can be qualitatively seen that the membrane wing has a higher lift coefficient at its steady state for $S2$ and $S3$ pre-stress sets.

Table 6.8: Maximum camber and its location for the mid-span section

$\alpha(deg)$	maximum camber (%)	maximum camber location
0.0	0.67	69.61
1.5	1.00	69.60
3.0	1.38	69.57
4.5	1.82	69.54
6.0	2.28	69.50
7.5	2.67	64.73
9.0	3.05	64.72

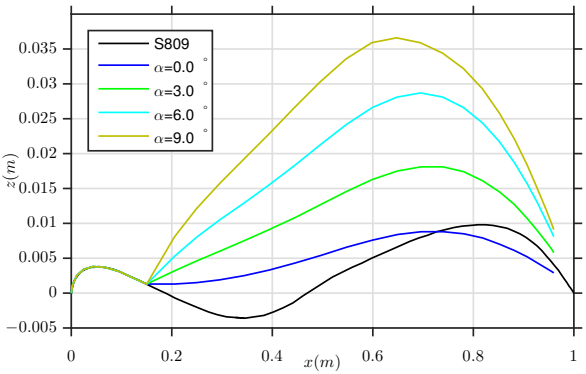

Figure 6.22: Comparison of camber line for $S2$ pre-stress case with S809 airfoil's camber line.

Cross section of the membrane wing at the mid-span section is plotted in Fig. 6.24 together with the $S809$ airfoil profile. The upward displacement of the trailing edge slightly reduces the effective angle of attack. It is not in favor of a higher lift coefficient compared with the rigid base wing, but the change in the profile due to membrane flexibility changes the pressure distribution over wing's surface. Comparing the pressure distributions of the base wing with the membrane wing (Fig. 6.23) it is observed that for the most part of the suction side, pressure coefficient for the membrane wing is lower (higher suction) than the rigid base wing. The difference increases with the increase of membrane's flexibility from $S1$ to $S3$ pre-stress level and as a result, the lift coefficient for the membrane wing is higher than that of the rigid base wing for $S2$ and $S3$ pre-stress levels. A quantitative comparison is made in the next section.

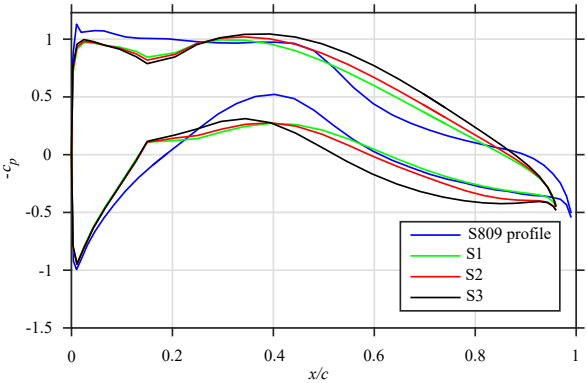

Figure 6.23: Comparison between pressure distribution over the mid-span section of the conventional S809 profile wing with membrane wing with different pre-stress levels.

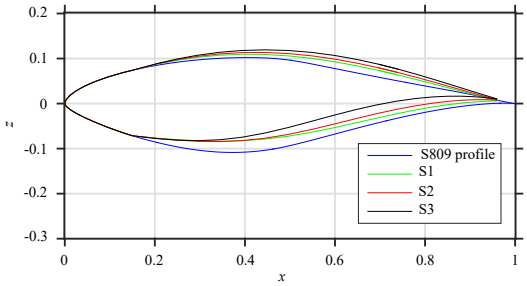

Figure 6.24: Comparison of the converged cross section profile at mid-span section for different pre-stress levels ($\alpha = 6°$).

Comparison with the baseline rigid wing: Lift coefficient

Comparison of the lift coefficient for different pre-stress levels is made in Fig. 6.25. For all three pre-stress sets the membrane wing has smaller lift coefficient at zero angle of attack. The slope of the lift curve increases as the flexibility of the membrane wing is increased by reducing the pre-stress level. For all three cases, the lift curve of the membrane wing has a higher mean slope than the

conventional rigid wing. As a result, after a certain angle of attack (depending on the pre-stress level) the membrane wing demonstrates better lift characteristics. In the case of $S3$ there is an improvement in lift coefficient even for $\alpha = 1.5°$, while for a stiffer membrane wing configuration ($S1$), the improvement in lift coefficient is observed only for $\alpha = 7.5°$ and $\alpha = 9.0°$. Table 6.9 summarizes the percentage of change in lift coefficient for the three cases compared with the conventional rigid wing. The reason for the decline in lift coefficient for $\alpha = 0.0°$ compared to the base wing is that at the unloaded situation the membrane wing has a quite symmetric airfoil profile (red curves in Fig. 6.21). For $\alpha = 0.0°$ the lift coefficient of the membrane wing is compared with a non-symmetric wing profile (S809 airfoil) and as a result, the highest decline is observed at $\alpha = 0.0°$. For other angles of attack, the membrane wing's profile becomes more unsymmetrical with the increase in angle of attack and its lift coefficient compares better with the baseline rigid wing.

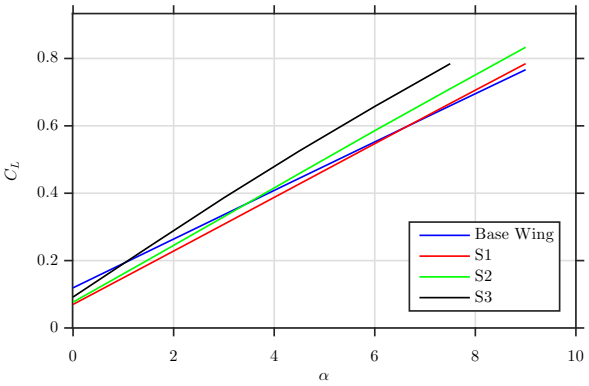

Figure 6.25: Lift coefficient for different pre-stress sets.

Table 6.9: Percentage of change in c_L compared with conventional rigid wing

α	0.0	1.5	3.0	4.5	6.0	7.5	9.0
$S1$	-41.3	-17.2	-8.4	-3.8	-0.9	1.0	2.3
$S2$	-35.7	-11.0	-1.8	3.2	6.1	7.6	8.7
$S3$	-22.9	5.4	14.9	18.2	19.1	18.1	-

Trailing edge flexibility

Finally, the influence of trailing edge flexibility on the overall response of the coupled system is presented. As summarized in Table 6.10, elastic deformation of the trailing edge cable causes a slight improvement in the lift coefficient. The table compares the lift coefficient of the membrane wing with an elastic trailing edge cable with that of the wing with a rigid trailing edge.

Table 6.10: Percentage of change in c_L compared with the membrane wing with rigid trailing edge

$\alpha(deg)$	0.0	1.5	3.0	4.5	6.0	7.5	9.0
$\%\Delta c_L$	4.50	2.01	1.69	2.07	2.07	2.13	2.32

Converged cross section profile and camber line at the mid-span section of the membrane wing are shown in Fig. 6.26 for $\alpha = 4.5°$. The membrane wing has higher camber and airfoil thickness in the case of an elastic trailing edge cable. The elastic deformation of the trailing edge influences the structural response

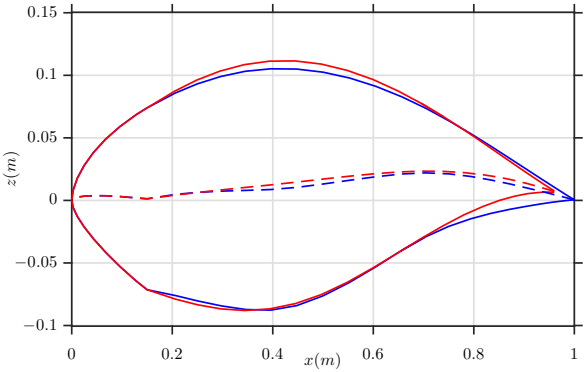

Figure 6.26: Cross section and camber line (dashed) comparison between rigid trailing edge(blue) and elastic trailing edge(red).

of the wing as well. While for the elastic trailing edge the membrane oscillations are present for $\alpha = 7.5°$ and $\alpha = 9.0°$ and are damped for smaller angles of attack, for the case of rigid trailing edge cable the membrane continues to oscillate for angles of attack bigger than $\alpha = 3.0°$. The fact that the trailing edge shape adapts itself to membrane's deflection proves to help to mitigate the vibration of the membrane. It postpones not only the oscillatory response

to higher angles of attack for a specific set of pre-stress but also reduces the amplitude of the oscillations as shown in Fig. 6.27 for $\alpha = 7.5°$. The figure presents the spectral analysis of displacement at the monitor point. For the rigid trailing edge, there are more than only one dominant frequency and the amplitude of the oscillations is higher compared with the case of an elastic trailing edge cable.

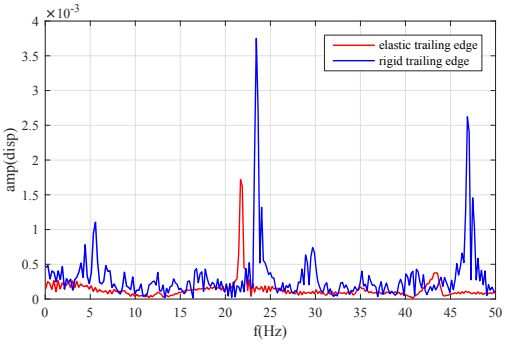

Figure 6.27: Spectral analysis of membrane oscillation, comparison of rigid and elastic trailing edge.

6.2.3 Conclusion

The panel method enables faster exploration of the design space. On a standard PC (3.40 GHz, 8 M Cache, 15 GB RAM) it takes about 90 minutes to run three seconds of FSI simulation (transient approach). Transient results converge to the results obtained from the steady approach for the cases where a steady state solution exists. Even though using panel method for flow modeling facilitates faster design evaluations and a comprehensive study of the design envelope at a lower cost during early design stages, limitations of the method should also be considered. Since no boundary layer model is coupled with the current panel method implementation, viscous drag is not included in the model. In determining the final shape of the membrane, pressure force plays a much more important role than the viscous drag. However, the final design should inevitably be studied using a high-fidelity FSI analysis which is done in the upcoming chapter.

Comparing the performance of the membrane wing with the baseline rigid wing, the following main observations have been made:

1. Increase in the camber for the membrane wing as well as shifting of the point of maximum camber towards the leading edge.

2. Higher lift curve slope for the membrane wing. A lower lift coefficient for zero angle of attack is observed for the membrane wing, but due to the higher lift curve slope, the membrane wing has higher lift coefficient than the baseline wing for higher angles of attack.

3. Vortex-induced oscillations have been observed for the membrane wing at higher angles of attack. Depending on the pre-stress level, they have been present either from $\alpha = 6.0^\circ$ or from $\alpha = 7.5^\circ$. For both cases, the stall point is not reached yet, but as a consequence of membrane vibration, oscillations in lift coefficient are observed for the membrane wing even before the stall angle of attack. The lift coefficient in these cases oscillates around a constant mean which is higher than that of the baseline rigid wing. The actual stress state in the membrane is dominated by induced stresses due to the elastic deformation. Even though different pre-stresses are set for the initial configuration, resulting in different natural frequencies for the membrane wing configuration, actual stress distribution is quite the same regardless of the pre-stress value. Consequently, membrane oscillations in the three different pre-stress configuration share approximately the same frequency.

4. Elastic deformation of the trailing edge cable improves the lift coefficient of the membrane wing and postpones membrane vibration to higher angles of attack. The flexibility of the trailing edge reduces the amplitude of the membrane vibration as well.

7 *The Membrane Blade*

This chapter utilizes the methods discussed so far in the thesis for the analysis of the membrane blade concept. The analysis is done in three levels. Every level of the analysis compares the performance of the membrane blade with the baseline rigid blade which is the NASA-Ames Phase VI blade (Appendix B).

First, steady-state and transient FSI analysis of the blade in non-rotating configuration is performed. The steady-state analysis follows the idea of multi-fidelity analysis by using both panel method and CFD for solving the fluid problem.

Next, a workflow for using the blade element momentum (BEM) method, as the most common tool for aerodynamic analysis of wind turbines, for the analysis of the membrane blade is proposed and tested in both steady-state and transient condition, considering the rotation of the rotor. In classical BEM, look-up tables for the lift and drag coefficients at different angles of attack and for a range of Reynolds number are used. For BEM analysis of the membrane blade, these tables are substituted with the two-dimensional panel code solver discussed in Section 3.1.

Finally, high-fidelity FSI analysis of the membrane blade in steady-state condition is presented in Section 7.4. The rotation of the blade is modeled using the Multi Reference Frame (MRF) approach in OpenFOAM. At all of the three levels of the analysis, the membrane blade promises certain advantages over the rigid baseline blade in terms of the lift force or the generated power which are discussed in the upcoming sections.

Parts of the results presented in this chapter have been published in Wind Energy Science Journal [68] and Journal of Physics [69]. They are presented here with written consent from the publisher.

7.1 The Membrane Blade Concept

The *Sailwing* concept was proposed by Ormiston during the $70's$ [15]. The basic schematic of the sailwing can be seen in Fig. 7.1. The main frame of the sailwing consists of a leading edge mast which is assumed to be rigid and a number of ribs which are connected to the leading edge mast along the span of the wing. Upper and lower surfaces of the wing are elastic, pre-stressed membranes connected to the mast and to the ribs. The membranes are supported at the trailing edge by pretensioned edge cables. The form of the wing in the operating condition depends on the interaction between the internal forces of the wing configuration and the aerodynamic loading.

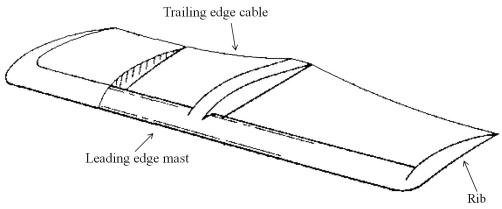

Figure 7.1: Sailwing construction concept, from [15]

In the absence of aerodynamic loads, the shape of the sailwing is determined by the equilibrium of membrane and edge cable forces. In the unloaded state, membranes form a concave, double-curved surface. In the operating condition, the applied aerodynamic load deforms the membranes and edge cables. The interaction between external aerodynamic force and the internal pretensions governs the form of wing's surface and its aerodynamic characteristics. As a result, fully-coupled fluid-structure interaction analysis is needed to evaluate the actual performance of the sailwing. Having the upper and lower surface of the wing made out of membranes with a weight of about $1 - 1.5\,kg/m^2$ facilitates light-weight construction of the wing. The flexibility of the sailwing enables it to adapt itself to the flow condition to some extent which promises a favorable loading on the wing in terms of fatigue life.

The studied membrane blade is inspired by the sailwing concept. It can be

seen in Fig. 7.2. It is basically the layout of the NASA-Ames Phase VI rotor with a length of $5.029\,m$ [70]. The chord length varies along the blade, with $0.73\,m$ at the root of the blade (after the transition from cylindrical hub profile to the airfoil profile) to $0.35\,m$ at the tip of the blade. The upper and lower membranes are attached to the rigid leading edge which extends up to 15% of the chord length. The membranes are supported by 4 ribs and by 4 edge cables at the trailing edges. The 4 ribs divide the blade into 4 segments with equal span.

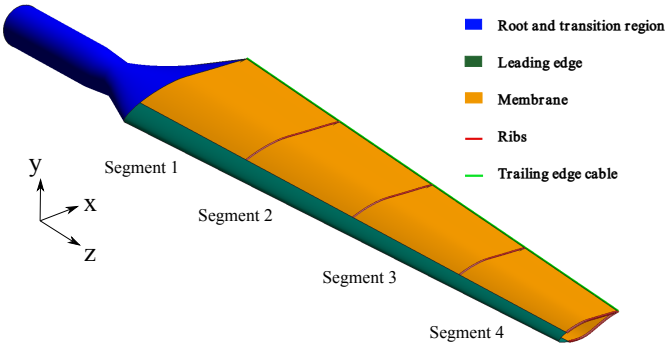

Figure 7.2: Membrane blade planform (without twist)

7.2 Membrane blade in non-rotating configuration

In this section analysis of the membrane blade in non-rotating, uniform flow condition is presented. The blade does not need to be twisted since the non-rotating condition is studied. Steady-state and transient FSI analysis of the membrane blade follows in the sequel:

7.2.1 Steady-state FSI analysis

Two different modeling levels are being used for the steady-state FSI analysis of the membrane blade. A lower-fidelity approach is utilized by the coupling between the panel method solver and the structural solver as discussed in chapter 6. The low fidelity approach is very robust and efficient for early-stage design space exploration, specially for deciding about the pre-stresses.

Comparison of the low-fidelity approach and high-fidelity FSI simulation using OpenFOAM as the fluid solver is presented in the upcoming sections. The analysis starts with form finding simulation. In form finding, the equilibrium state of the wing is calculated, i.e. the state where the membrane and edge cable's internal forces are in equilibrium. This is the initial shape of the blade surface in the absence of external forces. FSI simulations start from this initial state. In the following sections fluid, structure and coupling related aspects are explained in detail. The overall simulation workflow is shown in Fig. 7.3, which demonstrates the sequence of the analysis.

The process of solving the flow problem for both approaches is presented in the figure as well. At each coupling iteration, the fluid solver receives the displacement from the structural solver and updates the mesh. Then the fluid problem is solved for the updated mesh. It should be noted that in solving the problem using finite volume method all the steps include operations performed on a three-dimensional mesh, whereas in panel method the mesh consists of a two-dimensional surface discretization. For the case of mesh update in particular, for the panel method discretization updating the mesh means adding the displacement at each node to the original coordinate of the node, but for the three-dimensional volume mesh, in addition to applying the displacement on the boundary, the displacement of the interior points should also be calculated. In addition to the higher computational cost of the three-dimensional mesh morphing, it is also a challenge to keep the quality of the volume elements as they deform.

7.2.1.1 Model setup

The blade configuration and its decomposition into different structural parts is shown in Fig. 7.2. The properties of the three different structural parts are summarized in table 7.1:

Table 7.1: Properties of the structural parts.

Membrane		Edge cable		Rib	
E	$84\,MPa$	E	$125\,GPa$	E	$190\,GPa$
ρ	$1400\,kg/m^3$	ρ	$7800\,kg/m^3$	ρ	$7800\,kg/m^3$
t	$0.48\,mm$	$radius$	$4\,mm$	A	$2\,cm \times 12\,cm$

The pre-stresses in the membranes and the edge cables are summarized in Ta-

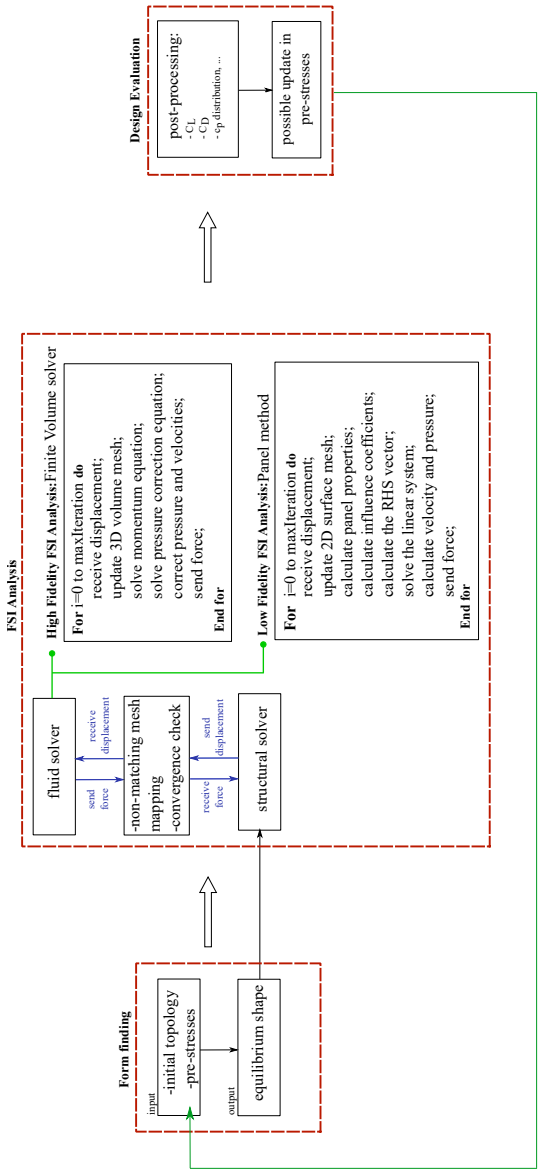

Figure 7.3: Schematic representation of the multi-fidelity analysis work flow

ble 7.2. For the membrane pre-stresses, the superscript distinguishes between membranes on the upper (suction) and lower (pressure) side of the blade, while the subscript designates the direction of the applied pre-stress. These pre-stresses correspond to the pre-stresses in the first segment of the blade. For the remaining three segments the pre-stresses are scaled according to the dimensions of the segment. Since all segments have the same span, the pre-stress in spanwise direction is the same at all segments. But, the pre-stress in chordwise direction is scaled with the mean chord length for the three other segments.

Table 7.2: Membrane and edge cable pre-stresses.

$\sigma^{u}_{chordwise}$	$180\,kPa$
$\sigma^{u}_{spanwise}$	$480\,kPa$
$\sigma^{l}_{chordwise}$	$180\,kPa$
$\sigma^{l}_{spanwise}$	$480\,kPa$
σ^{l}_{cable}	$30\,MPa$

7.2.1.2 Form finding

The equilibrium state of the blade with the structural parameters presented in Tables 7.1 and 7.2 is calculated in form finding analysis. The deformed state is compared with the undeformed state in Fig. 7.4.

Membranes and the edge cables pull against each other and as a result, the edge cables are moved toward the leading edge with maximum displacement at the middle of each blade segment. Because of the pre-stresses in the membranes and the curved structural frame to which the membranes are connected, double-curved membrane surfaces are formed where the upper membranes are moved downwards and lower membranes are moved upwards. Fig. 7.5 shows how the cross section at the middle of the second segment deviates from the initial cross section (which is the S809 airfoil profile) and how the upper and lower membranes pull the elastic trailing edge cable toward the leading edge.

7.2.1.3 Fluid setup

For the fluid side, SimpleFoam solver from OpenFOAM has been used for performing steady state CFD simulations. The schematic representation of the blocking strategy is presented in Fig. 7.6. The Computational domain together

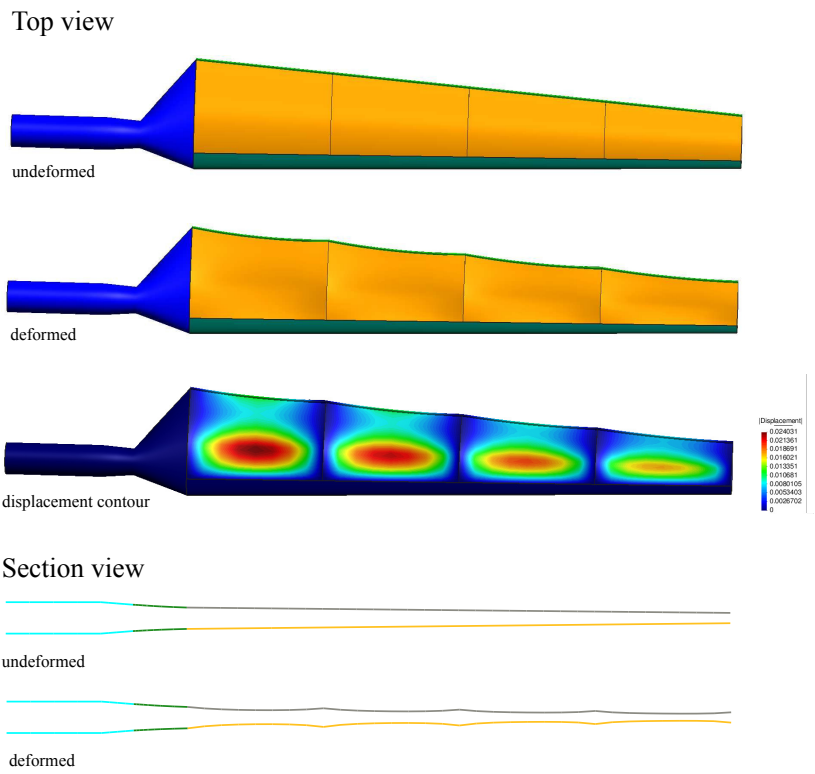

Figure 7.4: Form finding of the membrane blade. Undeformed and deformed geometry from top and front views.

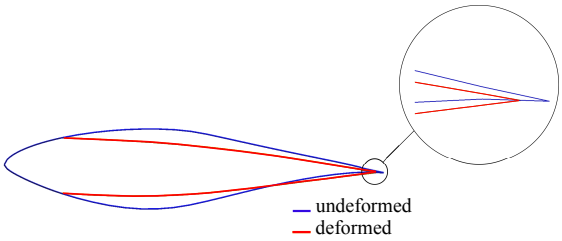

Figure 7.5: Form finding of the membrane blade (mid-span section, second segment).

with the mesh in the vicinity of the blade are shown in Fig. 7.7.

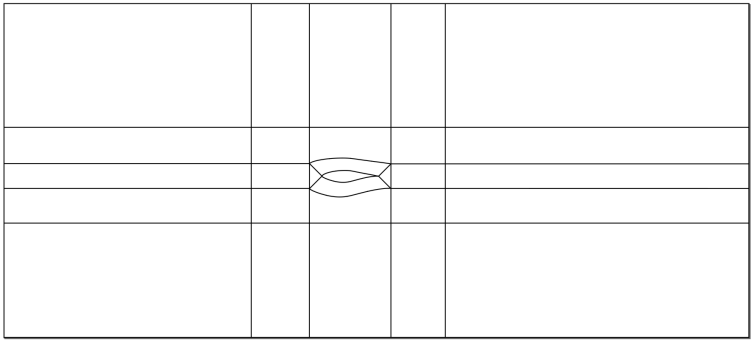

Figure 7.6: Blocking structure for the fluid mesh

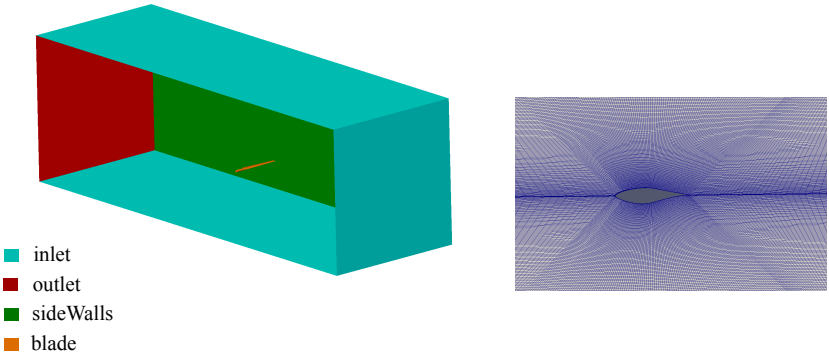

Figure 7.7: Left: Fluid Domain, Right: Fluid mesh in the vicinity of the blade

The domain size is $15\,m \times 15\,m \times 45\,m$, which results in a blockage ratio of about 0.3%. The tip of the blade has a distance of $10\,m$ to the far field boundary. The domain is discretized with a total of 2.9 million cells (hexahedral and prism elements), which results in a maximum y^+ value of about 70. Fig. 7.8 presents the result of the mesh convergence study performed for the rigid blade configuration at $\alpha = 4.0°$. As it can be seen, C_L has converged for the mesh with 2.9 million elements.

The $k - \omega SST$ model has been used for turbulence modeling. OpenFOAM wall functions have been used at blade's surface, kqRWallFunction for k and omegaWallFunction for ω. The velocity at the inlet is $30m/s$. The boundary

conditions for the fluid simulation are summarized in table 7.3.

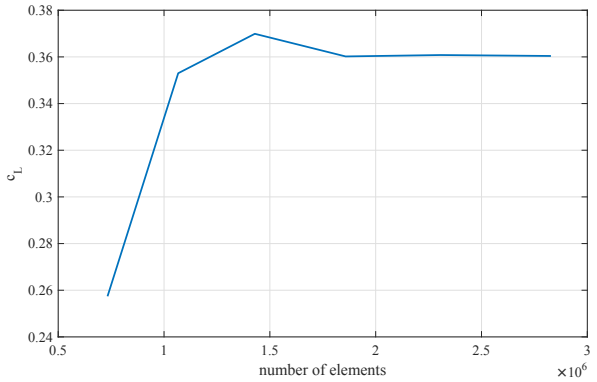

Figure 7.8: Mesh convergence study for the rigid blade, $\alpha = 4.0°$

Table 7.3: Boundary conditions for CFD simulations

boundary	U	p	k	ω
inlet	fixedValue uniform (u, v, w)	zeroGradient	fixedValue uniform $k = \frac{0.1U_\infty^2}{Re_L}$	fixedValue uniform $\omega = \frac{10*U_\infty}{L}$
outlet	zeroGradient	fixedValue uniform 0	zeroGradient	zeroGradient
sideWalls	symmetryPlane	symmetryPlane	symmetryPlane	symmetryPlane
blade	fixedValue uniform $(0, 0, 0)$	zeroGradient	kqRWallFunction uniform 1^{-10}	omegaWallFunction uniform $\omega = 10\frac{6\nu}{\beta_1(\Delta d_1)^2}$

7.2.1.4 FSI Simulations

FSI simulations have been done for 6 different angles of attack from $0°$ to $9°$. In the following FSI_CFD is used for simulations using finite volume method for the fluid side and FSI_Panel is used for simulations which use the panel method for flow modeling. Because of blade's deformation in FSI simulations, the fluid solver should in addition to solving the fluid flow problem, take care of the movement in the mesh as well. For the FSI_CFD case the deformation of the blade, which is applied to the blade patch is diffused into the fluid domain. This means that the boundary motion is distributed into the volume mesh and zero displacement condition is applied at the far field boundaries of the fluid domain.To solve the mesh motion problem the *displacementLaplacian* based

solver from OpenFOAM has been used with the *quadratic inverseDistance* diffusion method.

Convergence to steady state solution for the case of using the panel method solver is about 30 times faster than using the simpleFoam solver from OpenFOAM as the fluid solver. The panel code was run on a single processor, while for OpenFOAM simulations 10 processors were used. For both cases, a relaxation factor of 0.15 has been used for the displacement field for all angles of attack except for $\alpha = 7.5^\circ$ and $\alpha = 9.0^\circ$, where the relaxation factor was reduced to 0.1 to improve stability in the FSI run. Under relaxation is applied in order not to send the total calculated displacement at an increment to the fluid solver, but to send a fraction of that to improve the stability of the coupling algorithm and preserve the quality of the mesh on the fluid side:

$$\mathbf{d}^{n+1}_{\Gamma_{I,sent}} = \omega_r \mathbf{d}^{n+1}_{\Gamma_{I,calculated}} + (1-\omega_r)\mathbf{d}^{n}_{\Gamma_I} \tag{7.1}$$

The relaxation factor (ω_r) should be kept below some limit (which is case-dependent) for FSI_CFD simulations, otherwise, the quality of the finite volume mesh cannot be preserved during the simulation and the simulation might crash as a result of having highly distorted elements in the mesh. The same relaxation factor has been used for FSI_Panel case. The reason for using the same relaxation factor is to have a rather fair comparison between the convergence behavior of the two approaches, but it must be mentioned, that for FSI_Panel cases a higher relaxation factor can be used as well to have faster convergence without getting stability problems due to distorted elements in the mesh, which is in this case just a discretized surface.

First, the convergence behavior of the displacements to the steady state solution for each approach is compared (Fig. 7.9). Displacement of the point at the mid-span section of segment 2 (Fig. 7.2) with $x/c = 0.5$ is compared (c is the chord length). While with the panel method convergence is reached within 25 iterations, FSI simulation using SimpleFoam takes 450 iterations to converge. The time each iteration takes is also different in the two approaches. Overall, in the case of the panel method convergence is reached approximately 30 times faster. For this particular case, FSI_CFD simulation has taken about 10 hours to converge using 10 processors, but FSI_Panel has converged within about 20 minutes on a single processor. For $\alpha = 4^\circ$ the converged displacement is $0.0221\,m$ from FSI_Panel and $0.0211\,m$ from FSI_CFD, which demonstrates clearly the applicability of the low-fidelity approach, provided that the blade operating condition is in agreement with the respective modeling assumptions.

Comparison of the two approaches for the selected monitor point is summa-

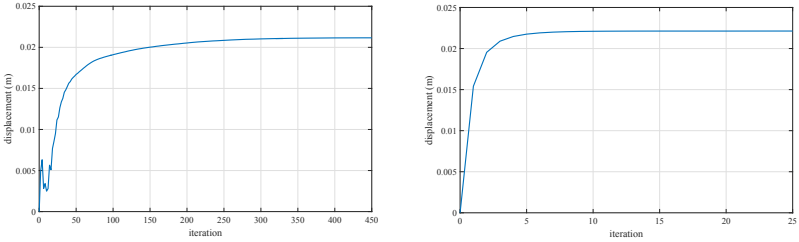

Figure 7.9: Convergence of the displacement for the selected monitor point. Left: FSI_CFD. Right: FSI_Panel.

rized in Table 7.4. For $\alpha = 0°$ the difference in the calculated displacement from the two approaches is 2.87%. The difference increases with angle of attack. For the base airfoil of the studied blade, the S809 profile, stall happens at $\alpha \approx 10°$. With the emergence of stall and flow separation, the assumptions of the panel method are no more valid. This explains the increased deviation of FSI_Panel result from FSI_CFD result for $\alpha = 9°$.

Table 7.4: Comparison of displacement (m) in y direction for different angles of attack

$\alpha(deg)$	FSI_Panel	FSI_CFD	$\%diff$
0.0	0.0175	0.0170	2.87
2.0	0.0198	0.0189	4.74
4.0	0.0221	0.0211	4.73
6.0	0.0241	0.0231	4.38
7.5	0.0252	0.0241	4.53
9.0	0.0255	0.0237	7.68

After local comparison of the calculated displacements from the two approaches in Table 7.4 for a single monitor point, a more global comparison is made by comparing the converged cross section shape at the steady-state. Fig. 7.10 shows the cross section of the blade in the middle of segment 2. For the upper surface of the blade, there is a very good agreement between the two methods, even though the difference increases with the increase of the angle of attack which is to be expected. The difference in the converged shape is higher for the lower surface and particularly for $\alpha = 7.5°$ and $\alpha = 9.0°$. It can be explained by the increased discontinuity in the slope of the surface at the point

where the lower membrane is attached to the leading edge mast. There is a kink at the point of attachment which is much more visible for higher angles of attack. The local flow separation downstream of the kink is not captured by the panel method, which results in different pressure distributions and as a consequence different converged shapes for the two approaches.

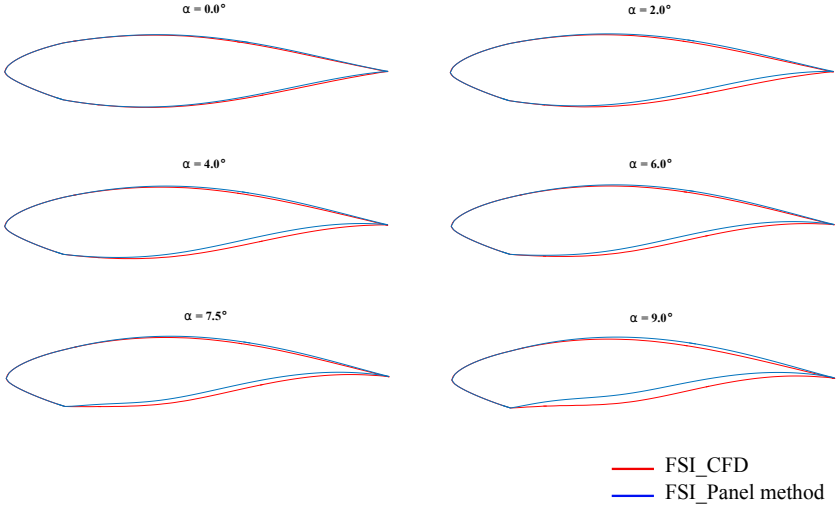

Figure 7.10: Comparison of the converged cross section at the mid-span section of the second segment.

The membrane blade concept facilitates a lighter blade construction due to the optimal load carrying behavior and also due to its capability to alleviate peak loading because of its deformation. It should also have an improved performance compared to rigid blade configurations in the stall region because of the so-called ”soft stall characteristics” of the membrane wings [7]. In order to assess the aerodynamic performance of the studied blade, lift coefficient, drag coefficient and lift to drag ratio of the blade are compared with the baseline rigid blade. As it can be seen in Fig. 7.11, for smaller angles of attack the membrane blade has a smaller lift and drag coefficient compared with the rigid blade; however, with the increase of angle of attack higher lift and drag coefficients are observed for the membrane blade. Table 7.5 provides a quantitative comparison of the change in these coefficients compared with the rigid blade. The cross section of the membrane blade in the absence of aerodynamic load was shown in Fig. 7.5 (the red curve). The membrane blade has a pretty much symmetric profile in the unloaded state. For $\alpha = 0.0°$, the converged cross

section is also a rather symmetric profile (Fig. 7.10). This explains the big decrease in the lift coefficient of the membrane blade at $\alpha = 0.0°$, compared with the rigid blade with the asymmetric S809 airfoil. With the increase of angle of attack, the loading on the blade, and as a consequence the converged cross section profile, becomes more and more asymmetric which can be seen in Fig. 7.10. Moreover, the displacement in the membranes increases with the increase of the angle of attack. It increases the camber of the blade profile and as a consequence, there is an improvement in the lift coefficient of the membrane blade compared with the rigid blade for higher angles of attack. The drag coefficient increases as well with the increase of angle of attack and the drag coefficient of the membrane blade is higher than that of the rigid blade. But the improvement in the lift coefficient is larger compared with the increase of the drag coefficient and consequently for $\alpha = 4.0°$ and higher angles of attack the lift to drag ratio for the membrane blade is higher compared with the baseline rigid blade. While having a higher lift coefficient and lift to drag ratio is not desired for stall controlled turbine like the NASA-Ames Phase VI rotor, it should be mentioned that the purpose of the analysis is to investigate the characteristics of the membrane blade concept and make a comparison between the membrane blade and a conventional blade. No conclusion could be made at this stage, whether the concept should be utilized for pitch-controlled or stall-controlled turbines.

Table 7.5: Percentage change in aerodynamic characteristics of the membrane blade compared with the rigid blade

$\alpha(deg)$	0.0	2.0	4.0	6.0	7.5	9.0
Δc_L	-75.5	-12.5	7.5	15.0	17.7	13.9
Δc_D	-4.2	-5.3	-1.4	3.4	5.9	2.9
$\Delta(L/D)$	-74.5	-7.5	9.1	11.2	11.1	10.7

The cross section of the membrane blade varies along the span. Membrane deformation changes cross section properties of the blade like the maximum camber and thickness. The original S809 airfoil has a maximum camber of about 1% at 82.3% chord position, but for the membrane blade maximum camber and its location change with the angle of attack (Table 7.6). It is also shown in Fig. 7.12 that with the increase of angle of attack the maximum camber increases as well and in general the point of maximum camber moves towards the leading edge of the blade.

The increase in the lift coefficient of the membrane blade could also be seen in

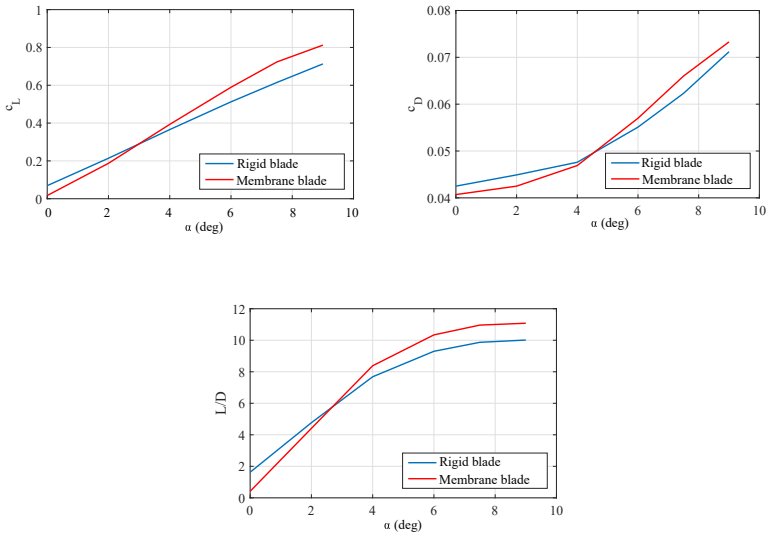

Figure 7.11: Comparison between the aerodynamic characteristics of the membrane blade and the rigid blade

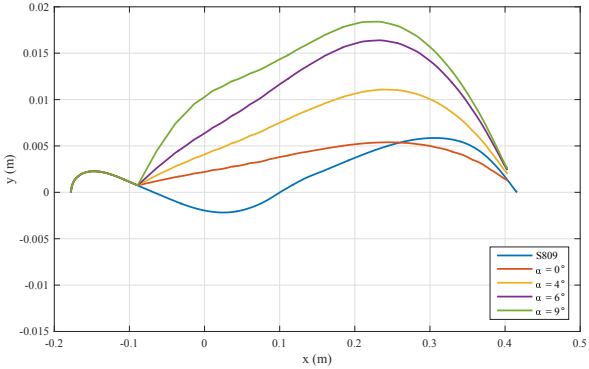

Figure 7.12: Comparison of the camber line at the middle span section of the second segment.

the pressure coefficient distribution over blade's surface. The pressure coefficient distribution over the middle span section of segment 2 is plotted in Fig.

Table 7.6: Maximum camber and its location for the middle span section of the second segment from the root

$\alpha(deg)$	0.0	2.0	4.0	6.0	7.5	9.0
Maximum Camber %	0.34	0.93	1.91	2.82	3.29	3.17
Location of maximum camber	71.48	73.53	73.51	71.45	69.40	69.40

7.13 and is compared with pressure coefficient distribution of the rigid blade for $\alpha = 6.0°$. The kink in the c_p distribution is due to slope discontinuity at the point where the lower membrane is attached to the rigid leading edge mast.

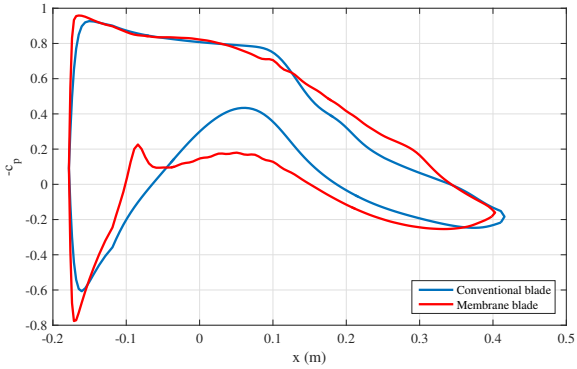

Figure 7.13: Pressure coefficient distribution over the middle span section of the second segment.

To sum up, comparing the performance of the membrane blade with its representative rigid counterpart the following main observations are made:

1. A higher lift curve slope for the membrane blade is observed. Even though at zero angle of attack the membrane blade has a smaller lift coefficient than the rigid blade, due to the higher slope of the lift curve, the membrane blade shows higher lift coefficient compared with the rigid blade for higher angles of attack.

2. With the increase of angle of attack the lift to drag ratio of the membrane blade becomes higher than that of the rigid blade.

3. The maximum camber and its location for a membrane blade depends on the angle of attack. The maximum camber of the membrane blade is

higher than the rigid blade. With the increase of angle of attack, there is a slight shift of the point of maximum camber toward the leading edge.

7.2.2 Transient FSI analysis

This section presents the transient FSI analysis of the membrane blade with the same structural properties and pre-streeses as in section 7.2.1.

For solving the fluid problem pimpleDyMFoam solver is used with slight modification for managing the data exchange between the fluid and the structural solver. The computational domain together with its discretization near the blade is presented in Fig. 7.7. As in the steady FSI simulations, the simulations are done for a uniform far-field velocity of $30\,m/s$ and up to an angle of attack of $\alpha = 15.0^\circ$ is simulated. Until $\alpha = 11.0^\circ$, the same mesh as in the steady state simulations has been used, but for $\alpha = 13.0^\circ$ and $\alpha = 15.0^\circ$ a finer mesh consisting of about 4.4 million elements has been used. The refinement has been mainly made near the blade and in the wake region.

The coupled problem of the interaction between membrane deformation and external fluid flow is solved for a total of 6 seconds with a time step size of 0.001 seconds. In order to improve the stability, the calculated displacement at each iteration is relaxed by a factor (ω_r) between 0.1 and 0.3 (depending on the angle of attack) before being sent to the fluid solver (Eqn. 7.1).

Blade profile comparison

As a result of the applied aerodynamic load, the membrane on the upper side of the blade moves upward and on the lower side, depending on the angle of attack, the membrane moves either downward or upward. Blade's cross section at the ribs remains unchanged (S809 profile), but apart from the 5 ribs, the cross section changes along the blade. Comparison of the mean cross section profile with the undeformed cross section and the S809 profile is made in Fig. 7.14 for the mid-span section of segment 2. There are small oscillations in the membranes up to $\alpha = 11.0^\circ$ (Fig. 7.15). Since the amplitude of these oscillations is small, the time-averaged profiles are represented in Fig. 7.14. Due to the unsteadiness of membrane's vibration at $\alpha = 11.0^\circ$ $\alpha = 13.0^\circ$ and $\alpha = 15.0^\circ$ and due to wave-type oscillations in the membranes, no time-averaged profile is shown for these angles of attack.

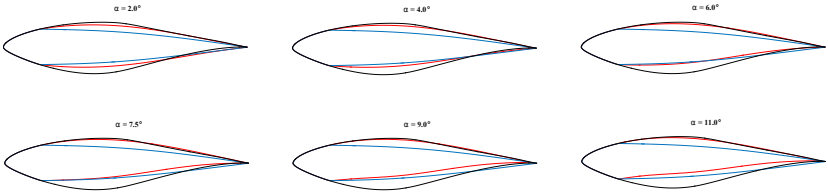

Figure 7.14: Blade's cross section comparison: S809 profile (black), undeformed profile (blue) and deformed profile (red).

Displacement over Time

Displacement of the membrane at a selected monitor point on the upper membrane which is located at $x/c = 0.5$ position on the mid-span cross section of segment 2 is plotted in Fig. 7.15. For the seven studied angles of attack oscillations in the membrane are damped out with time for all except $\alpha = 11.0°$. For this case, displacement at the monitor point oscillates around a mean value of $0.0181\,m$ with a standard deviation of 2.54×10^{-5}. As it can be seen in the figure, for $\alpha = 0.0°$ to $\alpha = 9.0°$, displacement is increasing with angle of attack but for $\alpha = 9.0°$ and $\alpha = 11.0°$ there is a decrease in the displacement. Taking the acting forces on the blade into account, it is not the lift force which correlates with the displacement of the membrane, but a correlation exists between the displacement of the monitor point and the lift to drag ratio (Fig. 7.16).

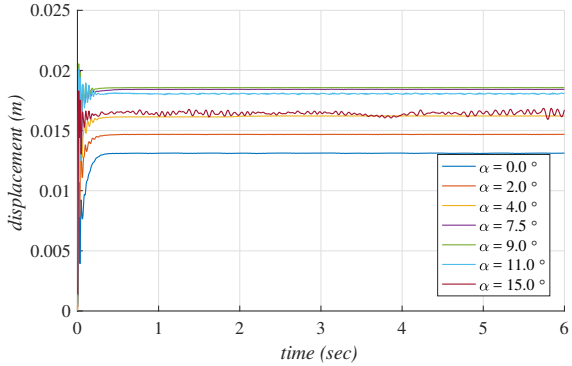

Figure 7.15: Membrane displacement at the monitor point

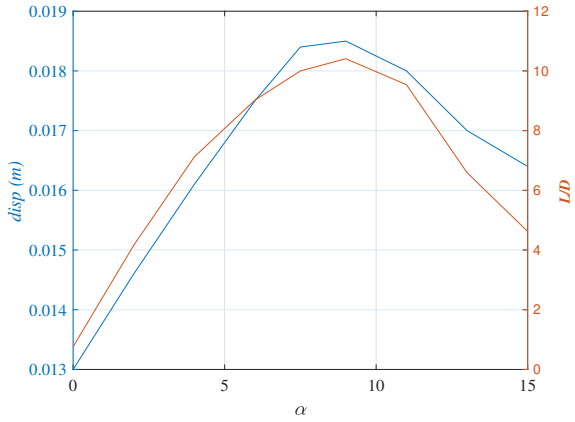

Figure 7.16: Correlation between membrane displacement and L/D

Camber Line

As a result of membrane's deflection, blade's camber changes. As previously mentioned, the S809 airfoil has a maximum camber of about 1% located at 82.3% chord position. Under the action of the applied aerodynamic load, the maximum camber increases with the angle of attack. As shown in Fig. 7.17 and as seen in the steady-state analysis, the point of maximum camber shifts toward the leading edge. Starting from $\alpha = 4.0°$ the membrane blade has higher camber compared with the baseline blade.

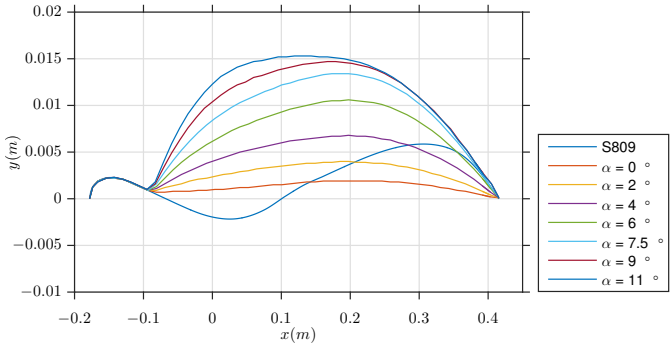

Figure 7.17: Camber line at the mid-span section for the second segment form blade's root.

Table 7.7: Maximum camber and its location for the membrane blade

$\alpha(deg)$	0.0	2.0	4.0	6.0	7.5	9.0	11.0
Max Camber (%)	0.38	0.67	1.14	1.78	2.26	2.52	2.63
Location of Max Camber	65.2	63.2	63.2	63.2	61.2	60.0	52.0

Aerodynamic Coefficients

Because of vortex shedding at the cylindrical part of the blade, flow separation at higher angles of attack ($\alpha = 9.0°$ and $\alpha = 11.0°$) and slight oscillations in the membrane, the force acting on the membrane blade has also an oscillatory behavior (Fig. 7.18). Spectral analysis of the lift coefficient is shown in Fig. 7.19, the two dominant frequencies correspond to vortex shedding at the root section of the blade and flow separation over the blade.

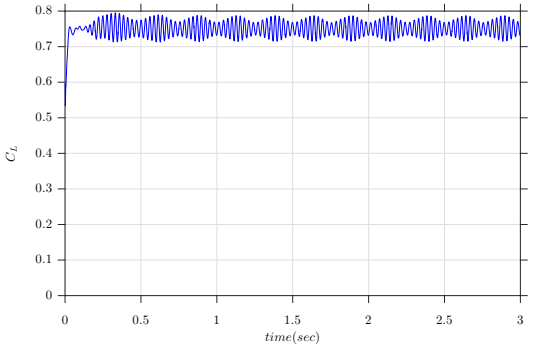

Figure 7.18: Lift coefficient for the membrane blade, $\alpha = 9.0°$.

Membrane vibrations change the spectral response of the loading on the blade which is of utmost importance in fatigue analysis of the blade. The comparison of the spectra of the lift coefficient between the membrane blade and the baseline blade is shown in Fig. 7.20. There is a shift toward the right for the dominant frequency of the membrane wing. Furthermore, the amplitude of the oscillation in the lift coefficient at the dominant frequencies is less for the membrane blade, which can be an advantage over the rigid blade regarding fatigue lifetime of the blade.

Comparison of the lift coefficient, drag coefficient and the lift to drag ratio between the membrane blade and its rigid counterpart is made in Fig. 7.21. As

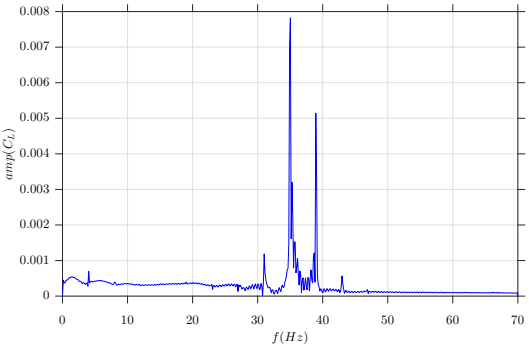

Figure 7.19: Spectral analysis of the lift coefficient, $\alpha = 9.0°$.

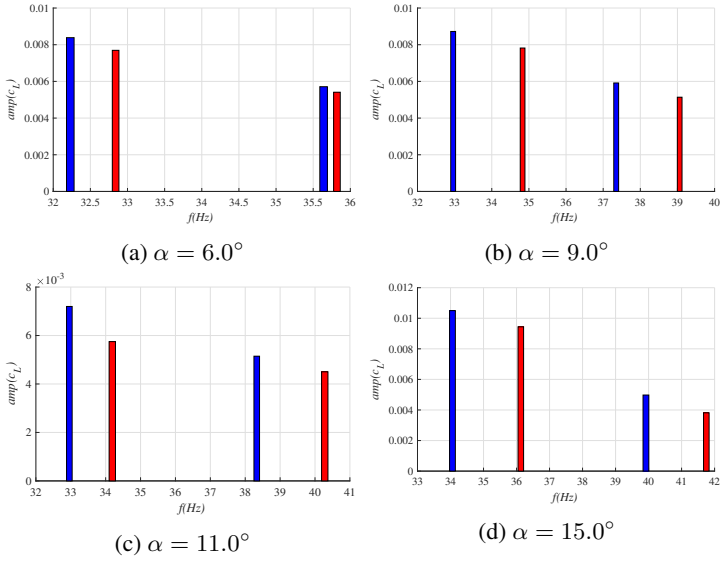

(a) $\alpha = 6.0°$ (b) $\alpha = 9.0°$

(c) $\alpha = 11.0°$ (d) $\alpha = 15.0°$

Figure 7.20: Change of the dominant frequencies for the membrane blade compared with the rigid blade.

in the steady-state analysis, for $\alpha = 0.0°$ the membrane blade has a smaller lift coefficient compared with the rigid blade, but with the increase of angle of attack the camber, and consequently the lift coefficient increases for the membrane blade. Even though the zero angle of attack lift coefficient is smaller for the membrane blade, the slope of the lift curve is higher for the membrane

blade and starting from $\alpha \approx 4.5°$ the lift coefficient is higher for the membrane blade.

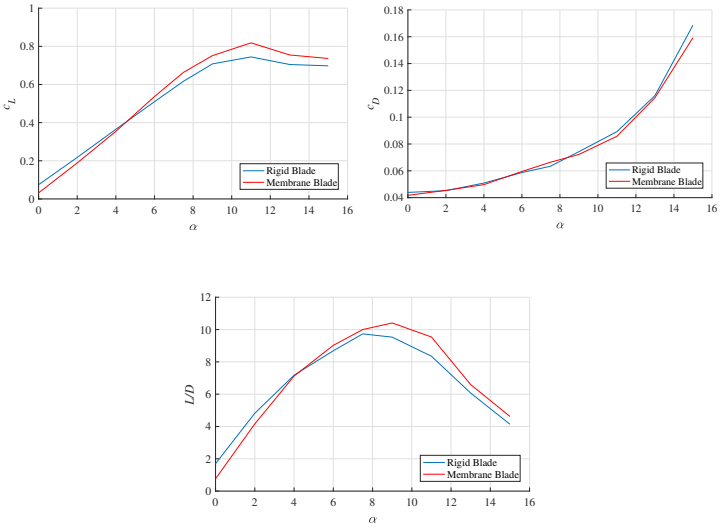

Figure 7.21: Comparison between the aerodynamic characteristics of the membrane blade and rigid blade

Pressure Distribution Comparison

Improvement of the lift coefficient for the membrane blade over the rigid baseline blade can also be seen in the pressure distribution over the blade. The comparison is made in Fig. 7.22 for the pressure coefficient at the mid-span section of segment 2. The kink in the pressure coefficient distribution for the membrane blade is due to discontinuity in surface slope at the point where the membrane is attached to the rigid leading edge.

In summary, the lift coefficient at zero angle of attack is smaller for the membrane blade, but due to the higher lift curve slope the membrane blade demonstrates higher lift coefficient and lift to drag ratio for higher angles of attack compared with the rigid blade. An increase of camber with the angle of attack and also shifting of the point of maximum angle toward the leading edge is observed for the membrane blade. The maximum lift to drag ratio is also larger for the membrane blade. These results together with the lighter construction of the membrane blade promise the potential of this concept for wind turbines.

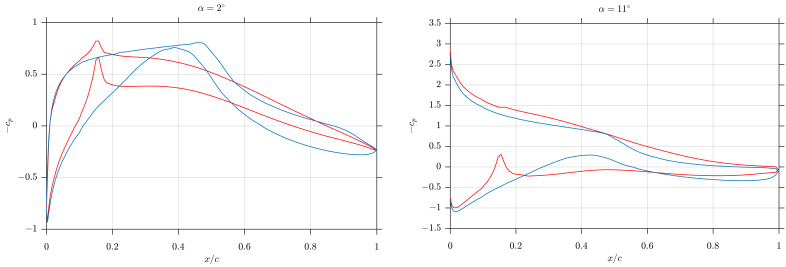

Figure 7.22: Pressure distribution comparison, rigid blade (blue), membrane blade (red)

7.3 BEM for Analysis of the Membrane Blade

As already discussed in chapter 2, the blade element momentum (BEM) method is the most common approach for calculating aerodynamic loads on a wind turbine and analyzing its aerodynamic performance [21]. The method is very fast and provides good results if accurate lift and drag coefficient data as a function of the angle of attack are available. The classical BEM method cannot be applied to the membrane blade because the actual shape of blades's cross section is not known in advance for a specific operating condition of the turbine (wind speed, rotational speed and pitch angle). Consequently, lift and drag coefficients for the 2D sections of the blade cannot be read from look-up tables.

This section introduces the coupled panel-BEM approach for analyzing the membrane blade via FSI. The proposed method uses the three-dimensional panel code solver (Section 3.2) for calculating the pressure distribution over the surface of the blade in order to estimate the aerodynamic loading for calculating the shape of the blade, combined with the two-dimensional panel method solver (Section 3.1) for polar calculations of the 2D blade sections. The 2D vortex panel method replaces the look-up tables for the lift and drag coefficients and calculates these coefficients on the run during the FSI iterations.

7.3.1 Steady-State FSI Analysis via Panel-BEM Coupling

A typical FSI analysis using the staggered approach consists of a fluid solver and a structural solver with the two solvers exchanging information at the fluid-solid interface. Evaluating the aerodynamic performance of the membrane blade via BEM-Panel coupling in a fluid-structure interaction workflow

requires two levels of coupling and hence two levels of communication. First of all, the structural solver needs to communicate with the fluid solver in order to exchange loading and displacement data. Secondly, on the fluid side, the vortex panel solver needs to receive the induced velocities from the BEM solver at each iteration in order to update the relative velocity at each blade section.

During the explicit coupling iteration these steps are performed for each iteration in the following order:

1. The BEM solver calculates the induced velocities for all radial blade sections and sends them to the 3D panel solver.

2. The panel solver updates the relative velocity by taking the induced velocities into account and solves the fluid problem. The resulting forces are then sent to the structural solver.

3. The structural solver calculates the displacements and sends them to the BEM solver, the 2D panel solver and the 3D panel solver.

The above-mentioned steps are taken for each iteration until convergence is reached. For the iterative solution of the BEM a relative tolerance of 10^-6 for the convergence of the axial and tangential induction factors is used. The same tolerance is also used for the convergence of the coupling iterations between the fluid solver and the structural solver. The schematic representation of a single coupling iteration is shown in Fig. 7.23. The individual blocks are explained in more detail in the following sections.

7.3.1.1 BEM Solver

The solution procedure for the classical BEM method is presented in Section 2.3.3. In order to utilize the BEM method for analysis of the membrane blade, the look-up tables for lift and drag coefficients should be substituted by some tool which receives the actual 2D profile of the blade at different radial sections and calculates the lift and drag coefficients on the run.

For this purpose, the 2D panel code solver, presented in section 3.1, is integrated into the BEM solution procedure. The iterative solution algorithm for the BEM method coupled with the 2D panel solver is summarized in Algorithm 5. The output of the BEM solver are the induced velocities which are sent to

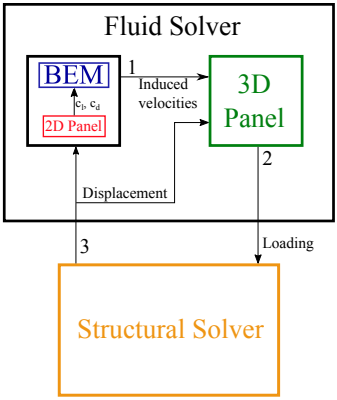

Figure 7.23: Realization of FSI coupling: sequence of data transfer between the solvers.

the 3D panel solver in order to update the relative velocity before calculating the pressure distribution over the blade.

for *each element* **do**
  initialize a and a';
  while *convergence* = *false* **do**
    calculate the relative flow angle (eqn. 2.28);
    calculate angle of attack (eqn. 2.29);
    `// 2D Panel method`
    2D profile discretization;
    calculate panel properties;
    calculate the influence coefficients;
    calculate the RHS;
    solve for vortex strength;
    calculate pressure distribution;
    calculate C_l and C_d;
    calculate C_n and C_t (eqn. 2.31);
    calculate a and a' (eqns. 2.40 and 2.41);
    check convergence;
  end
  do the post-processing;
end

Algorithm 5: The iterative BEM solution for the membrane blade.

7.3.1.2 3D Panel Solver

Both, the geometry of the blade and the velocity seen by the blade, should be updated at each iteration. The geometry update is made after receiving the new displacement field from the structural solver. The velocity at rotating blade consists of three components. They are: wind velocity, rotational velocity and the induced velocity:

$$\mathbf{u}_{rel} = \mathbf{U}_0 + \mathbf{U}_{rot} + \mathbf{W} \tag{7.2}$$

These components are shown in Fig. 7.24. The 3D panel solver receives the induced velocities, calculated by the BEM solver, and updates the total velocity vector before solving the problem for the new coupling iteration.

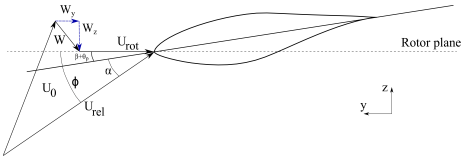

Figure 7.24: Components of the total velocity vector.

7.3.1.3 Structural Solver

In the last step of each coupling iteration, the structural finite element solver (CARAT++) receives the loading from the fluid solver and calculates the displacement. The calculated displacement is sent back to the fluid solver. The Fluid mesh is updated by applying the received displacement to the mesh nodes. Mortar mapping is used for interpolating the data at the non-matching FSI interface.

The overall algorithm for performing the steady-state FSI analysis of the membrane blade via Panel-BEM coupling is presented in algorithm 6. The color coding in the algorithm follows that of Fig. 7.23. The proposed workflow is verified by testing it for the NASA-Ames Phase VI wind turbine, which is used as the baseline rigid blade. The obtained pressure distribution at the radial position of $\frac{r}{R} = 0.8$ for a wing velocity of $U = 7\,m/s$ and a pitch angle of $\theta_p = 3^\circ$ is presented in Fig. 7.25. The comparison is made with the numerical and experimental results in [39].

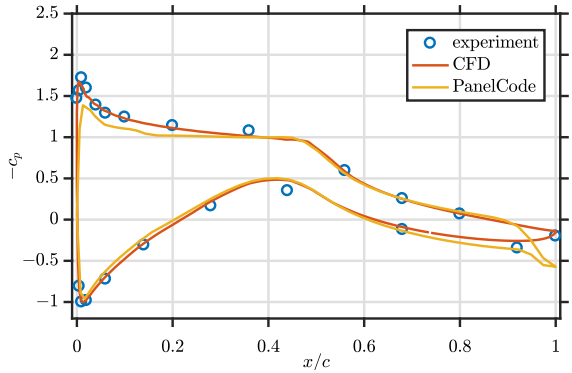

Figure 7.25: Comparison of the pressure distribution obtained using the proposed work flow with numerical and experimental data.

7.3.1.4 results

FSI analysis of a membrane blade via Panel-BEM coupling is presented in this section for a specific membrane blade based on the NASA-Ames Phase VI turbine. The finite element model of the blade (consisting of the 5 parts is shown in Fig. 7.2) is shown in Fig. 7.26.

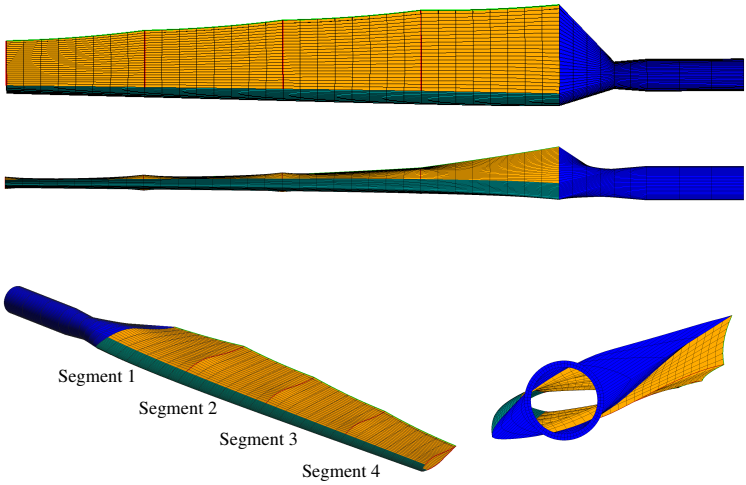

Figure 7.26: The finite element model of the membrane blade.

```
while convergence = false do
    for each coupling iteration do
        update the fluid mesh;
        for each radial element do
            initialize a and a′;
            while BEMconvergence = false do
                calculate the relative flow angle (eqn. 2.28);
                calculate angle of attack (eqn. 2.29);

                // 2D Panel method
                2D profile discretization;
                calculate panel properties;
                calculate the influence coefficients;
                calculate the RHS (eqn. 3.19);
                solve for vortex strength;
                calculate pressure (eqn. 3.21);
                calculate C_l and C_d;

                calculate C_n and C_t (eqn. 2.31);
                calculate a and a′ (eqns. 2.40 and 2.41);
                check BEMconvergence;
            end
        end
        write BEM output;
        calculate panel properties; // 3D panels
        update the local velocity (eqn. 7.2);
        calculate 3D influence coefficients;
        calculate the RHS;
        solve for vortex strength;
        calculate pressure;
        send force;
        write output;
        receive force;
        calculate displacement;
        send displacement;
    end
    check convergence;
end
```

Algorithm 6: The iterative BEM solution for the membrane blade.

Blade's root, as well as its leading edge, are assumed to be rigid. Upper and

lower surface of the blade are modeled using membrane elements, the ribs are modeled as beams and the pre-stressed edge cables are modeled as trusses. Their properties are summarized in table 7.1.

The membrane's pre-stress is set individually for the upper and lower membranes of the four segments of the membrane blade. Since the rotational velocity, and consequently the loading, increases towards the tip of the blade, higher pre-stress should be applied to the to the outer segments of the blade. This scaling is made via the local scaling factor (S_l). In addition to the scaling with respect to the local rotational velocity, the variation of membrane dimensions should also be reflected in assigning the pre-stresses. This is taken care of by introducing a geometrical scaling factor for the pre-stresses (S_g). The four segments of the blade have similar span length, but their chord length decreases towards the tip. As a result, the pre-stresses in chordwise direction should decrease towards the tip of the blade. The goal of introducing the scaling factors for the pre-stress distribution at different blade segments is to minimize the difference in membrane deflection at different sections and to ensure sufficient flexibility of the membranes. After deciding for a reference pre-stress state in the membranes and the edge cables, these reference pre-stresses are scaled with a geometrical scaling factor (S_g) and a local scaling factor (S_l) and assigned to the corresponding structural parts:

$$\sigma_{c,i} = \sigma_{c,0} \times S_{l,i} \times S_{g,i} \tag{7.3}$$

$$\sigma_{s,i} = \sigma_{s,0} \times S_{l,i} \tag{7.4}$$

$$\sigma_{cable,i} = \sigma_{cable,0} \times S_{l,i} \times S_{g,i} \tag{7.5}$$

Where σ_c and σ_s are respectively membrane's pre-stress in chordwise and spanwise direction and σ_{cable} is the pre-stress in the edge cable.

In order to study the pre-stress dependent performance of membrane blade, three sets of pre-stresses are examined. These pre-stresses are summarized in Table 7.8. The superscripts u and l are used respectively for pre-stresses of the upper and lower membranes. Compared with the S1 pre-stresses, in pre-stress set S2 the pre-stress in spanwise direction is doubled for the lower membranes. In the S3 pre-stress set all the pre-stresses are reduced by about 33% compared with S1. Deflection of the membrane at the suction side of the blade for the S3 pre-stress set is shown in Fig. 7.27. For each segment, the maximum displacement occurs at the middle of the segment.

Table 7.8: Pre-stress sets and the scaling factors according to Eqns. 7.3 and 7.4.

	S1	S2	S3
$\sigma^u_{c,0}(kPa)$	25	25	16.6
$\sigma^u_{s,0}(kPa)$	67	67	44.6
$\sigma^l_{c,0}(kPa)$	25	25	16.6
$\sigma^l_{s,0}(kPa)$	67	134	44.6
$\sigma_{cable,0}(kPa)$	4160	4160	4160
$S_{l,1}$	2.2	2.2	2.2
$S_{g,1}$	1.0	1.0	1.0
$S_{l,2}$	2.4	2.4	2.4
$S_{g,2}$	0.86	0.86	0.86
$S_{l,3}$	4.6	4.6	4.6
$S_{g,3}$	0.72	0.72	0.72
$S_{l,4}$	6.0	6.0	6.0
$S_{g,4}$	0.59	0.59	0.59

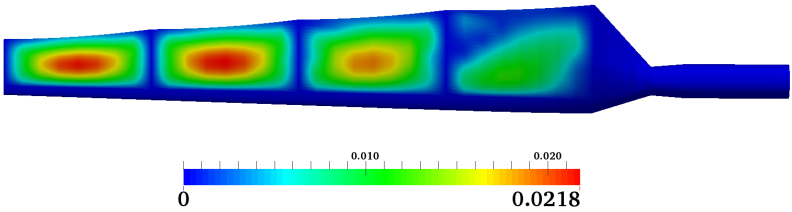

Figure 7.27: Displacement (m) distribution for the suction side of the blade for the S3 pre-stress set. ($U = 8\,m/s$, $\theta_p = 5°$)

Comparison of the power produced by the membrane blade with the baseline blade is made in Fig. 7.28. The generated power for the rigid blade is also calculated using lift and drag coefficients calculated by the 2D panel code. It should be kept in mind that the method over-predicts the power because viscous effects are neglected in the panel method, but the over-prediction is happening for both the rigid blade and the membrane blade. The percentage change in the power compared to the rigid blade is reported in Table 7.9. With the increase of membrane's deflection for higher wind speed, the power generated by the membrane blade exceeds that of the rigid blade. The S3 pre-stress set provides the highest improvement among the three examined pre-stress levels. This is

due to higher flexibility of the membrane blade for the S3 pre-stress set, which results in higher deflection of the membranes and consequently higher camber, which will be examined in more detail in the following sections.

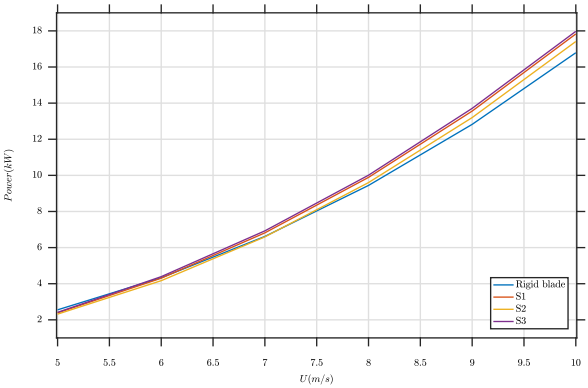

Figure 7.28: Power comparison: membrane blade vs rigid blade.

Table 7.9: Percentage change in power compared with the rigid blade.

Wind speed (m/s)	5.0	6.0	7.0	8.0	9.0	10.0
S1	-6.7	-0.5	3.0	4.7	5.7	6.2
S2	-9.3	-3.8	-0.4	1.6	2.9	3.7
S3	-5.5	1.4	4.6	6.0	6.9	7.1

Comparison of the Deformed Shapes

The cross section of the membrane blade at the middle of the third segment is presented in Fig. 7.29. The figure shows the results of the S3 pre-stress set for different wind velocities (U). Both deformed and undeformed cross sections are presented. For lower wind velocities there are suction regions on both sides of the blade and parts of the lower membrane move downward, causing the profile thickness to increase. But as the wind speed increases, above $8\,m/s$ in this case, only positive pressure is observed at the side of the blade which faces the wind. With the upward movement of the lower membrane, the profile thickness decreases and at the same time the camber increases. Comparison of the change in camber is made in the next section.

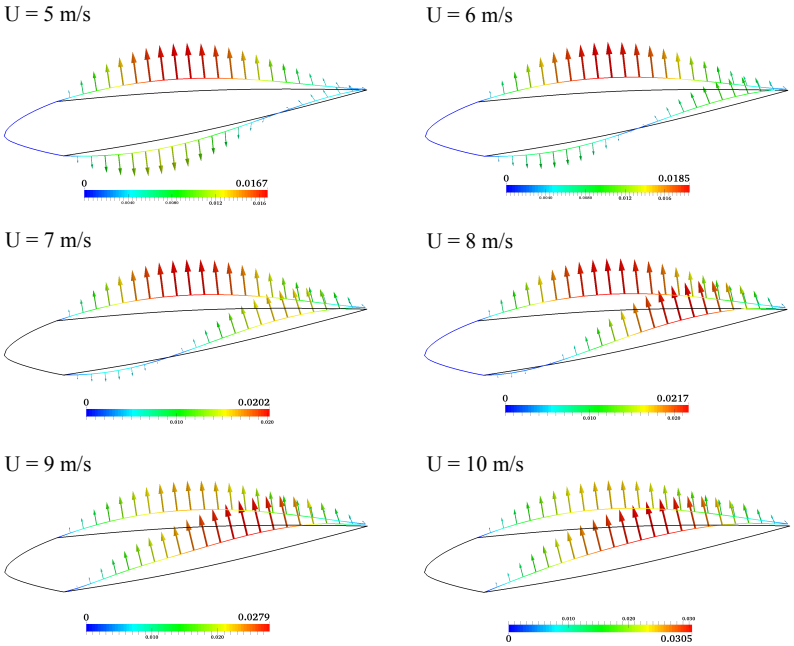

Figure 7.29: Profile comparison at the middle of the third segment (S3 pre-stress set). The arrows and the legends correspond to the displacement (m).

Camber Comparison

The cross section and consequently the camber line changes for the membrane blade along the span. Fig. 7.30 shows the camber line for the middle section of the third segment. The camber line is plotted for the converged profile and is compared with that of the baseline conventional rigid blade, i.e. the S809 airfoil. The change in the horizontal position of the trailing edge by the increase of wind speed from $5\,m/s$ to $10\,m/s$ is about 0.1% and is hardly visible in the figure. For the same velocity increase, the vertical displacement of the trailing edge increases by a factor of 2.7. The maximum camber increases with the increase of wind speed. The point of maximum camber is as well shifted towards the leading edge. For the S809 airfoil the maximum camber is about 1% and its location is at $x/c = 0.823$. For the membrane blade at the middle section of the third segment, the maximum camber and its location are

Table 7.10: Maximum camber and its location for the middle section of the third segment. (S3 pre-stress set.)

Wind speed (m/s)	5.0	6.0	7.0	8.0	9.0	10.0
Maximum camber %	1.22	2.31	3.33	4.23	5.12	5.60
Location of maximum camber ($\frac{x}{c} \times 100$)*	73.6	70.7	66.7	63.7	60.7	55.9

summarized in Table 7.10.

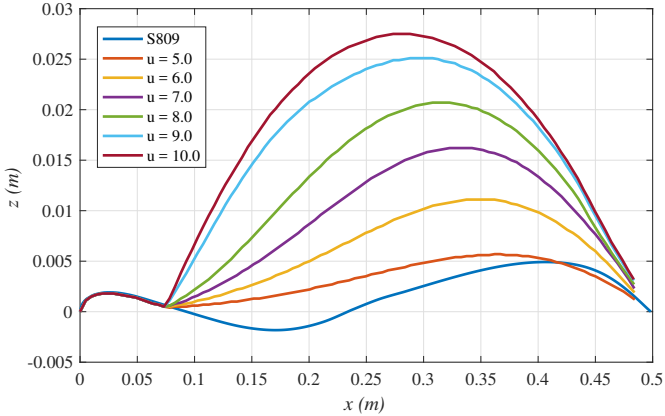

Figure 7.30: Camber line comparison at the middle of the third segment. (S3 pre-stress set)

Comparison of the Angle of Attack

In this section, the local angle of attack along the blade for the flexible membrane blade is compared with the baseline rigid blade. The variation of the angle of attack (and chord length) with the deflection of the trailing edge (Fig. 7.31) is taken into account in calculating the effective angle of attack and chord length for the membrane blade.

The comparison is depicted in Fig. 7.32 for the wind speed of $U = 8\,m/s$ at the pitch angle of $\theta_p = 5°$. The vertical lines show the position of the ribs. The maximum local angle of attack along the blade is about $10.2°$. Apart from

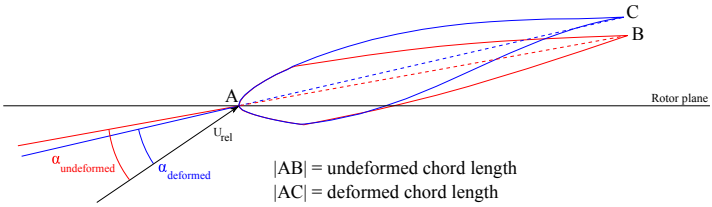

Figure 7.31: Change of the angle of attack and chord length as a result of trailing edge's deflection.

a portion of the first segment, for the other segments the membrane blade the local angle of attack for the membrane blade is smaller than the stall angle of attack for the S809 airfoil. Therefore, for this operating condition of the turbine the results from panel method are valid .

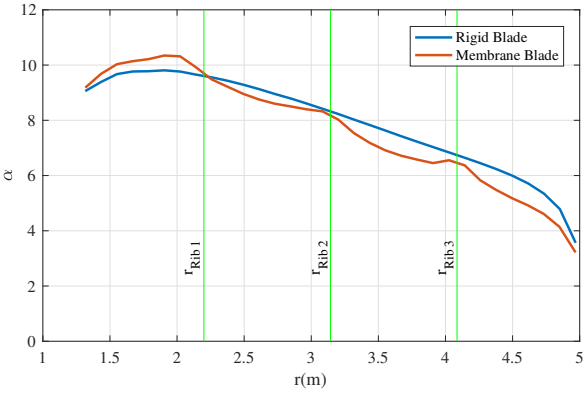

Figure 7.32: Comparison of the local angle of attack between the membrane blade and the baseline rigid blade for the S3 pre-stress set. ($U = 8\,m/s$, $\theta_p = 5°$)

Apart from the first segment, for the other segments the membrane blade has a smaller local angle of attack compared to the rigid blade. Despite lower local angle of attack along most parts of the blade for the membrane blade compared with the rigid blade, the generated power by the membrane blade is higher. This should be attributed to the change in blade's cross section and the increase of camber in the membrane blade. This is also reflected in the distribution of the lift coefficient along the blade which is shown in Fig. 7.33. Since for each blade segment the maximum deflection of the membrane occurs at the middle

of the segment, the camber of the blade's profile has a local maximum in the middle of each segment. Consequently there exists a local maximum for the lift coefficient at the middle of each segment as well. At the first segment the lift coefficient is smaller for the membrane blade (which is discussed in the next section), but at the other three segments, the membrane blade has higher lift coefficient. Base on the Betz theory, for an ideal rotor and with neglecting the drag force and wake rotation the optimum energy extraction from the wind occurs at an axial induction factor of $\frac{1}{3}$. For the three outer segments of the blade, the axial induction factor of the membrane blade is higher than the rigid baseline blade (Fig. 7.34). Overall, the axial induction factor along the blade is nearer to the optimum axial induction factor for the membrane blade.

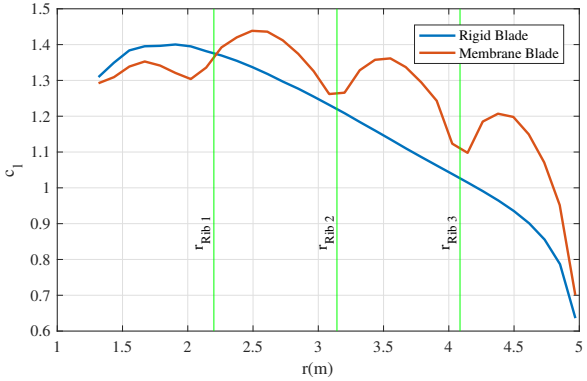

Figure 7.33: Comparison of the 2D lift coefficient between the membrane blade and the baseline rigid blade for the S3 pre-stress set. ($U = 8\,m/s$, $\theta_p = 5°$)

Pressure distribution comparison

In order to investigate the difference between the lift coefficient of the membrane blade and the rigid blade for the operating condition presented in the previous section, first the converged blade cross section is compared with the rigid blade's airfoil profile (S809 airfoil). This comparison is made in Fig. 7.35. Both the thickness and the camber of the airfoil increase toward the tip (segment 4).

The higher lift coefficient at segments 2 to 4 and lower lift coefficient at the first segment of the membrane blade compared with the rigid blade can be explained

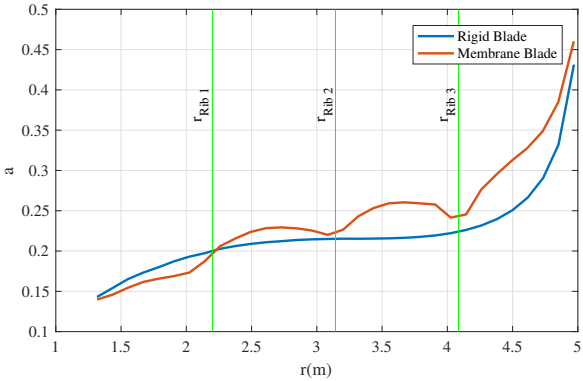

Figure 7.34: Comparison of the axial induction factor between the membrane blade and the baseline rigid blade for the S3 pre-stress set. ($U = 8\,m/s$, $\theta_p = 5^\circ$)

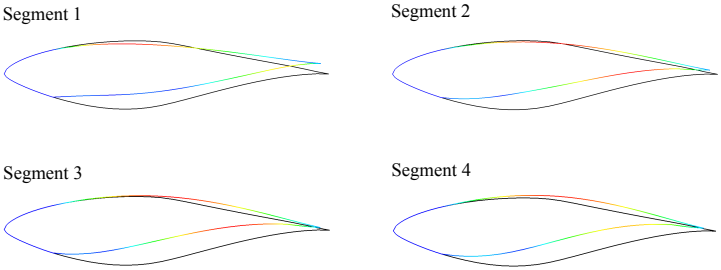

Figure 7.35: Comparison of membrane blade's cross section and the rigid blade cross section (black) at the middle of the 4 segments.(S3 Pre-stress set, $U = 8\,m/s$, $\theta_p = 5^\circ$)

by the pressure distribution over the membrane blade and its comparison with the baseline rigid blade. Fig. 7.36 shows the distribution of the pressure coefficient at the middle of the four blade segments. The area enclosed by the curve measures the lift coefficient. As it can be seen, for the first segment the pressure difference between the suction and the pressure side is higher for the rigid blade and as a result, the rigid blade demonstrates a higher lift coefficient at the first segment. With the increase in profile's camber the pressure difference between the suction side and the pressure side of the membrane blade increases

and the area enclosed by the c_p curve of the membrane blade gets larger than that of the rigid blade.

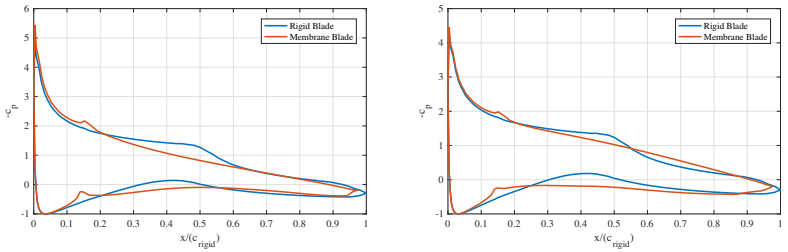

(a) Segment 1

(b) Segment 2

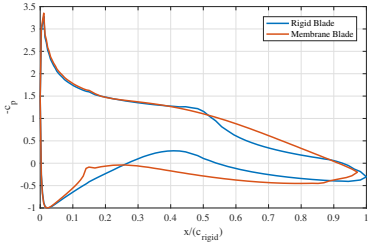

(c) Segment 3

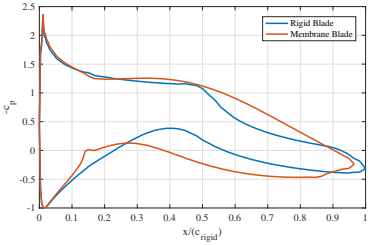

(d) Segment 4

Figure 7.36: Pressure coefficient distribution comparison between the membrane blade and the rigid blade for the S3 pre-stress set. ($U = 8\,m/s, \theta_p = 5°$)

Tangential force comparison

The tangential force (p_T) is the force component whose work generates power in a wind turbine. As reported in Table 7.9, depending on the wind speed, the power generated by the membrane blade is higher than the rigid blade. This holds apart from the wind speed of $U = 5\,m/s$, which is also reflected in the distribution of the tangential force along the blade, presented in Fig. 7.37 for the S3 pre-stress set. For $U = 5\,m/s$ the tangential force is lower for the membrane blade at each of the four segments. For $U = 8\,m/s$ and $U = 10\,m/s$, the membrane blade has lower tangential force at segment 1, but a higher tangential force at the 3 other segments and overall higher power. However, the distribution of the tangential force for the membrane blade is not as smooth as for the rigid blade which is due to the variation of the blade's profile in the radial direction.

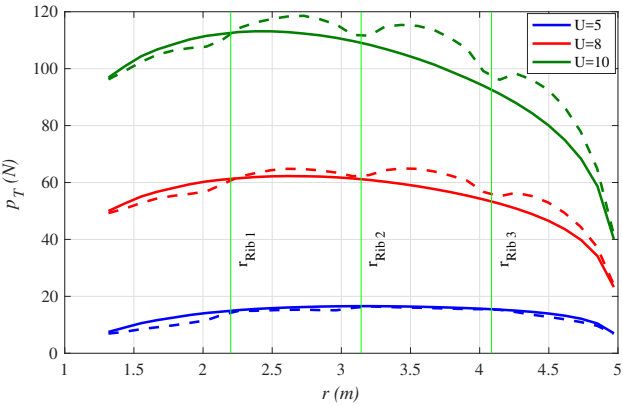

Figure 7.37: Comparison of tangential force distribution between the rigid blade (full line) and the membrane blade (dashed line). (S3 Pre-stress set, $\theta_p = 5°$)

7.3.2 Transient FSI Analysis via Panel-BEM Coupling

The methodology presented in section 7.3.1 can also be applied for performing unsteady FSI analysis of the membrane blade. For the transient FSI analysis, instead of the steady state BEM solver and panel code, the corresponding unsteady versions presented respectively in sections 2.5 and 3.3 are used together with a dynamic analysis solver for the structure side.

Unsteady FSI analysis of the same membrane blade configuration as in section 7.3.1 with the same structural properties (Table 7.1) is presented in this section. The coupled problem of the interaction between the rotating membrane blade and wind is simulated for 10 seconds with a time step size of $\Delta t = 0.01s$ and for the wind speed range of $5 - 10\,m/s$. The analysis is performed for the S3 pre-stress set (Table 7.8). On the structural side, the Newmark-Beta method is used for the time integration and structural damping is modeled via Rayleigh damping. The transient response of the membrane to the uniform wind as well as to the mean atmospheric wind profile (including wind shear) is analyzed.

7.3.2.1 Uniform Wind

Unsteady FSI analysis of the membrane blade is presented in this section. The aeroelastic behavior of the blade in the case of steady uniform wind can be

used as a benchmark to verify the presented unsteady FSI workflow utilizing the unsteady BEM solver and the unsteady vortex panel method. If there exists a steady state solution, the result of the unsteady FSI analysis should converge the steady state solution (already covered in section 7.3.1) or should oscillate around the steady state solution in the case of a transient response.

Under the applied aerodynamic load the membrane starts to deform. For all of the studied wind speeds, the membrane experiences an initial overshoot and starts oscillating around a constant mean after about 2 seconds which corresponds to approximately 2.5 revolutions of the blade. Fig. 7.38 shows the membrane displacement at the middle of the suction side of the blade in segment 3 (Fig. 7.26). The amplitude of the oscillations is very small, with the maximum amplitude for the 6 studied wind speeds being about 0.2% of the mean displacement.

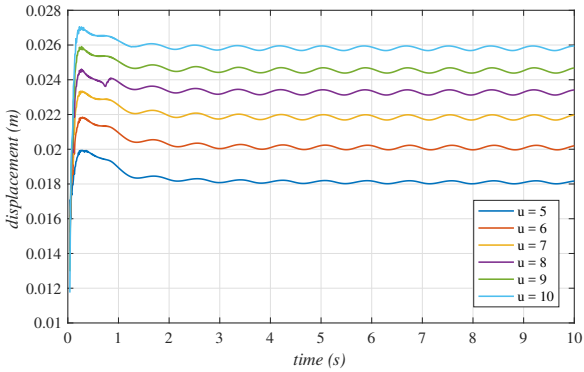

Figure 7.38: Membrane displacement at the selected monitor point, $\theta_p = 5°$.

These small oscillations of the membrane surface cause fluctuations in the generated power. This is plotted in Fig. 7.39 for the wind speed of $U = 8\,m/s$. Similar to the displacement oscillations, the amplitude of the power fluctuations due to membrane vibration is also small. The maximum amplitude of power fluctuations for the 6 studied wind speeds is about 1% of the mean power. Furthermore, the transient power is oscillating around the steady-state solution. Convergence of the transient solution to the steady state one demonstrates the consistency between the two approaches.

As illustrated in Fig. 7.28, the membrane blade is more efficient in extracting power from the wind and it becomes more efficient compared with the rigid blade as the wind speed, and consequently membranes deformation, increases.

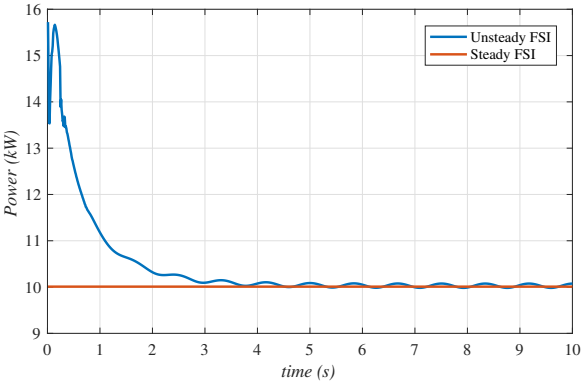

Figure 7.39: Fluctuations in the generated power by the membrane blade rotor, ($U = 8\,m/s$, $\theta_p = 5°$).

This could also be confirmed by the distribution of the axial induction coefficient (Eqn. 2.12). The comparison of the axial induction coefficient between the membrane blade and the rigid blade is made in Fig. 7.40. The red curves correspond to the rigid blade and the blue ones show the convergence course of the axial induction coefficient over time. The axial induction factor is $a = \frac{1}{3}$ for the Betz-optimized rotor. As it can be seen in the figure, for $U = 5\,m/s$ the axial induction factor is higher for the rigid blade all over the blades. This explains the higher power production by the rigid blade, compared with the membrane blade at this velocity. With the increase of wind speed, the axial induction factor of the membrane blade surpasses that of the rigid blade at the outer segments of the blade, but not for segment 1. Overall, for the membrane blade the axial induction factor is higher than the rigid blade and the blade operates nearer to the Betz-optimized blade. This clarifies the higher predicted power for the membrane blade, compared with the rigid blade.

7.3.2.2 Wind Shear

In this section aeroelastic behavior of the membrane blade including wind shear is presented. The logarithmic velocity profile (Eqn. 2.105) is used rather than the uniform profile. Consequently, the blade experiences a transient harmonic loading with a period corresponding to blade's rotational speed (72 RPM). This increases the vibrations in the upper and lower membranes compared with the case of uniform wind profile.

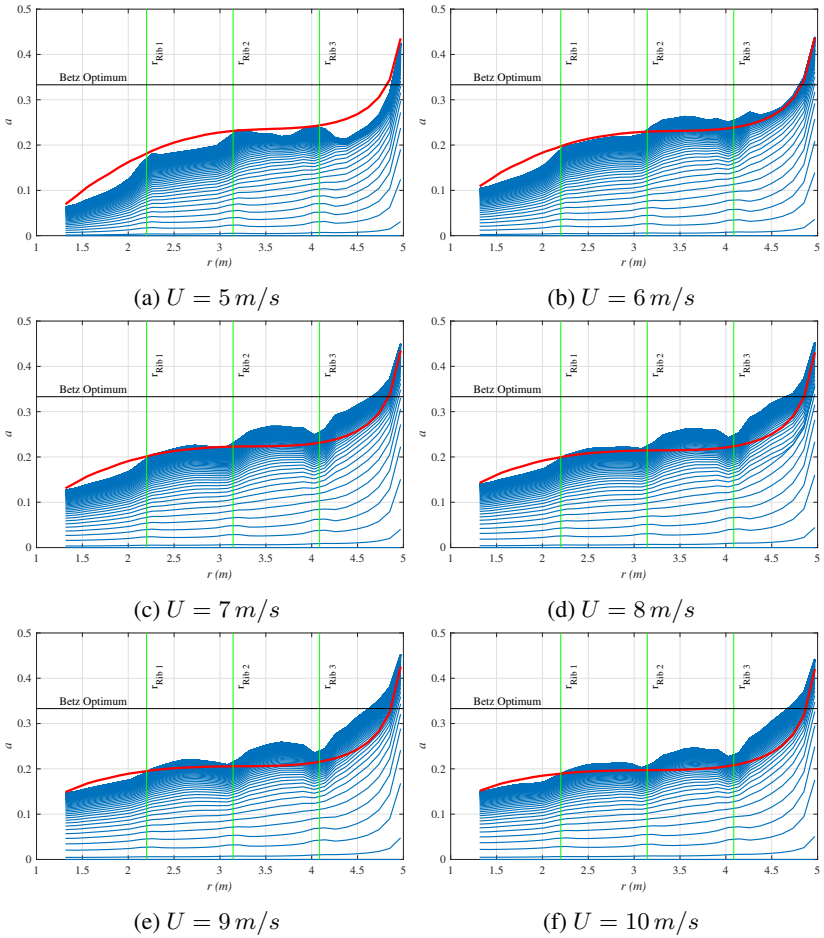

(a) $U = 5\,m/s$ (b) $U = 6\,m/s$

(c) $U = 7\,m/s$ (d) $U = 8\,m/s$

(e) $U = 9\,m/s$ (f) $U = 10\,m/s$

Figure 7.40: Comparison of the distribution of the axial induction coefficient over the blade between the membrane blade (blue) and the baseline rigid blade (red) for different wind speeds.

Fig. 7.41 compares displacement of the membrane at the selected monitor point in the middle of the suction side of segment 3. The amplitude of the oscillations is obviously higher with wind shear. This should also lead to higher fluctuations in the extracted power.

Fig. 7.42 presents the comparison of the generated power between the mem-

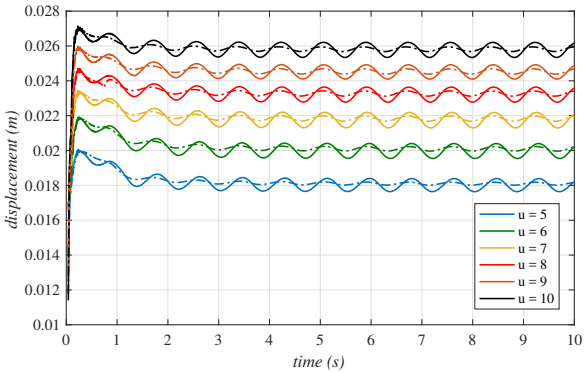

Figure 7.41: Membrane displacement at the selected monitor point taking wind shear into account (full line) and without wind shear (dot-dash line), $\theta_p = 5°$.

brane blade and the rigid blade. Similar to the uniform flow situation (Fig. 7.28 and Fig. 7.40), also for the case of including wind shear the rigid blade produces more power than the membrane blade for the hub-height wind speed of $U = 5\,m/s$. For $U = 6\,m/s$ the generated power is quite the same, but for higher wind speeds, and with the increase of membrane deflection, the extracted power by the membrane blade surpasses that of the rigid blade. At the same time power fluctuation due to wind shear is higher for the membrane blade which is because of membrane's vibration (Fig. 7.41).

Finally, the local change in axial induction factor over time is compared for the two blades. Fig. 7.43 shows the local axial induction factor at the middle of segment 3 for the membrane blade and the rigid blade. The same trend as in the extracted power can be seen here as well, namely starting from the wind speed of $U = 6\,m/s$ the axial induction factor of the membrane blade is higher than the rigid blade and consequently the membrane blade is more efficient.

7.4 High-fidelity FSI analysis of the rotating membrane blade

Multi-fidelity analysis of the non-rotating membrane blade has been presented in section 7.2 and in section 7.3 analysis of the membrane blade using the panel-BEM coupling approach has been covered for both steady state situation in non-rotating configuration and transient case including blade's rotation.

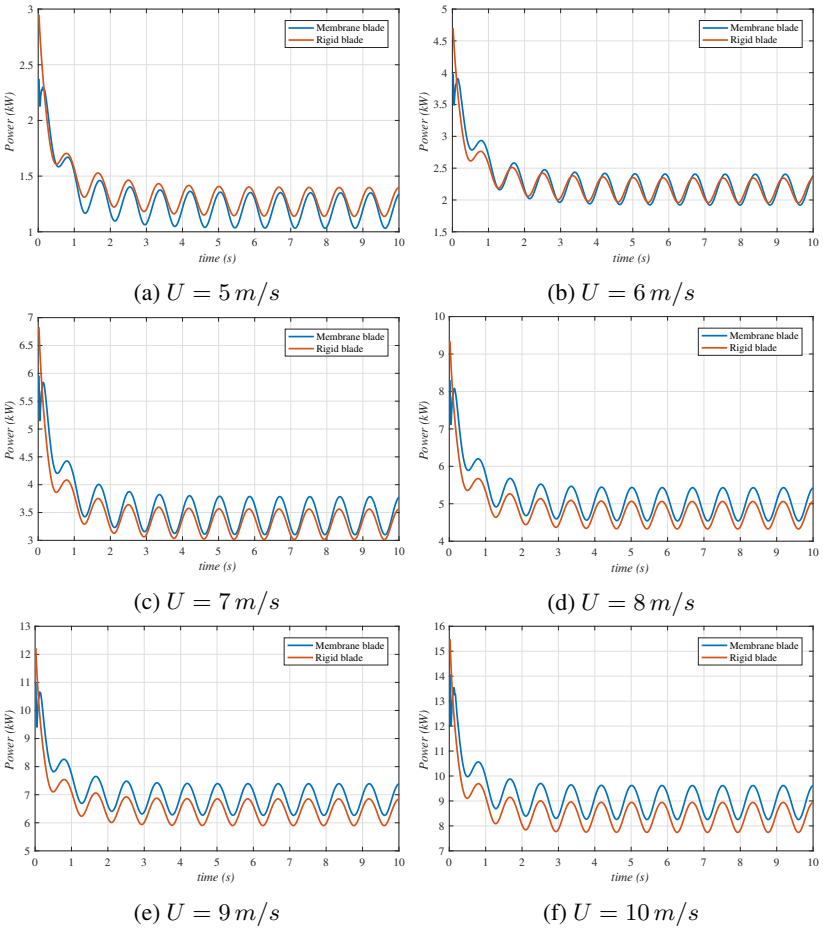

(a) $U = 5\,m/s$ (b) $U = 6\,m/s$

(c) $U = 7\,m/s$ (d) $U = 8\,m/s$

(e) $U = 9\,m/s$ (f) $U = 10\,m/s$

Figure 7.42: Comparison of the extracted power from the wind over time between the membrane blade and its corresponding rigid blade for different wind speeds.

The proposed workflow for the transient FSI analysis of the membrane blade in section 7.3.2 is a low-fidelity approach to facilitate accelerated analysis of the membrane blade. The method is mainly based on panel method and, in general, over-predicts the performance for both the membrane blade and its corresponding baseline rigid blade. To overcome this shortcoming, the final

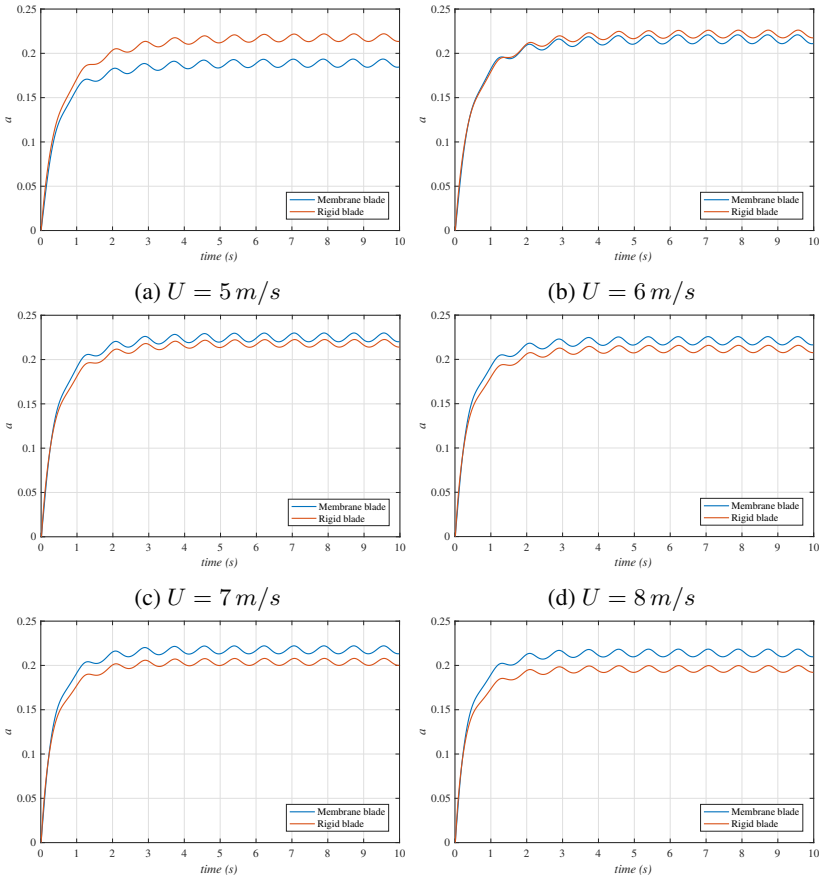

(a) $U = 5\,m/s$ (b) $U = 6\,m/s$

(c) $U = 7\,m/s$ (d) $U = 8\,m/s$

(e) $U = 9\,m/s$ (f) $U = 10\,m/s$

Figure 7.43: Comparison of the axial induction factor between the membrane blade and its corresponding rigid blade for different wind speeds.

design of the membrane blade needs to be analyzed using high-fidelity models utilizing CFD for flow modeling. This section discusses the performance of the membrane blade in rotating configuration via high-fidelity steady-state FSI analysis. Multiple Reference Frame (MRF) solver in OpenFOAM is used for modeling of the rotating blade. In the coming sections, first the model setup in OpenFOAM is presented and verified for the case of the rigid blade. The verified setup is then used for the FSI analysis of the membrane blade. Finally,

comparison of the performance of the membrane blade with the baseline rigid blade is discussed. Similar to the previous sections, the NASA-Ames Phase VI wind turbine has been taken as the baseline rigid blade.

7.4.1 Simulation setup

Schematic representation of the computational domain used in the analysis is presented in Fig. 7.44. The NASA-Ames Phase VI wind turbine is a two-bladed turbine. Only one blade is modeled using periodic boundary condition for the boundaries cyclicAMI1 and cylcicAMI2. The same blocking structure as the one in Fig. 7.6 is used for generating the finite volume mesh using the blockMeshDict in OpenFOAM. The utilized boundary conditions are summarized in Table 7.11.

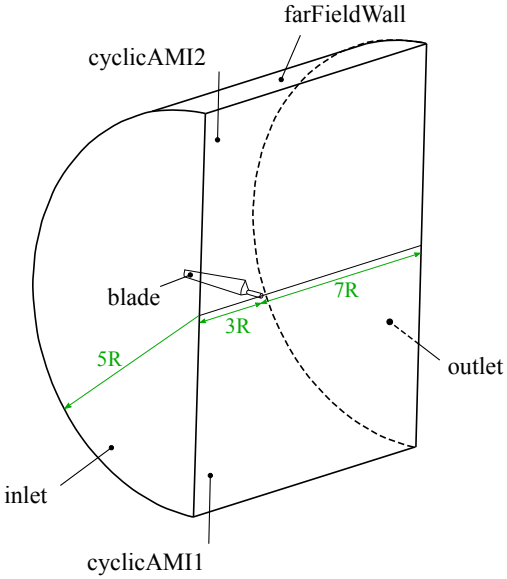

Figure 7.44: Computational domain and its dimensions. R is rotor's radius.

7.4.2 CFD analysis of the baseline rigid blade

Steady-state analysis of the rotating blade problem is performed using the simpleFoam solver. Rotation of the blade is taken into account via Multi Reference

Table 7.11: Boundary conditions for CFD simulations.

boundary	U	p	nut	$nuTilda$
inlet	fixedValue uniform (u, v, w)	zeroGradient	fixedValue uniform $1.03e-5$	fixedValue uniform $6e-5$
outlet	zeroGradient	fixedValue uniform 0	zeroGradient	zeroGradient
farFieldWall	slip	slip	slip	slip
blade	fixedValue uniform $(0, 0, 0)$	zeroGradient	nutkWallFunction	fixedValue uniform 0
cyclicAMI1&2	cyclicAMI	cyclicAMI	cyclicAMI	cyclicAMI

Frame (MRF) in OpenFOAM. The SpalartAllmaras model is used for turbulence modeling. The mesh consists of about 9.3 million elements. The blade is discretized into 75 elements in the spanwise direction and into 240 elements in the chordwise direction. The structure of the vortices in the wake of the rotor and the induced rotation in the flow is graphically presented in Fig. 7.45 ($U = 7\,m/s, \theta_p = 5°$).

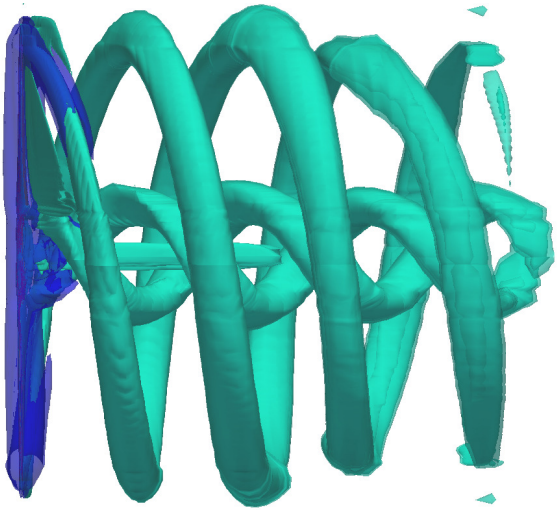

Figure 7.45: Vortex structures in the wake of the rotor.

To verify the simulation setup the obtained results have been compared with the available experimental and numerical results. Comparison of the distribution of the pressure coefficient over the blade with experimental and numerical data reported in [39] is shown in Fig. 7.46 at $r/R = 0.3$ section and in Fig. 7.47

at $r/R = 0.8$ section of the blade. There is a good agreement between the OpenFOAM results and the reference results.

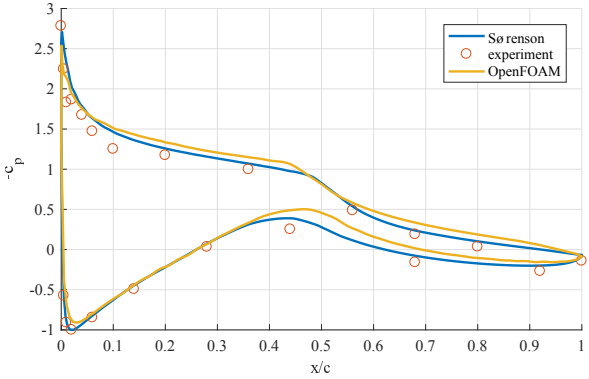

Figure 7.46: comparison of the pressure coefficient at $r/R = 0.3$ ($U = 7\,m/s, \theta_p = 3°$)

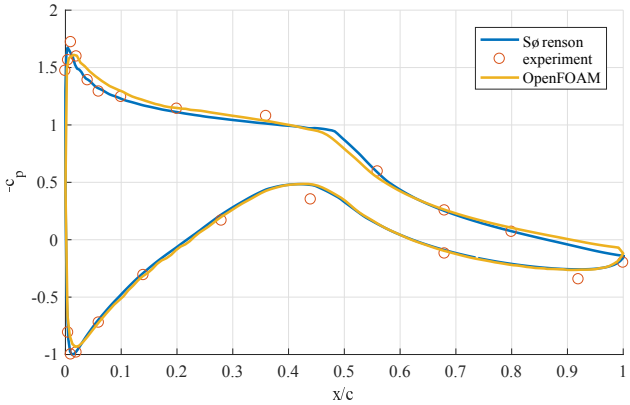

Figure 7.47: comparison of the pressure coefficient at $r/R = 0.8$ ($U = 7\,m/s, \theta_p = 3°$)

Next, comparison of the predicted power generation is made in Fig. 7.48 for the pitch angle of $\theta_p = 5°$ and for wind speeds of 5, 7 and $9\,m/s$. Again, the calculated results match very well the reference results, with their relative difference being less than 5%. The verified fluid setup is then used in the next section for FSI analysis of the membrane blade.

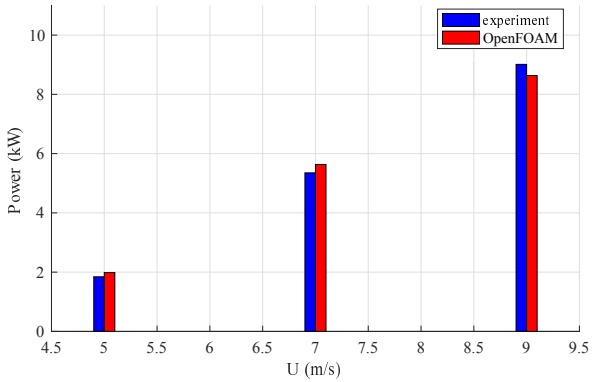

Figure 7.48: comparison of the calculated power ($\theta_p = 5°$).

7.4.3 FSI analysis of the rotating membrane blade

This section discusses the steady-state FSI analysis of the membrane blade in rotating, uniform flow condition. The analysis is done for the pitch angle of $\theta_p = 5°$ and for three different wind speeds: 5, 7 and 9 m/s. The pre-stresses are the same as the S3 pre-stresses reported in Table 7.8.

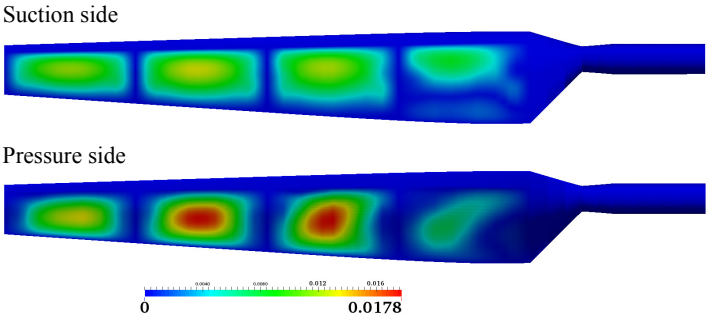

Figure 7.49: Membrane deformation ($U = 7\,m/s$, $\theta_p = 5°$).

Form comparison

The geometry of the blade at the beginning of the FSI analysis is the outcome of form finding analysis, which represents the equilibrium shape of the blade.

Under the applied aerodynamic wind load, the membranes deform. The steady state deformation of the blade for $U = 7\,m/s$ is shown in Fig. 7.49.

Comparison of blade's cross section (at the middle of each segment) between the membrane blade and the baseline rigid blade is made in Fig. 7.50. Membrane's displacement increases toward the tip of the blade (segment 4), which leads to higher camber in blade's profile toward the tip. Next, the change in camber is compared.

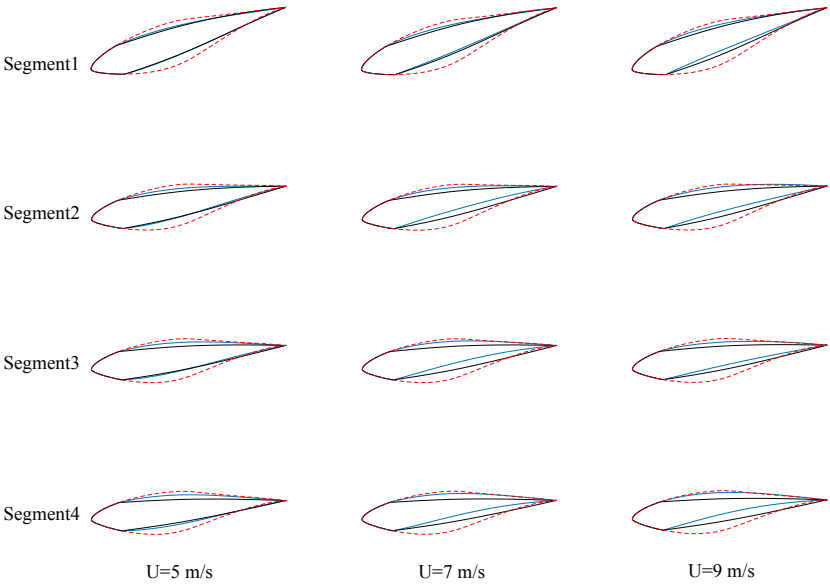

Figure 7.50: comparison of blade's cross section. Red: rigid blade, Black: undeformed membrane blade, Blue: deformed membrane blade.

Camber line comparison

Comparison of the camber line between the membrane blade and the baseline rigid blade is presented in Fig. 7.51. The camber line in the middle of segment 1 and 4 is depicted in the figure. For $U = 5\,m/s$ the rigid blade has a higher camber . Furthermore, the point of maximum camber is shifted toward the leading edge for the membrane blade. With the increase of membrane's deflection with the increase of wind speed, for $U = 7\,m/s$ and $U = 9\,m/s$ the camber for the membrane blade is higher than the baseline rigid blade.

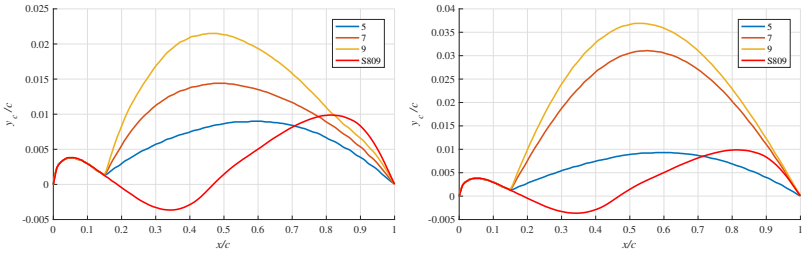

(a) Segment 1 (b) Segment 4

Figure 7.51: Camber line comparison in the middle of blade segments.

Power comparison

Fig. 7.52 compares the generated power between the membrane blade and the baseline rigid blade. The same trend from section 7.3.1 is observed in the high-fidelity analysis of the membrane blade. The initial shape of the membrane blade which is the result of form finding analysis is not an aerodynamically optimal shape. In the initial shape, the cross section of the membrane blade at different spanwise locations looks like shrunk airfoils. It is the deflection of the membranes which changes the cross section profile of the blade and converts the initial shape to a more airfoil-like shape. At the wind speed of $U = 5\,m/s$ the deflection of the membranes is apparently smaller than 7 and $9\,m/s$ and the power generated by the membrane blade is slightly lower than that of the baseline rigid blade. But with the increase of wind speed and respectively the increase of membrane's deflection and profile's camber, the membrane blade surpasses the baseline blade in generating power. For $U = 5\,m/s$ the membrane blade generates about 1.5% less power, but for $U = 7\,m/s$ and $U = 9\,m/s$ the membrane blade produces respectively 9.2% and 7% more which should be mainly due to increase of profile's camber compared with the rigid blade.

Pressure distribution comparison

Finally, the pressure distribution over the two blades is compared. The comparison is made in Fig. 7.53 for the wind velocity of $U = 7\,m/s$. The enclosed area within the pressure coefficient curve shows the pressure difference between the suction and the pressure side of the blade which is the main contributor to the lift force. The membrane blade produces more power at $U = 7\,m/s$, so it should have generated more lift. This is approved by the comparison of

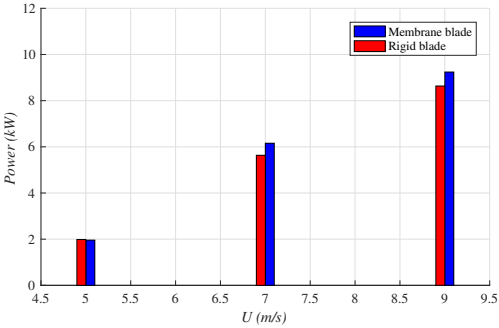

Figure 7.52: Comparison of the generated power.

the pressure distribution over the blade. Compared with the rigid blade the enclosed area within the pressure coefficient curve of the membrane blade is larger. For the first segment, the difference is less significant, but the relative difference increases toward the tip of the blade.

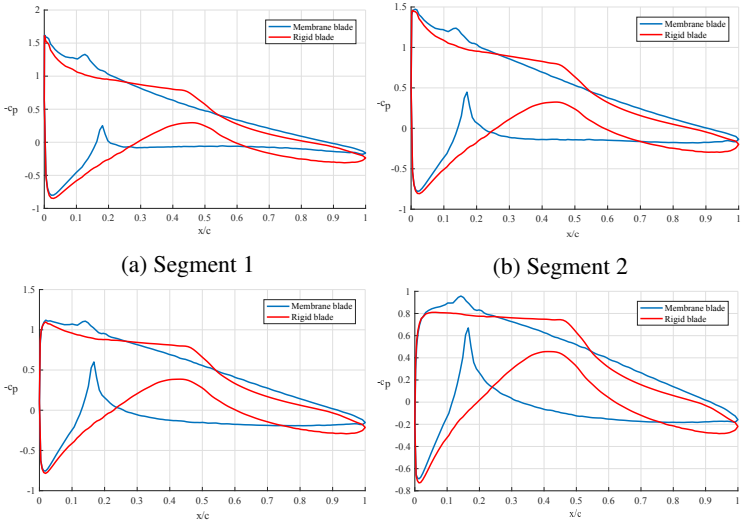

(a) Segment 1

(b) Segment 2

(c) Segment 3

(d) Segment 4

Figure 7.53: Comparison of pressure coefficient distribution at the middle of blade segments ($U = 7\,m/s$).

8 *Summary and Conclusion*

The goal of this dissertation was twofold: to develop an environment for multi-fidelity aeroelastic analysis of wind turbine blades, and to analyze the potential of using the sailwing concept for the design of wind turbine blades. To realize the multi-fidelity analysis workflow, three methods were utilized for predicting the aerodynamic loading on wind turbines. These methods are (ordered by increasing complexity): the blade element method (BEM), vortex panel method and CFD analysis.

Steady state and transient implementations of the BEM method were discussed. The implementations were used for evaluating the performance of the NASA-Ames Phase VI wind turbine and evaluating the loading on its blades. Furthermore, the transient BEM solver was linked with a turbulent inflow generator for predicting the unsteady aerodynamic loading on the blade (taking both, atmospheric turbulence, as well as wind shear into account) and was coupled with the developed structural dynamic solver based on modal decomposition for aeroelastic simulation of the blade.

Implementation of 2D, 3D steady state and 3D transient panel method was discussed and the implementations were verified against reference results obtained from XFLR5. Examples including simple wing geometries like a rectangular wing were solved for cases like sudden acceleration and pitching oscillation of the wing. The implemented 3D transient code was furthermore tested for more complex geometries, i.e. wind turbine rotors. A good agreement between the obtained result and the reference experimental and numerical (CFD) results were observed.

The implemented panel method was then employed as the fluid solver to de-

velop a low-fidelity FSI workflow via coupling between the panel code and CARAT++. The developed workflow was tested for steady and transient analysis and was verified against high-fidelity FSI analysis using CFD for the fluid side. The low-fidelity approach was about 25 times faster in the steady state analysis and about 13 times faster in transient FSI analysis. The range of applicability of the low-fidelity FSI environment was studied and a very good agreement between the low-fidelity and high-fidelity FSI simulations was observed at this range.

Application of the sailwing concept to a sample membrane blade for wind turbines was analyzed in three levels: multi-fidelity analysis in non-rotating configuration, FSI analysis of the blade via panel-BEM coupling in transient and steady state operation and finally, high-fidelity FSI analysis of the membrane blade in rotating configuration. For the examined example in the non-rotating configuration the slope of the lift curve and also profile's camber were higher for the membrane blade than the rigid baseline blade.

A methodology for FSI analysis of the membrane blade via panel-BEM coupling was introduced. Two levels of coupling were utilized for evaluating the performance of the membrane blade via BEM. The first level is the coupling between the fluid solver and the structural solver in a typical FSI coupling iteration loop for calculating membrane's deflection. The second level is the coupling between the panel code and the BEM code, where the BEM solver initially receives the lift and drag coefficients from the 2D panel code and then sends the induced velocities to the 3D panel code for calculating the loading on the blade. Using the proposed FSI analysis procedure for the membrane blade via panel-BEM coupling, higher power production was predicted for the membrane blade and the membrane blade was in general closer to the Betz-optimum blade than the rigid baseline blade for the studied membrane blade which has the same planform as the NASA-Ames Phase VI rigid blade.

Finally, high-fidelity FSI analysis of the membrane blade was performed using CFD for the fluid side. The rotation of the blade was modeled using the Multi Reference Frame (MRF) approach in OpenFOAM. The same trend was observed in the high-fidelity analysis as well. For lower wind speeds ($5\,m/s$ in the studied example) the rigid blade generates more power than the membrane blade. But, for higher wind speeds and with the increase of membrane's deflection and the consequent increase in profile's camber, the membrane blade generated more power.

To the author's opinion, the membrane blade concept could have a great potential in facilitating the light-weight construction of wind turbines and reducing

the cost of energy production from wind. However, the main focus of this contribution was on evaluating the aerodynamic performance of such a blade concept via FSI analysis. The following items list worthwhile topics for further research in the membrane blade and possible challenges in the realization of the concept.

- Analysis of the blade at higher wind speeds and unsteady operating conditions.
- Coupling of the implemented panel method solver with boundary layer models for modeling the viscous effects.
- Fatigue lifetime analysis of the membranes to gain insights about whether the pre-stressed membranes could last for the typical 20-25 year lifespan of a wind turbine.
- The problem of leading edge erosion for designs in which the membranes are not attached to the leading edge mast at some distance away form the leading edge, but are wrapped around it (as in the Princeton sailwing windmill).
- Providing the required bending stiffness for the membrane blade. In conventional blades, the stiffness of the blade is provided by internal components like shear webs, which are glued to the pressure and suction side of the blade and foam panels which are used to increase the stiffness in the trailing edge. The membrane blade apparently requires a different design for realizing the stiffness of the blade against the edgewise and flapwise loading. The internal structural components in the space between the pressure and the suction side of the blade could also prevent the deformation of the membranes, in particular on the pressure side of the blade.
- Integration of morphing mechanisms into the blade design to realize a semi-active adaptive blade and exploiting the advantage of operating at the optimal local angle of attack by actively adjusting the twist in the blade segments at the ribs.

Appendix

Hypergeometric function

The hypergeometric function, ${}_2F^1(a, b, c, z)$, is a solution of the hypergeometric differential equation,

$$z(1-z)F'' = abF - [c - (a+b+1)z]\,F' \tag{A.1}$$

where primes denote $\frac{d}{dz}$. For generation of anisotropic turbulence, the eddy life time is calculated using this function. The arguments of the function for this special case are:

$$a = \frac{1}{3},$$
$$b = \frac{17}{6},$$
$$c = \frac{4}{3},$$

and

$$z = -(kL)^2.$$

Analytic solution of Eqn. A.1 is available for special set of arguments, but for the above set there is no analytic solution and function value should be calculated by path integration method. For calculating the function value at z_1, the method starts from a point, z_0, where the value of the function and its derivative are known. z_0 is connected to z_1 via a line parameterized by:

$$z(s) = z_0 + s(z_1 - z_0). \tag{A.2}$$

Eqn. A.1 is written as a set of two first order equations:

$$\frac{dF}{ds} = (z_1 - z_0)F', \tag{A.3}$$

and

$$\frac{dF'}{ds} = (z_1 - z_0)\left(\frac{abF - [c - (a + b + 1)z]F'}{z(z - 1)}\right). \tag{A.4}$$

The line connecting z_0 to z_1 is divided to a number of segments. Starting from z_0 and using equations A.3 and A.4, at each step the value of function and its derivative are calculated for the neighboring point until z_1 is reached. In the current the algorithm from [29] is used to calculate the hypergeometric function.

B

The NASA-Ames Phase VI turbine

The NASA-Ames Phase VI turbine [70] is a two-bladed research wind turbine designed and tested during the 80s (Fig. B.1). The primary purpose of the testing campaign has been to provide experimental data regarding three-dimensional aerodynamic behavior of horizontal axis wind turbines. It is a stall controlled machine with the nominal rotational speed of 72 RPM. The blade length is approximately 5.5 meters in the extended version and 5 meters in the baseline blade. Blade's cross section is the S809 profile. Chord and twist

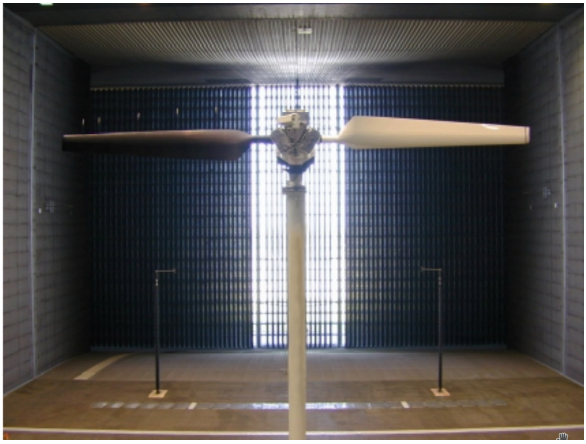

Figure B.1: NASA-Ames Phase VI turbine, from [70]

distribution for the blade and its structural properties are summarized in Tables

Table B.1: Blade chord and twist distribution, from [70].

Radial position (m)	Chord (m)	Twist (deg)
0	0.218	0
0.66	0.218	0
0.883	0.183	0
1.008	0.349	6.7
1.133	0.544	13.4
1.258	0.737	20.05
1.522	0.710	14.04
1.798	0.682	9.67
2.075	0.654	6.75
2.352	0.626	4.84
2.628	0.598	3.48
2.905	0.570	2.40
3.181	0.542	1.51
3.458	0.514	0.76
3.735	0.486	0.09
2.772	0.483	0.00
4.011	0.459	-0.55
4.288	0.431	-1.11
4.565	0.403	-1.55
4.841	0.375	-1.84
5.030	0.356	-2.00
5.118	0.347	-2.08
5.395	0.319	-2.36
5.533	0.305	-2.50

B.1 and B.2. The transition from cylindrical part at the root of the blade into the airfoil sections takes palace from $r = 0.883$ to $r = 1.257$.

Table B.2: Structural properties of the blade, from [70].

Radial position (m)	Mass per unit length (kg/m)	Mass moment of inertia about Y axis (kgm^4)	Mass moment of inertia about Z axis (kgm^4)	Torsional stiffness (Nm^2)	Axial stiffness (Nm)	Edgewise stiffness (Nm^2)	Flapwise stiffness (Nm^2)
0.369	34.784	6.99E-05	6.99E-05	3.16E+05	1.04E+09	4.16E+05	4.16E+05
0.483	223.973	1.87E-02	1.87E-02	1.31E+07	6.69E+09	1.72E+07	1.72E+07
0.508	39.557	6.26E-04	6.26E-04	3.00E+06	1.01E+09	4.06E+06	4.06E+06
0.559	50.797	6.73E-02	6.73E-02	3.68E+06	1.48E+09	6.85E+06	6.85E+06
0.61	44.797	6.73E-02	6.73E-02	3.12E+06	1.33E+09	6.10E+06	6.10E+06
0.66	33.797	6.73E-02	6.73E-02	2.14E+06	1.03E+09	4.77E+06	4.77E+06
0.883	9.973	3.98E-02	3.98E-02	4.02E+05	3.95E+08	1.65E+06	1.65E+06
1.257	16.265	4.88E-01	3.80E-02	3.18E+06	4.07E+08	7.22E+06	1.35E+06
1.343	16.134	4.78E-01	3.68E-02	3.09E+06	4.04E+08	7.20E+06	1.30E+06
1.51	15.623	4.51E-01	3.40E-02	2.89E+06	3.84E+08	6.92E+06	1.17E+06
1.648	15.21	4.29E-01	3.17E-02	2.74E+06	3.67E+08	6.69E+06	1.07E+06
1.952	14.741	3.94E-01	2.77E-02	2.45E+06	3.57E+08	6.49E+06	9.16E+05
2.257	14.379	3.59E-01	2.44E-02	2.19E+06	3.52E+08	6.23E+06	8.05E+05
2.343	12.38	2.77E-01	1.99E-02	1.63E+06	3.21E+08	5.02E+06	7.20E+05
2.562	11.705	2.45E-01	1.72E-02	1.45E+06	2.92E+08	4.38E+06	6.08E+05
2.867	10.853	2.04E-01	1.41E-02	1.22E+06	2.56E+08	3.59E+06	4.79E+05
3.172	10.279	1.70E-01	1.20E-02	1.03E+06	2.36E+08	2.99E+06	4.07E+05
3.185	10.253	1.69E-01	1.19E-02	1.03E+06	2.35E+08	2.97E+06	4.03E+05
3.476	9.585	1.40E-01	9.74E-03	8.56E+05	2.10E+08	2.44E+06	3.20E+05
3.781	8.935	1.14E-01	7.85E-03	7.07E+05	1.85E+08	1.97E+06	2.49E+05
4.023	8.416	9.56E-02	6.50E-03	5.97E+05	1.66E+08	1.63E+06	2.00E+05
4.086	8.291	9.15E-02	6.20E-03	5.73E+05	1.61E+08	1.56E+06	1.89E+05
4.391	7.672	7.21E-02	4.81E-03	4.57E+05	1.38E+08	1.21E+06	1.40E+05
4.696	7.043	5.54E-02	3.64E-03	3.57E+05	1.15E+08	9.14E+05	9.97E+04
4.78	6.882	5.16E-02	3.37E-03	3.34E+05	1.09E+08	8.45E+05	9.05E+04
5	6.44	4.16E-02	2.68E-03	2.73E+05	9.36E+07	6.71E+05	6.80E+04

Bibliography

[1] Bowmann, J., Sanders, B., Cannon, B., Kudva, J, Joshi, S., Weisshaar, T., 2007. Development of Next Generation Morphing Aircraft Structures. 48th AIAA/ASME/ASCE/AHS/ASC Structures, Structural Dynamics, and Materials Conference, Honolulu, Hawaii. doi: 10.2514/6.2007-1730.

[2] Blondeau, J., Richeson, J., and Pines, J.D., 2003. Design, development and testing of a morphing aspect ratio wing using an inflatable telescopic spar. 44th AIAA/ASME/ASCE/AHS/ASC Structures, Structural Dynamics, and Materials Conference. doi: 10.2514/6.2003-1718.

[3] Lian, Y., and Shyy, W., 2005. Numerical Simulation of Membrane Wing Aerodynamics for Micro Air Vehicle Applications. AIAA Journal of Aircraft, Vol. 42, No. 4, pp. 865-873. doi: 10.2514/1.5909.

[4] Abdulrahim, M., Garcia, H., and Lind, R., 2005. Flight Characteristics of Shaping the Membrane Wing of a Micro Air Vehicle. AIAA Journal of Aircraft, Vol. 42, No. 1, pp. 131-137. doi: 10.2514/1.4782.

[5] Fink, M., 1967. Full-scale Investigation of the Aerodynamic Characteristics of a Model Employing a Sailwing Concept. NASA-TN-D-4062.

[6] Maughmer, M.D., 1976. Optimization and Characteristics of a Sailwing Windmill Rotor. Princeton University.

[7] Maughmer, M.D., 1979. A Comparison of the Aerodynamic Characteristics of Eight Sailwing Airfoil Sections. Proceedings of the 3rd International Symposium on the Science and Technology of Low Speed and Motorless Flight, Hampton, VA, USA, 155-176.

[8] Fink, M., 1969. Full-scale Investigation of the Aerodynamic Characteristics of a Sailwing of Aspect Ratio 5.9. NASA-TN-D-5047.

[9] Levin, O., and Shyy, W., 2001. Optimization of a flexible low Reynolds number airfoil. 39th Aerospace Sciences Meeting and Exhibit, Aerospace Sciences Meetings. doi: 10.2514/6.2001-125.

[10] Waszak, R.M., Jenkins, N.L., and Ifju P., 2001. Stability and Control Properties of an Aeroelastic Fixed Wing Micro Aerial Vehicle. AIAA Atmospheric Flight Mechanics Conference and Exhibit, Guidance, Navigation, and Control and Co-located Conferences, Montreal, Canada. doi: 10.2514/6.2001-4005.

[11] Shyy, W., Klevebring, F., Nilsson, M., Sloan, J., Carroll, B., and Fuentes, C., 1999. Rigid and Flexible Low Reynolds Number Airfoils. Journal of Aircraft, Vol. 36, No. 3, pp. 523529. doi: 10.2514/2.2487.

[12] Lian, Y., and Shyy, W., 2007. Laminar-Turbulent Transition of a Low Reynolds Number Rigid or Flexible Airfoil. AIAA Journal, Vol. 45, No. 7, pp. 15011513. doi: 10.2514/1.25812.

[13] Song, A., Tian, X., Israeli, E., Galvao, R., Bishop, K., Swartz, S., and Breuer, K., 2008. Aeromechanics of Membrane Wings with Implications for Animal Flight. AIAA Journal, Vol. 46, No. 8,pp. 2096-2106. doi: 10.2514/1.36694.

[14] Gordnier, R.E., 2009. High fidelity computational simulation of a membrane wing airfoil. Journal of Fluids and Structures, Vol. 25, Issue 5,pp. 897917. doi:10.1016/j.jfluidstructs.2009.03.004.

[15] Ormiston R., 1971. Theoretical and Experimental Aerodynamics of the Sailwing. Journal of Aircraft, Vol. 8, No. 2, pp. 77-84. doi: 10.2514/3.44232.

[16] Mann, J., 1994. The spatial structure of neutral atmospheric surface-layer turbulence. Journal of Fluid Mechanics, 273, pp. 141168. doi: 10.1017/S0022112094001886.

[17] Mann, J., 1994. Models in micrometeorology. Risø National Laboratory, Roskilde, Denmark.

[18] Hansen, M.O.L., 2008. Aerodynamics of Wind Turbines. 2nd Edition, Earthscan, London, UK. ISBN-13: 978-1-84407-438-9.

[19] http://www.q-blade.org. December 2016.

[20] Manwell, J. F., McGowan, J.G., Rogers, A., 2009. Wind Energy Explained: Theory, Design and Application. 2nd Edition, John & Wiley Sons Ltd., West Sussex, UK. ISBN: 978-0-470-01500-1.

[21] M.O.L. Hansen, J.N. Sørensen, S. Voutsinas, N. Sørensen, H.Aa. Madsen, 2006. State of the art in wind turbine aerodynamics and aeroelasticity. Progress in Aerospace Sciences, Volume 42, Issue 4, pp. 285-330, ISSN 0376-0421. doi: 10.1016/j.paerosci.2006.10.002.

[22] Spera, D.A., 1994. Wind Turbine Technology. ASME Press, New York, USA. ISBN-13: 978-0791812051.

[23] Snel H., Schepers J.G., 1995. Joint Investigation of dynamic inflow effects and implementation of an engineering method. ECN-C94-107.

[24] Schepers J.G., Snel H., 1995. Dynamic inflow: yawed conditions and partial span pitch control. ECN-C-95-056.

[25] Øye S., 1991. Dynamic stall, simulated as a time lag of separation. In: K.F. McAnulty, editor. Proceedings of the fourth IEA symposium on the aerodynamics of wind turbines, ETSUN-118.

[26] Batchelor, G.K., 1982, The Theory of Homogeneous Turbulence. Cambridge University Press. ISBN: 9780521041171.

[27] Von Kármán, T., 1948. Progress in the Statistical Theory of Turbulence. Proceedings of the National Academy of Sciences of the United States of America, 34(11), 530539. doi: 10.1073/pnas.34.11.530.

[28] Townsend, A.A., 1980. The Structure of Turbulent Shear Flow. University of Cambridge. ISBN-13: 9780521298193.

[29] Press. W.H., Teukolsky S.A., Vetterling, W.T., Flannery B.P., 2007. Numerical Recipes The Art of Scientific Computing. Cambridge University Press. ISBN: 9780521880688.

[30] Wolfe, W. P., Ochs, S.S., 1997. CFD Calculations of S809 Aerodynamic Characteristics. 35th Aerospace Sciences Meeting and Exhibit, Aerospace Sciences Meetings. doi: 10.2514/6.1997-973.

[31] Richards, P.J., Hoxey, R.P., 1993. Appropriate boundary conditions for computational wind engineering models using the $k - \epsilon$ turbulence model. Journal of Wind Engineering and Industrial Aerodynamics, Vol. 46 & 47, pp. 145-153. doi: 10.1016/0167-6105(93)90124-7.

[32] Rao, S. S., 2010. Mechanical Vibrations. 5th edition, Upper Saddle River, N.J.: Prentice Hall. ISBN-13: 978-0132128193.

[33] Katz, J., Plotkin, A., 2008. Low Speed Aerodynamics. Cambridge, Cambridge Univ. Press. ISBN-13: 9780521665520.

[34] Mason, W. H., Jan. 2017. Subsonic Airfoils. Lecture Notes from Configuration Aerodynamics course, Virginia Tech University.

[35] Sanderson, C. , Curtin, R., 2016. Armadillo: a template-based C++ library for linear algebra. Journal of Open Source Software, Vol. 1, pp. 26. doi: 10.21105/joss.00026.

[36] http://www.xflr5.com/. January 2017.

[37] Ortega, E., Flores, R., Oñate, E., 2010. A 3D low-order panel method for unsteady aerodynamic problems. Publication CIMNE N°-343.

[38] van Garrel, A., 2016. Multilevel Panel Method for Wind Turbine Rotor Flow Simulations. PhD Thesis, University of Twente. doi: 10.3990/1.9789036542241.

[39] Sørensen, N. N., Michelsen, J. A., Schreck, S., 2002. Navier-Stokes predictions of the NREL phase VI rotor in the NASA Ames 80 ft $\times$ 120 ft wind tunnel. Wind Energy, 5(2-3), 151-169. doi:10.1002/we.64.

[40] Fox, R. W., McDonald, A. T., Pritchard, P. J., 2015. Introduction to fluid mechanics. Hoboken, NJ: Wiley. ISBN-13: 9781118912652.

[41] White, F. M., 2015. Fluid mechanics. New York, NY: McGraw-Hill Education. ISBN-13: 9780073398273.

[42] Versteeg, H. K., Malalasekera, W., 2007. An introduction to computational fluid dynamics: the finite volume method. Harlow: Pearson Education. ISBN-13: 9780131274983.

[43] Moukalled, F. H., Mangani, L., Darwish, M., 2015. The finite volume method in computational fluid dynamics: an advanced introduction with OpenFOAM and Matlab. Springer. ISBN-13: 9783319168739.

[44] Kupzok, A., 2009. Modeling the Interaction of Wind and Membrane Structures by Numerical Simulation. PhD Thesis, Technische Uiniversität München.

[45] Patankar, S.V., Spalding, D. B., 1972. A Calculation Procedure for Heat, Mass and Momentum Transfer in Three-dimensional Parabolic Flows. International Journal of Heat and Mass Transfer, Vol. 15, p. 1787. doi: 10.1016/0017-9310(72)90054-3.

[46] Issa, R.I., 1986. Solution of the Implicitly Discretised Fluid Flow Equations by Operator-Splitting. Journal of Computational Physics, Vol. 62, pp. 4065, doi: 10.1016/0021-9991(86)90099-9.

[47] Batchelor, G., 2000. An Introduction to Fluid Dynamics (Cambridge Mathematical Library). Cambridge: Cambridge University Press. ISBN-13: 9780521663960.

[48] Pope, S. B., 2000. Turbulent flows. Cambridge: Cambridge University Press. ISBN-13: 9780521598866.

[49] Spalart, P.R.,Allmaras, S.R., 1994. A One-Equation Turbulence Model for Aerodynamic Flows. 30th Aerospace Sciences Meeting and Exhibit, Aerospace Sciences Meetings. doi: 10.2514/6.1992-439.

[50] Godin, P., Zingg, D.W.,Nelson, T.E., 1997. High-lift aerodynamic computations with one- and two-equation turbulence models. AIAA Journal, Vol. 35, No. 2 pp. 237-243. doi: 10.2514/2.113.

[51] Menter, F.R., 1992. Performance of Popular Turbulence Models for Attached and Separated Adverse Pressure Gradient Flow. AIAA Journal, Vol. 30, pp. 2066-2072. doi: 10.2514/3.11180.

[52] Menter, F., 1993. Zonal Two Equation k-w Turbulence Models For Aerodynamic Flows. 23rd Fluid Dynamics, Plasmadynamics, and Lasers Conference, Fluid Dynamics and Co-located Conferences. doi: 10.2514/6.1993-2906-

[53] Wakefield, D.S., 1999. Engineering analysis of tension structures: theory and practice. Engineering Structures, Vol. 21, No. 8, pp. 680-690. doi: 10.1016/S0141-0296(98)00023-6.

[54] Schek, H.-J., 1974. The force density method for form finding and computations of general networks. Computer Methods in Applied Mechanics and Engineering, Vol. 3, No. 1, pp. 115-134. doi: 10.1016/0045-7825(74)90045-0.

[55] Wüchner, R., Bletzinger, K.-U., 2005. Stress-adapted numerical form finding of pre-stressed surfaces by the updated reference strategy. International Journal for Numerical Methods in Engineering, Vol. 64, No. 2, pp. 143-166. doi: 10.1002/nme.1344.

[56] Felippa, C.A., 2016. Nonlinear Finite Element Methods (ASEN 6107). Lecture notes, University of Colorado at Boulder.

[57] Wüchner R., Kupzok A., Bletzinger K.-U., 2007. A framework for stabilized partitioned analysis of thin membrane-wind interaction. International Journal of Numerical Methods in Fluids, Vol. 54, No. 6-8, pp. 945-963. doi: 10.1002/fld.1474.

[58] Farhat, C., Lesoinne, M., 2000. Two efficient staggered algorithms for the serial and parallel solution of three-dimensional nonlinear transient aeroelastic problems. Computer Methods in Applied Mechanics and Engineering, Vol. 182, No. 3-4, pp. 499-515. doi: 10.1016/S0045-7825(99)00206-6.

[59] Piperno S., 1997. Explicit/implicit fluid/structure staggered procedures with a structural predictor and fluid subcycling for 2D inviscid aeroelastic simulations. International Journal for Numerical Methods in Fluids, Vol. 25, No. 10, pp. 1207-1226. doi: 10.1002/(SICI)1097-0363(19971130)25:10<1207::AID-FLD616>3.0.CO;2-R.

[60] Wang T., Wüchner R., Sicklinger S., Bletzinger K.-U., 2016. Assessment and improvement of mapping algorithms for non-matching meshes and geometries in computational FSI. Journal of Computational Mechanics. doi= 10.1007/s00466-016-1262-6, 2016.

[61] Willis, D., Israeli, E., Persson, P., Drela, M., Peraire, J., Swartz, S., Breuer, K., 2007. A Computational Framework for Fluid Structure Interaction in Biologically Inspired Flapping Flight. 25th AIAA Applied Aerodynamics Conference. doi: 10.2514/6.2007-3803.

[62] Nicholls-Lee, R.F., Turnock, S.R., Boyd, S.W., 2011. A method for analyzing fluid structure interactions on a horizontal axis tidal turbine. 9th European Wave and Tidal Energy Conference (EWTEC 2011), United Kingdom. 04-09 Sep., 8 pp.

[63] Kim, J., Kim, Y., 2014. Numerical analysis on springing and whipping using fully-coupled FSI models. Ocean Engineering, Volume 91, Pages 28-50. doi: 10.1016/j.oceaneng.2014.08.001.

[64] Sessarego, M., Ramos-Garca, N., Shen, W. ,2015, Development of a Fast Fluid-Structure Coupling Technique for Wind Turbine Computations. Journal of Power and Energy Engineering, 03(07), 1-6. doi:10.4236/jpee.2015.37001

[65] Saeedi, M., Bletzinger, K.-U., Wüchner, R., 2017. Investigation of Prestress-Dependent Aerodynamic Performance of a Double Membrane Sailwing. Journal of Aircraft, Vol. 54, No. 3, pp. 980-994. doi: 10.2514/1.C033872.

[66] Saeedi, M., Wüchner, R., and Bletzinger, K.-U, 2015. Multi-fidelity Fluid-Structure Interaction Analysis of a Membrane Wing, 17th International Conference on Applied Aerodynamics and Aeromechanics, London.

[67] Bertagnolio, F., Sørensen, N.N., Johansen, J., 2006. Profile catalogue for airfoil sections based on 3D computations. Denmark, Forskningscenter Risoe. Risoe-R, No. 1581(EN).

[68] Saeedi, M., Bletzinger, K.-U., Wüchner, R., Multi-fidelity fluidstructure interaction analysis of a membrane blade concept in non-rotating, uniform flow condition, Wind Energ. Sci., 1, 255-269, doi:10.5194/wes-1-255-2016, 2016

[69] Saeedi, M., Wüchner, R., Bletzinger, K.-U. (2016). Fluid-Structure interaction analysis and performance evaluation of a membrane blade. Journal of Physics: Conference Series, 753, doi:10.1088/1742-6596/753/10/102009

[70] Hand, M.M., Simms, D., Fingersh, L., Jager, D.W, Cotrell, J.R., Schreck, M., Larwood, S.M., Unsteady Aerodynamics Experiment Phase VI: Wind Tunnel Test Configurations and Available Data Campaigns, Tech. Rep. NREL/TP-500e29955, NREL, 2001